Universität Hamburg
DER FORSCHUNG | DER LEHRE | DER BILDUNG

FAKULTÄT
FÜR MATHEMATIK, INFORMATIK
UND NATURWISSENSCHAFTEN

Development of inhibitors against the ADPR-binding macrodomain of the non-structural-protein 3 of SARS-CoV-2

Dissertation for the Acquisition of a Doctoral Degree (Dr. rer. nat.)
at the Department of Chemistry
Faculty of Mathematics, Informatics and Natural Sciences
University of Hamburg

submitted by

Maximilian Sandmann

June 2024

This work was done from December 2020 to June 2024 at the Department of Biochemistry and Molecular Cell Biology (IBMZ) of the University Hospital Hamburg-Eppendorf (UKE) under the supervision of Dr. Ralf Fliegert.

1st reviewer: Professor Ralph Holl
2nd reviewer: Dr. Ralf Fliegert

Date of Disputation: 06th of December 2024

“Only if we understand, will we care.
Only if we care, will we help.
Only if we help, shall all be saved.”

Jane Goodall

Table of Contents

List of Publications

Patent Application

Maximilian Sandmann, Sahra Tajdar, Benedikt Ganter, Marina Ocenas, Chris Meier, Ralf Fliegert: GS-441524 DIPHOSPH(ON)ATE DERIVATIVES AS MACRODOMAIN INHIBITORS. **PAT1873 EP (UKE417 - EP-Minimal)**: Application Number: EP24157879.8, submitted February 15th 2024.

Congress Contributions (posters)

Maximilian Sandmann, Sahra Tajdar, Benedikt Ganter, Andreas Bauche, Frederike Kulow, Chris Meier, Ralf Fliegert: Development of activity-based enzyme assays for the de-ADP-Ribosylating macrodomain of SARS-CoV-2. Published on ***FASEB NAD Metabolism and Signaling Conference***, June 26th to June 30th 2022, Steamboat Springs, Colorado, United States

Maximilian Sandmann*, Sahra Tajdar, Benedikt Ganter, Marina Ocenas, Andreas Bauche, Chris Meier, Ralf Fliegert: Test of inhibitors for the de-ADP-ribosylating macrodomain (Mac1) of SARS-CoV-2 using activity-based enzyme assays and binding studies. Published on ***HIPS Symposium***, May 4th 2023, Saarbrücken, Germany

*awarded with poster price by ***Advanced Therapeutics*** (Wiley)

Maximilian Sandmann#, Sahra Tajdar, Benedikt Ganter, Marina Ocenas, Andreas Bauche, Chris Meier, Susanne Pfefferle, Ralf Fliegert: Development of inhibitors against the de-ADP-ribosylating activity of the macrodomain Mac1 of SARS-CoV-2. Published on ***FEBS Advanced Lecture Course*** *on Cellular Stress and ADP-ribosylation.* November 6th to November 11th 2023, Naples, Italy.

#awarded with best poster price

Maximilian Sandmann, Sahra Tajdar, Benedikt Ganter, Marina Ocenas, Andreas Bauche, Joanna M. Watt, Ondrej Baszczynski,
Barry V. L. Potter, Chris Meier, Andreas H. Guse, Ralf Fliegert: Comparing the effects of ADPR derivatives on the non-selective Ca2+ permeable cation channel TRPM2 and the ADPR-binding macrodomain of SARS-CoV-2. Published on the ***10th European Calcium Society symposium****: The Ca2+-signaling toolkit in cell function, health and disease*. Biology open, 13(4), bio060357. https://doi.org/10.1242/bio.060357

List of Figures

List of Figures (continued)

List of Figures (continued)

List of Tables

List of Abbreviations

µg	microgram
µl	microliter
µM	micromolar
µmol	micromole
µcal	microcalorie
AB	acyloxybenzyl
abs.	absorbance
ADMET	absorption distribution metabolism excretion toxicity
ADP	adenosine-5′-diphosphate
ADPR	adenosine-5′-diphosphate ribose
ADPRP	2′-phospho-adenosine-5′-diphosphate ribose
Af1512	*Archaeoglobus fulgidus* ADP-ribose glycohydrolase 1521
ALC1	chromodomain-helicase-DNA-binding protein 1-like
AMP	adenosine-5′-monophosphate
ARH	ADP-ribosylhydrolase
AVR	assay variability ratio
CaLu-3	non-small cell lung carcinoma-3
cAMP	cyclic adenosine-5′-monophosphate
CC_{50}	half maximal cytotoxic concentration
CDP	cytidine-5´-diphosphate
CHIKV	*chikungunya virus*
cm	centimeter
CoV	coronavirus
COVID-19	coronavirus disease 2019
DMEM	dulbecco´s modified eagle medium
DNA	desoxy-ribonucleic acid
DTT	dithiothreitol
E.coli	*Escherichia coli*
e.g.	*exempli gratia* (for example)
EDTA	ethylenediaminetetraacetic acid
em	emission

List of Abbreviations (continued)

ER	endoplasmatic reticulum
ex	excitation
FF	fast flow
FPLC	Fast protein liquid chromatography
GS	gilead sciences
GST	glutathione-S-transferase
h	hour
HEPES	4-(2-hydroxyethyl)-1-piperazineethanesulfonic acid
His_6	histidine (hexamer)
HPD	hydroxymethyl-pyrrolidinediol
HPLC	high performance liquid chromatography
HTS	high-throughput screen
IC_{50}	half-maximal inhibitory concentration
IDPR	inositol 5´-diphosphate ribose
IFN	interferon
IFNAR	interferon α/ β-receptor
IMAC	immobilized metal-ion affinity chromatography
IRF1	interferon regulatory factor 1
IRF3	interferon regulatory factor 3
ISG	interferon-stimulated gene
ITC	isothermal titration calorimetry
i.e.	*id est* (it means)
kcal	kilocalorie
K_D	dissociation constant
kDa	kilodalton
K_M	michaelis constant
LU	light units
M	molar
Mac1	macroD-like macrodomain 1 of SARS-CoV-2
MacroD1	human mono-ADP-ribosylhydrolase 1
MacroD2	human mono-ADP-ribosylhydrolase 2

List of Abbreviations (continued)

MacroH2A1.1	human macroH2A.1 histone
MAR	mono-ADP-ribosylation
mAU	milliarbitrary units
MDA5	melanoma differentiation-associated protein 5
MERS-CoV	*middle eastern respiratory syndrome coronavirus*
MHR1/2	homology region 1/2 (of transient receptor potential melastatin type)
MHV	*murine hepatitis virus*
min	minute
ml	milliliter
mM	millimolar
MOPS	3-(N-morpholino)propanesulfonic acid
MP	molport
Mpro	main protease of coron
mS	millisiemens
MTS	5-(3-carboxymethoxyphenyl)-2-(4,5-dimenthylthiazoly)-3-(4-sulfophenyl)tetrazolium
n.d.	not determined
NAD	nicotinamide-adenine dinucleotide
NFκB	nuclear factor κ-light-chain-enhancer of activated B cells
nm	nanometer
nM	nanomolar
NMN	nicotinamide mono-nucleotide
nsp3	non-structural protein 3
NUDT5	nudix hydrolase 5
NUDT9	nudix hydrolase 9
NUDT9H	nudix hydrolase 9 homology
NUDT16	nudix hydrolase 16
ORF1	open reading frame 1
PAGE	poly-acrylamide gel electrophoresis
PAR	poly-adenosine-5′-diphosphate ribose

List of Abbreviations (continued)

PARG	poly-adenosine-5′-diphosphate-ribose-glycohydrolase
PARP	poly-adenosine-5′-diphosphate ribose polymerases
PBM	PAR-binding motif
PBZ	PAR-binding zinc finger
PDB	protein data bank
pH	negative decadic logarithm of the hydrogen-ion activity
pK_a	negative decadic logarithm of acid dissociation constant
pmol	picomole
RdRP	RNA-dependen RNA-polymerase
RIG-I	retinoic acid-inducible gene I
RNA	ribonucleic acid
Rt	retention time
s	second
SAL-AMS	5′-((2-hydroxybenzoyl)-sulfamoyl)-adenosine
SAR	structure-activity relationship
SARS	severe acute respiratory syndrom
SD	standard deviation
SDS	sodium dodecylsulfate
SEC	size exclusion chromatography
SI	selectivity index
S_N2	nucleophile substitution mechanism 2
STAT1	signal transducer and activator of transcription 1
STAT2	signal transducer and activator of transcription 2
SW	signal window
TARG	terminal ADP-ribose protein glycohydrolase 1
TFMU	trifluormethylumbelliferone
v_0	initial reaction rate
VEEV	*venezuelan equine encephalitis virus*
v_{max}	maximal reaction rate

List of Abbreviations (continued)

WHO	world health organization
WT	wildtype
WWE	tryptophane-tryptophane-glutamate
Z′	assay robustness
ΔH	enthalpy
ΔS	entropy
ΔΔG	gibbs free enthalpy

1 Abstract

The recurring appearance of coronavirus (CoV) epidemics is highly concerning. Since the recent outbreak of SARS-CoV-2 in 2019, the pandemic potential of these emerging viruses is obvious and has raised global awareness. Despite enormous vaccination efforts, new SARS-CoV-2 mutants continue to evolve, requiring more sustainable antiviral strategies.

In order to keep up in this arms race, new pharmacological targets came into focus. One promising candidate is the non-structural protein 3 (nsp3) of SARS-CoV-2, which contains a macroD-like macrodomain (Mac1) that removes ADP-ribose (ADPR) from proteins. Indeed, the enzymatic activity of Mac1 has been described as an important virulence factor *in vivo*, presumably by reversing cellular ADP-ribosylation, which is part of the host antiviral response. However, due to the limited repertoire of promising Mac1 inhibitors, the development of new drug candidates is still required.

To this aim, an HPLC-based ADP-ribosylhydrolase assay for recombinantly expressed Mac1 was established using α-NAD as a surrogate substrate, which was further modified into a robust fluorimeter-based microplate endpoint assay by post-reaction derivatization of α-NAD. Both the HPLC- and microplate assays showed good comparability and enabled the probing of the Mac1 active site with a unique collection of ADPR and ADP derivatives. The combination with orthogonal isothermal titration calorimetry (ITC) allowed to explore the structure-activity relationship (SAR), which not only provided insights into the molecular interplay between Mac1 and ADPR, but also guided the rational design of inhibitors.

The key findings from this SAR were that i) substitution of the terminal ribose of ADPR for a methyl group resulted in higher affinity for Mac1 than the parental nucleotide, ii) none of the tested pyrophosphate isosteres showed substantial effect on the activity of the viral macrodomain and that iii) unlike adenosine, the nucleoside analogue GS-441524, a known Mac1 ligand, was also a remarkably potent inhibitor of the viral macrodomain, which was even further improved by phosphorylation.

These results initiated the development of β-methyl-GS-441524-5′-diphosphate as selective Mac1 inhibitor with sub-micromolar affinity. Finally, introduction of a bio-reversible C_{11}-acyloxybenzyl (AB) masking group at the β-phosphate resulted in a membrane-permeable prodrug of β-methyl-GS-441524-5′-diphosphate with low cytotoxicity.

Prospectively, this study demonstrates the viability of Mac1 as a drug target, which might not only offer new therapeutic options for combating SARS-CoV-2 infections, but could also harbor the potential for the development of broad-spectrum antivirals in the future, due to the high conservation of viral macrodomains.

2 Zusammenfassung

Das häufige Auftreten von Coronavirus (CoV)-Epidemien ist höchst besorgniserregend. Seit dem jüngsten Ausbruch von SARS-CoV-2 im Jahr 2019 ist das pandemische Potenzial dieser neu erscheinenden Viren offensichtlich und hat das weltweite Bewusstsein geschärft. Trotz enormer Impfbemühungen entwickeln sich weiterhin neue SARS-CoV-2-Mutanten, die nachhaltigere antivirale Strategien erfordern.

Um in diesem Wettrüsten mithalten zu können, ist es wichtig neue pharmakologische Ziele in den Fokus zu nehmen. Ein vielversprechender Kandidat ist das Nicht-Strukturprotein 3 (nsp3) von SARS-CoV-2, das eine macroD-ähnliche Makrodomäne (Mac1) enthält, welche die Bindung zwischen ADP-Ribose (ADPR) und der Aminosäureseitenkette ADP-ribosylierter Proteine durch Hydrolyse spaltet. Die enzymatische Aktivität von Mac1 wurde in der Tat *in vivo* als wichtiger Virulenzfaktor beschrieben, aufgrund der Umkehrung der zellulären ADP-Ribosylierung, die Teil der antiviralen Antwort des Wirts ist. Aufgrund des begrenzten Repertoires an vielversprechenden Mac1-Inhibitoren ist jedoch die Entwicklung neuer Wirkstoffe weiterhin erforderlich.

Zu diesem Zweck wurde ein HPLC-basierter ADP-Ribosylhydrolase-Assay für rekombinant exprimiertes Mac1 unter Verwendung von α-NAD als Surrogatsubstrat etabliert, der durch Nachderivatisierung von α-NAD zu einem robusten Fluorimeter-basierten Mikroplatten-Endpunkt-*Assay* weiterentwickelt wurde. Sowohl die HPLC- als auch die Mikrotiterplatten-*Assays* waren gut untereinander vergleichbar und ermöglichten die Untersuchung des aktiven Zentrums von Mac1 mit einer einzigartigen Sammlung von ADPR- und ADP-Derivaten. Die Kombination mit orthogonaler isothermaler Titrationskalorimetrie (ITC) ermöglichte die Entwicklung einer ersten Struktur-Aktivitäts-Beziehung (SAR), die nicht nur Einblicke in das molekulare Zusammenspiel zwischen Mac1 und ADPR lieferte, sondern auch den rationalen Entwurf von Inhibitoren ermöglichte.

Die wichtigsten Ergebnisse dieser SAR waren, dass i) die Substitution der terminalen Ribose von ADPR durch eine methyl-Gruppe zu einer höheren Affinität für Mac1 führte, ii) keines der getesteten Pyrophosphat-Isostere eine

wesentliche Auswirkung auf die Aktivität der viralen Makrodomäne zeigte und dass iii) das Nukleosid Analogon GS-441524, ein bekannter Mac1 Ligand, im Gegensatz zu Adenosin ein bemerkenswert potenter Mac1-Inhibitor war, was sogar durch Phosphorylierung noch weiter verbessert wurde.

Diese Resultate initiierten die Entwicklung von β-methyl-GS-441524-5′-diphosphat als selektivem Mac1-Inhibitor mit submikromolarer Affinität. Schließlich resultierte die Einführung von bio-reversiblen C_{11}-acyloxybenzyl (AB) Masken in einem Membran-gängigen Propharmakon von β-methyl-GS-441524-5′-diphosphat mit geringer Zytotoxizität.

Diese Studie zeigt perspektivisch, dass Mac1 ein brauchbares Wirkstoffziel ist, welches nicht nur neue therapeutische Optionen für die Bekämpfung von SARS-CoV-2-Infektionen bieten könnte, sondern aufgrund der hohen Konservierung viraler Makrodomänen auch das Potenzial für die Entwicklung von antiviralen Breitbandmedikamenten in der Zukunft haben könnte.

3 Introduction

3.1 Evolution of new highly adapted SARS-CoV-2 mutants demand novel treatment options

In the last two decades highly pathogenic and rapidly spreading coronaviruses have emerged periodically with the latest outbreak by *severe acute respiratory syndrome coronavirus 2* (SARS-CoV-2) in 2019, which has caused to this day over 7 million deaths and still affects public health systems and economy globally (Perlman, 2020; WHO data, https://data.who.int/dashboards). Despite worldwide vaccination efforts, local outbreaks continue and new virus variants arise (Heyer et al., 2022) illustrating the need for better understanding of the adaptive nature of these coronaviruses (CoV), which will hopefully lead to sustainable therapeutic measures in the future.

Additionally, the increasing evidence of SARS-CoV-2 strains that developed drug tolerance against the Mpro inhibitor paxlovid (Padhi & Tripathi, 2021, Cho et al., 2021; Flynn et al., 2022) due to viral mutations (Callaway, 2021, Vogel, 2022; Service, 2022; Heyer et al., 2022) demonstrated the need for new therapeutic strategies for *coronavirus disease 2019* (COVID-19) patients to keep up with the arms race.

3.2 Antiviral interferon response involves ADP-ribosylation

Usually, early stages of infections with respiratory RNA viruses, like *influenca A virus* are fought by an interferon (IFN) response as part of the innate immune system of the host (Jensen & Thomsen, 2012).

But strikingly, cumulative evidence from COVID-19 patients indicate an inappropriate IFN response upon SARS-CoV-2 infection, which suggested the usage of type-I and III IFNs as therapy in clinical trials (Blanco-Melo et al., 2020, Busnadiego et al., 2020; Hadjadj et al., 2020; Lei et al., 2020; Lokugamage et al., 2020; Zhang et al., 2020; Sposito et al., 2021). However, there are mixed reports regarding effectiveness of a COVID-19 treatment with IFNs due to the challenging administration and timing of the intervention

(Jhuti et al., 2022). Thus, other therapeutic strategies, potentially along the IFN signaling pathway, apart from the IFN intervention therapy, appear worthwhile to be investigated.

Recently, ADP-ribosylation came into focus, which is involved in many steps of the antiviral IFN response and is defined by the transfer of ADP-ribose (ADPR) moieties on a multitude of target molecules, such as proteins or nucleic acids by poly-ADPR polymerases (PARP) (Fehr et al,. 2020; Rack et al., 2020a).

Of note, ADP-ribosylation plays a role in many other physiological and patho-physiological processes, including not only viral and microbial infections but also tumorigenesis, DNA repair and chromatin stability, ubiquitinylation and autophagy as well as apoptosis (Fehr et al., 2020).

Despite their name, most of the 17 human PARPs are mono-ADP-ribosyl (MAR)-transferases, whereas only PARP1, PARP2 as well as PARP5A and PARP5B can build up poly-ADPR (PAR) polymers (Fehr et al., 2020).

Using β-NAD as substrate, PARPs covalently bind ADPR to various acceptor sites like acidic amino acids, forming a single linkage at the 1″-position at the terminal ribose of ADPR, which can be extended to long linear or branched chains by PAR-forming PARPs via formation of additional 2′-1″-, as well as 2″-1″-*O*-glycosidic bonds (Figure 1) (Rack et al., 2020a).

In fact, the activities of many of these PARPs have been shown to promote IFN and IFN-stimulated genes (ISGs) as well as pro-inflammatory cytokine production, which all together can impair viral replication, thereby linking ADP-ribosylation with antiviral functions (Fehr et al., 2020). Thus, ADP-ribosylation is involved in type-I IFN signaling already after sensing of the viral RNA by pattern recognition receptors (MDA5 and RIG-I) and can promote NFκB- and IRF3-mediated activation of genes for production of cytokines and IFNs. In addition, ADP-ribosylation has also a role in the pathway downstream of the activation of the IFN α/ β-receptor (IFNAR) by regulation of the subsequent STAT1,2-/ IRF1-dependent induction of > 400 ISGs (Fehr et al., 2020).

Furthermore, PARP8, 9 and PARP11-15 were found to be up-regulated in lung samples of COVID-19 patients (Heer et al., 2020), which emphasizes their importance in response to a SARS-CoV-2 infection.

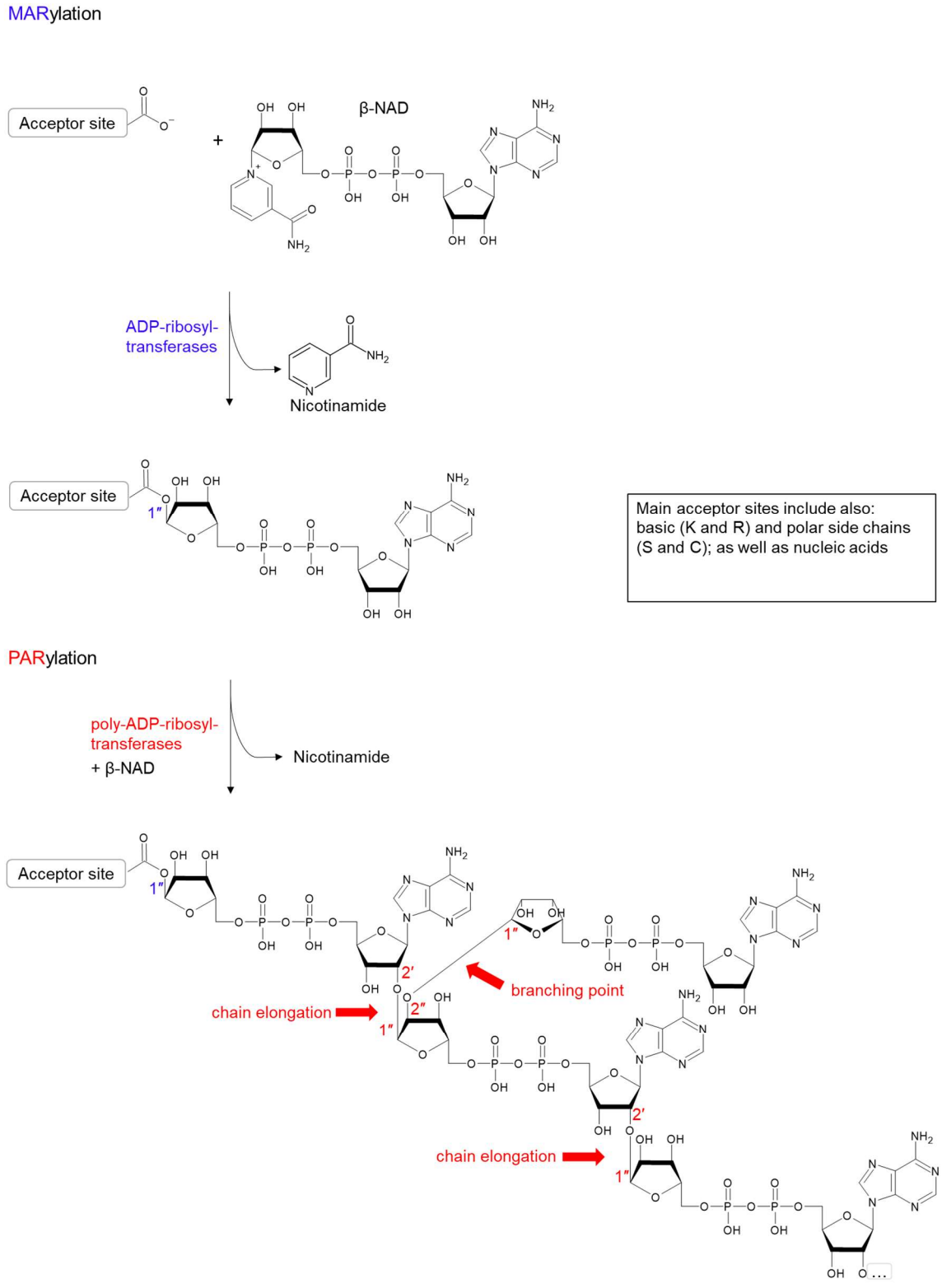

Figure 1: Mechanism of PARP-mediated ADP-ribosylation.
Shown is the β-NAD-dependent mono-ADP-ribos-(MAR)ylation of an exemplary acidic side chain (glutamate or aspartate) by the ADP-ribosyl-transferase activity of human PARPs and the consecutive poly-ADP-ribose (PAR) synthesis by the PARylating PARPs (e.g. PARP1).

3.3 Macrodomains are de-ADP-ribosylating enzymes

PARP-mediated ADP-ribosylation can be recognized by a number of ADPR-binding folds. Among them are the WWE domain (named after their conserved amino acid residues), the PAR-binding zinc fingers (PBZ), the PAR-binding motif (PBM), as well as human nudix domains (like NUDT5, 9, 9H and 16), the MHR1/2 fold and the macrodomain (Yu et al., 2007; Palazzo et al., 2015; Gattkowski et al., 2021; Sander et al., 2022; Suskiewicz et al., 2023).

ADP-ribosylation can by reverted by a number of hydrolytic enzymes, which are divided in two (evolutionary) distinct classes, the ADP-ribosylhydrolases (ARHs) and macrodomains. The enzymatically active members of the human macrodomain family can be further sub-divided in the MacroD-type, i.e. MacroD1 and MacroD2, the ALC1-like, e.g. TARG1 and the PAR-glycohydrolase (PARG)-like class. Whilst the latter is the main PAR-degrading class, the former, the “ALC1”-like and MacroD-type can hydrolyze the 1″-*O*-glycosidic bond (or ester respectively) that links the terminal ribose and the acceptor molecule (proteins or nucleic acids), leading to de-MARylation (Figure 2) (Jankevicius et al., 2013; Palazzo et al., 2015; Barkauskaite et al., 2015; Rack et al., 2020a+b).

Interestingly, substrate preferences, cleavage sites and the overall catalytic mechanism differ among macrodomains (Rack et al., 2020a). For the PARG-like hydrolases, binding of PARylated conjugates induces a pK_a shift of the catalytic glutamate (E756), which leads to increased protonation, allowing it to act as initial base of the reaction (Figure 3A). Whilst the carboxyl hydrogen of the catalytic glutamate is transferred to the PAR moiety (leaving group), an oxocarbenium ion is intermediately formed at the conjugated terminal ribose. Finally, the deprotonated E756 activates a proximal water molecule, which can react with the oxocarbenium intermediate, thereby re-constituting ADPR. The supposed catalysis mechanism of ALC1-like hydrolases involves deprotonation of the catalytic K84 by the proximal E125, which enables the nucleophilic attack of the anomeric C1″ by the amino group leading to release of the former acceptor site (glutamate of aspartate, Figure 3B). Formation of the N-glycosidic linkage results in ribose ring opening and constitution of a Schiff base, which is susceptible to engagement by a water nucleophile. Finally, a ring-opened ADPR is released and K84 is regenerated.

In contrast to PARG- and ALC1-like hydrolases, MacroD-type macrodomains exhibit a substrate-assisted mechanism (Figure 3C). A vitial step of this catalysis model is the coordination and pre-activation of a water molecule by the α-phosphate of the substrate, which acts as base. Subsequent increase of nucleophilicity allows the proximal water molecule to attack the anomeric C1″, which hydrolyzes the glycosidic linkage, thereby releasing free ADPR.

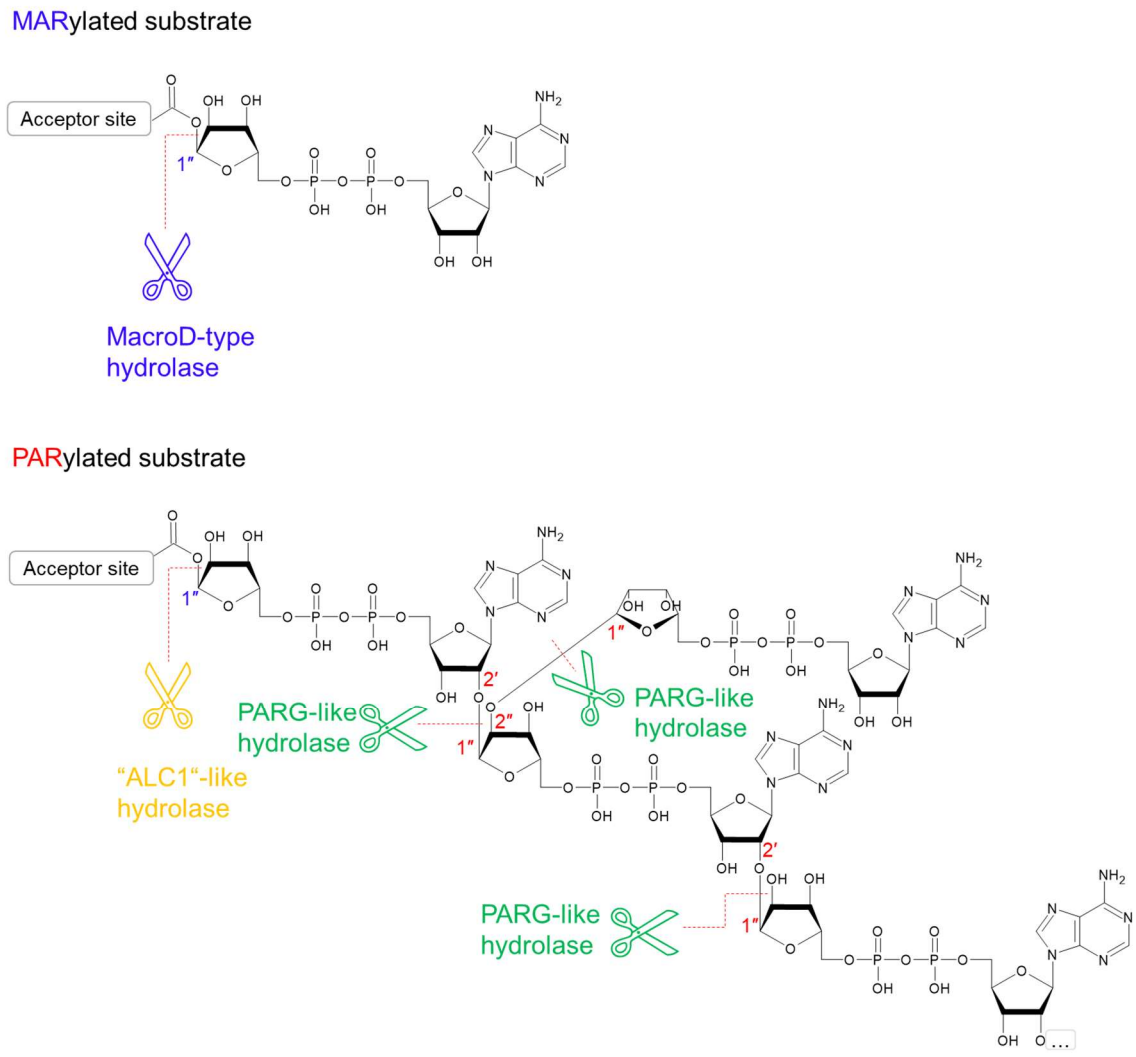

Figure 2: Target sites of macrodomain hydrolases.
Depicted is the substrate preference of the different classes of enzymatically active macrodmains (PARG-like, ALC1-like and MacroD-type) for ADP-ribosylated acceptor sites (e.g. MAR/ PARylated glutamate or aspartate) as well as the chemical bonds that are prone to cleavage by the respective hydrolases.

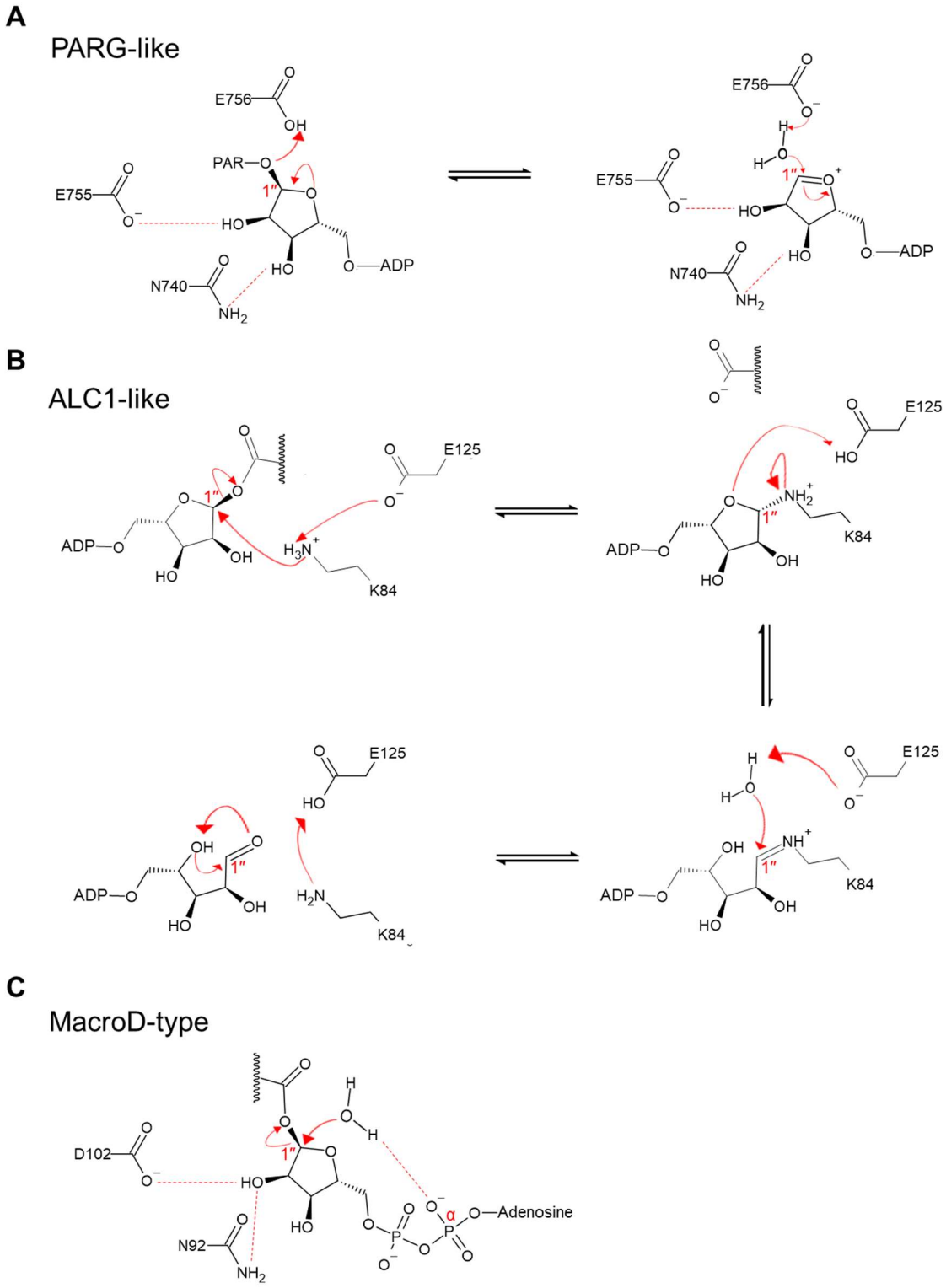

Figure 3: Proposed catalysis mechanisms of macrodomain hydrolases. **A**) Catalytic model of poly-ADP-ribose (PAR) hydrolysis by the PARG-like class. Side chain numbering according to human PARG (111 kDa splice variant). **B**) Hydrolysis mechanism of the ALC1-like class. Residues are numbered according to human TARG1. **C**) MacroD-type substrate-assisted hydrolysis. Side chain numbering according to human MacroD2.

3.4 Mac1 is a promising novel target against SARS-CoV-2

Since efficient evasion of innate immune response seems to be a hallmark of a CoV infection, therapeutic targeting of the underlying molecular mechanism could lead to potent antiviral drugs.

In light of the COVID-19 pandemic, novel targets came into focus. One of them is the conserved MacroD-like macrodomain (Mac1), which is encoded by SARS-CoV-2 open reading frame 1 (ORF1) and part of the transmembrane non-structural protein 3 (nsp3, Figure 4) (Rack et al., 2020b; Zimmermann et al., 2023).

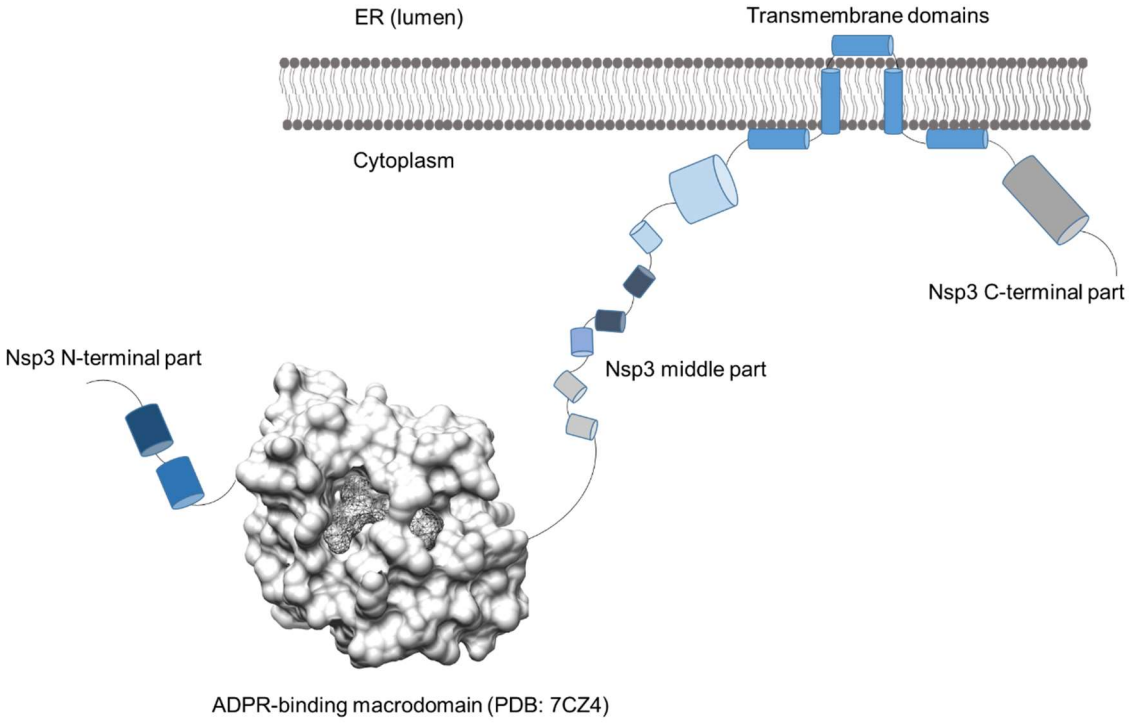

Figure 4: Mac1 is part of the non-structural protein 3 (nsp3) of SARS-CoV-2
Cartoon of SARS-CoV-2 nsp3 as multidomain protein inside a host cell. Nsp3 is anchored to the endoplasmatic reticulum (ER) with the macrodomain Mac1 located in the cytosol.

Interestingly, nsp3 of CoVs is known to be involved in the remodeling of the endoplasmatic reticulum (ER) leading to formation of convoluted membranes and double-membrane vesicles, which promotes viral propagation inside the cell (Lei et al., 2018). Apart from that, nsp3 generates pore complexes consisting of homohexamers that allow for molecule trafficking between the viral compartment

(lumen) and the cytoplasma (Zimmermann et al., 2023). Whilst this guarantees for constant exchange with the host and supply for the replication machinery, nsp3 has also been reported to directly suppress antiviral response (IFN) that is provoked when viral replication intermediats are recognized by the host (Lei et al., 2018).

Although the exact mechanism remains unclear, there is increasing evidence that Mac1 can directly interfere with cellular IFN signaling, presumably by reverting ADP-ribosylation (Alhammad & Fehr, 2020; Russo et al., 2021; Alhammad et al., 2023; Taha et al., 2023). In deed, Mac1 has been shown to have de-ADP-ribosylating activity (Rack et al., 2020b; Alhammad et al., 2021) and was recently reported as important virulence factor for SARS-CoV-2 *in vivo* (Alhammad et al., 2023; Taha et al., 2023). The same is true for other coronaviruses (e.g. SARS-CoV and MHV) (Fehr et al., 2016; Voth et al., 2021). Interestingly, so far, only a single point mutation was reported for Mac1 among the SARS-CoV-2 variants of concern (i.e. Pirola) (Heyer et al., 2022), which suggests that the macrodomain is under negative selection pressure, further emphasizing their vital role for the virus.

Furthermore, the macrodomain fold can be found in more than 150 viruses, such as coronaviruses, like SARS-CoV, *middle eastern respiratory syndrome coronavirus* (MERS-CoV) and *murine hepatitis virus* (MHV) as well as in alphaviruses, like *chikungunya virus* (CHIKV) (Alhammad & Fehr, 2020; Rack et al., 2020b; Fu et al., 2021).

Despite differences in amino acid sequence, the core motif of a typical macrodomain contains an α/β/α-sandwich, constituting a baseball glove-like binding pocket for ADPR, which is well conserved across different species, i.e. viruses, humans and even some bacteria (Figure 5A) (Rack et al., 2020a+b).

Surprisingly, evolutionary distinct macrodomains exhibit a highly similar binding mode for ADPR with only minimal differences in the vicinity of the terminal ribose as well as of the adenosine moiety across different crystal structures (Figure 5B).

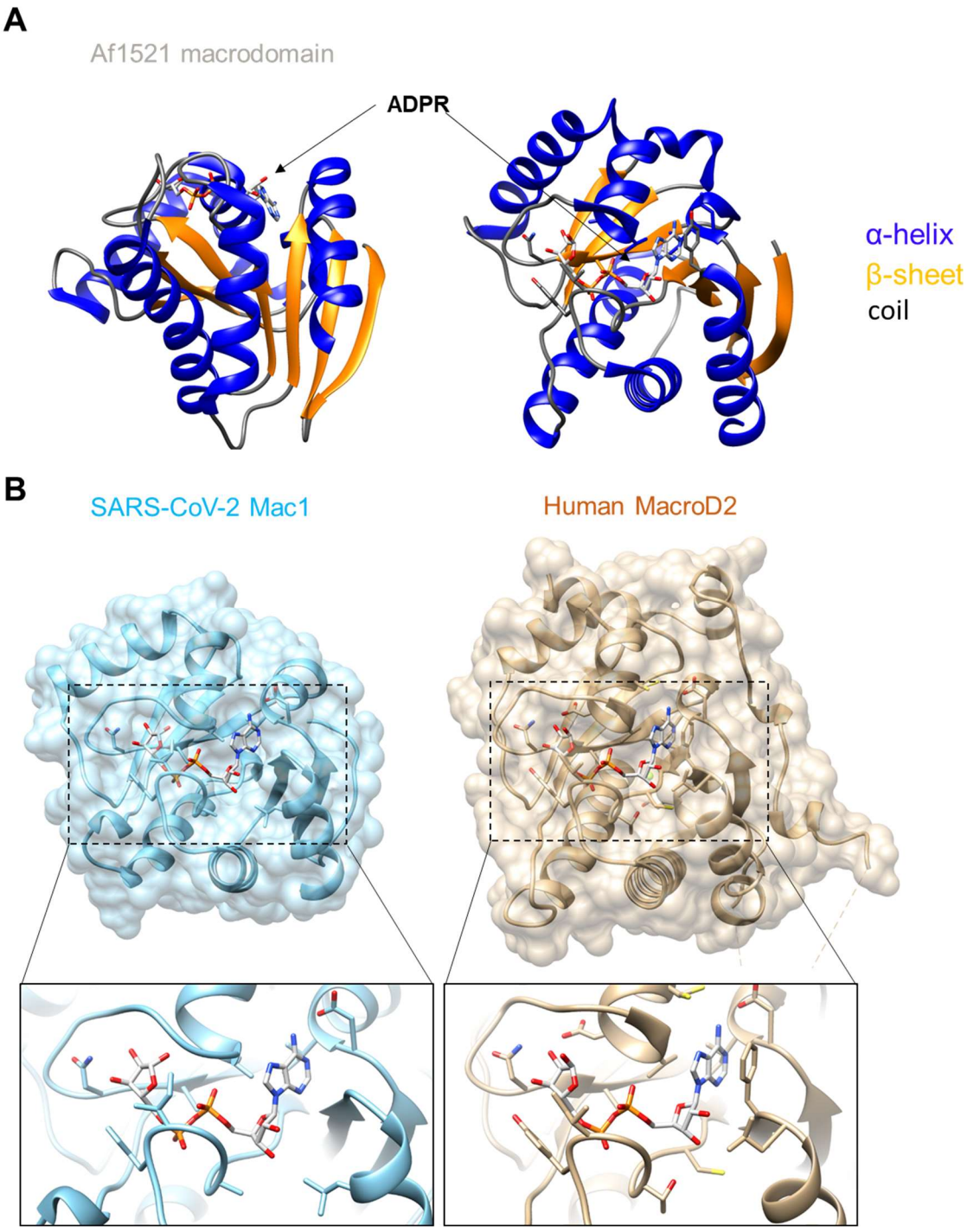

Figure 5: Macrodomains are structurally conserved ADPR binding motifs. **A**) Structure of the macrodomain Af1521 from *Archaeoglobus fulgidus* in complex with ADPR (PDB: 2BFQ) with the binding pocket in the side and top view respectively. **B**) ADPR-bound structures of Mac1 from SARS-CoV-2 (left, PDB: 6W02) and of human MacroD2 (right, PDB: 4IQY) as well as a zoom-in of the respective binding pockets (bottom).

Thus, ADPR appears always bound to the macrodomain in a bended (U-like) shape, which could be exploited for the design of promiscuous inhibitors in a ligand-based approach, whereas differences in the amino acid sequence might be exploited in order to improve selectivity for viral macrodomains (Rack et al., 2020b).

In conclusion, inhibition of the de-ADP-ribosylase activity of viral macrodomains could provide a novel therapeutic option against SARS-CoV-2 and might eventually lead to antivirals with pan-specific potential in the furture (Figure 6).

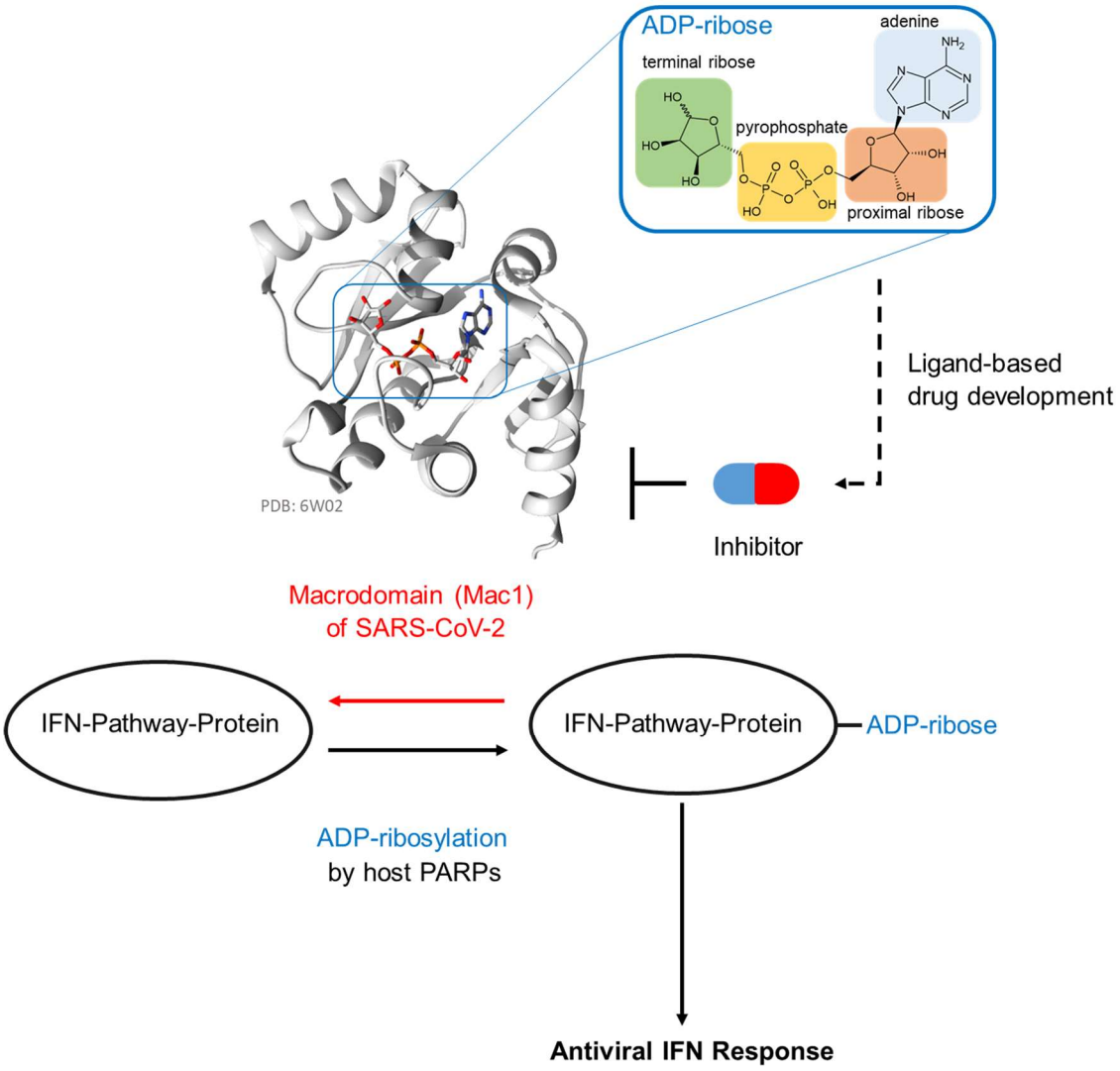

Figure 6: Expected antiviral effects of ligand-based Mac1 inhibitors.
Pharmacological inhibition of the de-ADP-ribosylating activity of Mac1 could restore the IFN-response upon a SARS-CoV-2 infection thereby preventing viral replication and disease progression.

3.5 Current status on Mac1 inhibitors

Since the viral macrodomains are important virulence factor for CoVs, pharmacological blockage of their enzymatic activity appears encouraging, not only for SARS-CoV-2 infections.

Although there have been already numerous, rather undirected approaches to identify inhibitors for the viral macrodomain, so far no promising drug candidates for Mac1 were found (Russo et al., 2021; Schuller et al., 2021; Dasovich et al., 2022; Roy et al., 2022; O'Connor et al., 2023). Many of these studies have applied molecular docking methods for pre-selection of potential Mac1 ligands. However, 69 inhibitor candidates that were proposed early by virtually screening failed to inhibit Mac1 in a cellular assay (Russo et al., 2021). Furthermore, a large fragment screening study showed that among a chemically diverse and large collection of ~ 2600 *in silico* predicted ligands, less than 10 % were found to bind Mac1, albeit with low affinity (IC_{50} = 190 µM) (Schuller et al., 2021). Also, most studies that primarily focused on high-throughput screens (HTS) of large compound libraries against the viral macrodomain had a low success rate < 0.04 % and the top hits exhibited only relatively poor potencies, i.e. IC_{50} values were between 37.5 - 57.5 µM and 6.1 - 8.5 µM respectively (Dasovich et al., 2022; Roy et al., 2022).

Until now, only a single study was able to present a few membrane permeable Mac1 ligands with affinities in the sub-micromolar range by combination of resource-intensive HTS and molecular modelling (Gahbauer et al., 2023).

In conclusion, Mac1 inhibition remains a challenging task and thus, new strategies are required to increase the repertoire of drug candidates that will eventually make it to the clinic.

4 Aim of the study

The primary goal of this work is the development of Mac1 inhibitors. Since pharmacological targeting of Mac1 has proven to be quite challenging, a dual strategy is chosen, comprising not only of screening of compounds that were *in silico* pre-selected for the Mac1 active site by Johannes Kirchmair (University of Vienna), but also includes, in contrast to previous studies, a more targeted approach by probing the viral macrodomain with a unique collection of ADPR and ADP analogues, This is also intended to generate structure-activity relationship (SAR) data. Finally, the acquired SAR data should improve our understanding of the interaction between Mac1 and its physiological ligand (ADPR) to guide the ligand-based design of drugs.

To this aim, protocols for the production of recombinant Mac1 and subsequent testing of compounds in ADP-ribosylhydrolase assays for both the viral as well as human macrodomains, i.e. MacroD1 and MacroD2 need to be established, that will allow for the identification of potential Mac1 modulators as well as their off-target assessment.

Utilization of orthogonal ligand binding studies should not only contribute to the SAR development but will also help to further characterize and refine novel Mac1 inhibitors, which will be finally evaluated in cellular assays regarding uptake, metabolization and toxicity.

5 Results

This chapter comprises data from the production and enzymatic characterization of Mac1, the development of assays for ADP-ribosylhydrolase activity monitoring, compound screening against Mac1 and the SAR-guided development of a novel Mac1 inhibitor as well as a preliminary pharmacological assessment.

5.1 Expression and Purification of SARS-CoV-2 Mac1

The MacroD-like macrodomain Mac1 of SARS-CoV-2 was expressed as gluthatione S-transferase (GST)-His_6-tagged fusion protein (46.7 kDa) in *E.coli* BL21 (DE3) Rosetta 2 using an autoinduction medium (Figure 7A). After mechanical cell lysis, the fusion protein was affinity purified via immobilized metal-ion affinity chromatography (IMAC, Figure 7B+C). For removal of the tag, the fusion protein was digested by His_6-tagged 3C protease (22 kDa), which resulted in almost complete cleavage (> 99 %) and release of Mac1 (18.5 kDa, Figure 7C).

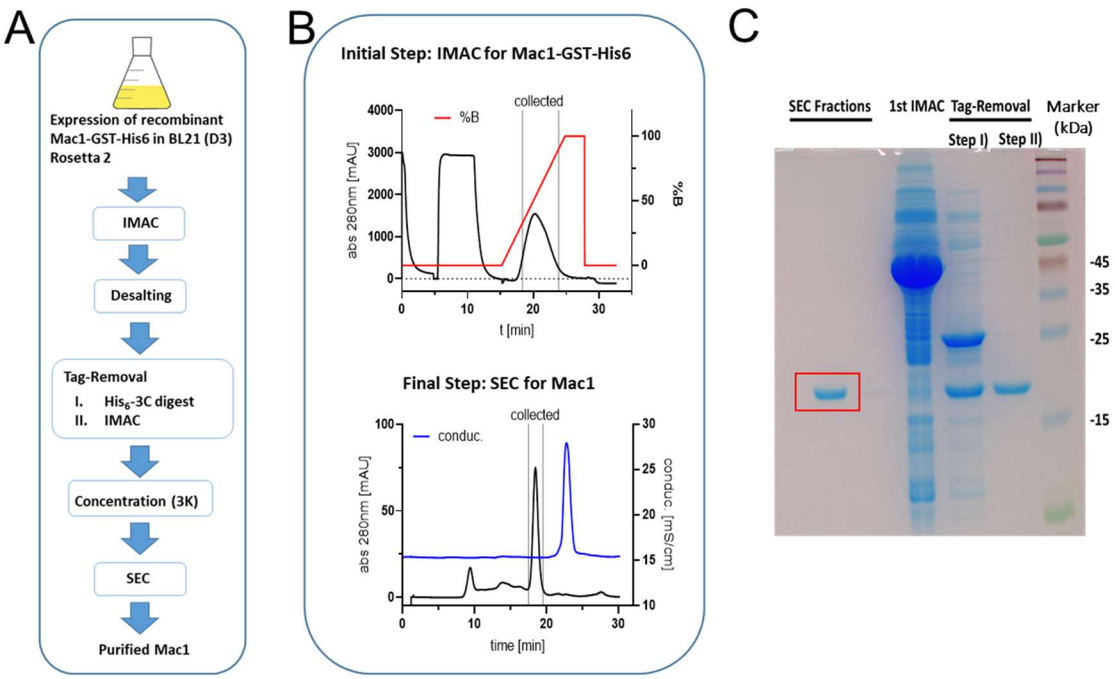

Figure 7: Production of the macrodomain Mac1 of SARS-CoV-2.
A) Outline of the purification strategy for the isolated Mac1 domain of SARS-CoV-2. **B**) Chromatogram from the purification of the Mac1-GST fusion protein by IMAC (top) and SEC chromatogram (bottom) from the final purification step of the isolated Mac1 domain. **C**) SDS-PAGE (stained with colloidal coomassie) of samples from different steps of the purification process. The red box marks the final product.

The reaction products were passed through a second IMAC to remove the 6xHis-Tag and the His_6-3C Protease, which yielded the isolated Mac1 at good purity (> 95 %). After a final round of polishing by size exclusion chromatography (SEC), pure Mac1 (> 99 %) was obtained (Figure 7B+C).

5.2 Investigation of the enzymatic properties of Mac1

The following chapters focus on the enzymatic characterization of the viral macrodomain and highlight potential substrates as well as some catalytically important aminoacids.

5.2.1 Identification of Mac1 substrates

Here, different N- and O-glycosidic nucleotides were tested for acceptance by Mac1 as substrate, which also lead to the development of a HPLC-assisted ADP-ribosylhydrolase assay.

5.2.1.1 Test of the N-glycosides α- and β-NAD

In addition to their natural substrates, mono-ADP-ribosylhydrolases can hydrolyse the α-anomer of NAD (Stevens et al. 2019). α-NAD can thus be used as a surrogate substrate in an enzymatic assay for this kind of enzyme (Wazir et al., 2021), because of its sterochemical similarity to an ADP-ribosylated protein (Figure 8).

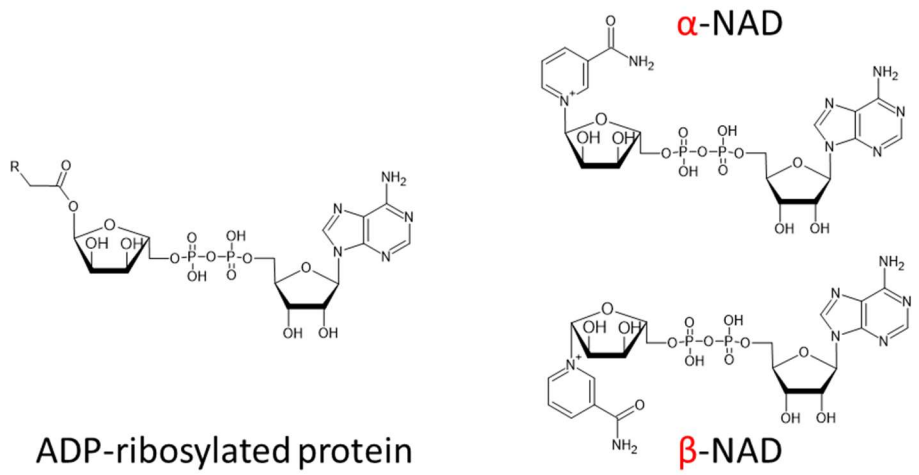

Figure 8: α-NAD mimicks the anomeric conformation of ADPR-conjugates.

Therefore, the isolated macrodomain Mac1 from SARS-CoV-2 was incubated with either α-NAD (Figure 9A + B) or β-NAD (Figure 9C + D). As a control, both substrates were incubated with the NADase from *Neurospora crassa*. While the viral macrodomain only hydrolysed α-NAD to produce ADPR and nicotinamide but not β-NAD (Figure 9A), NADase hydrolysed β-NAD but did not cleave α-NAD (Figure 9C).

From a substrate saturation plot the maximum reaction rate (v_{max} = 68 ± 16 pmol min^{-1} μg^{-1}) and the Michaelis-Menten constant (K_M = 0.18 ± 0.07 mM) for the hydrolysis of α-NAD by the viral macrodomain were determined (Figure 9E).

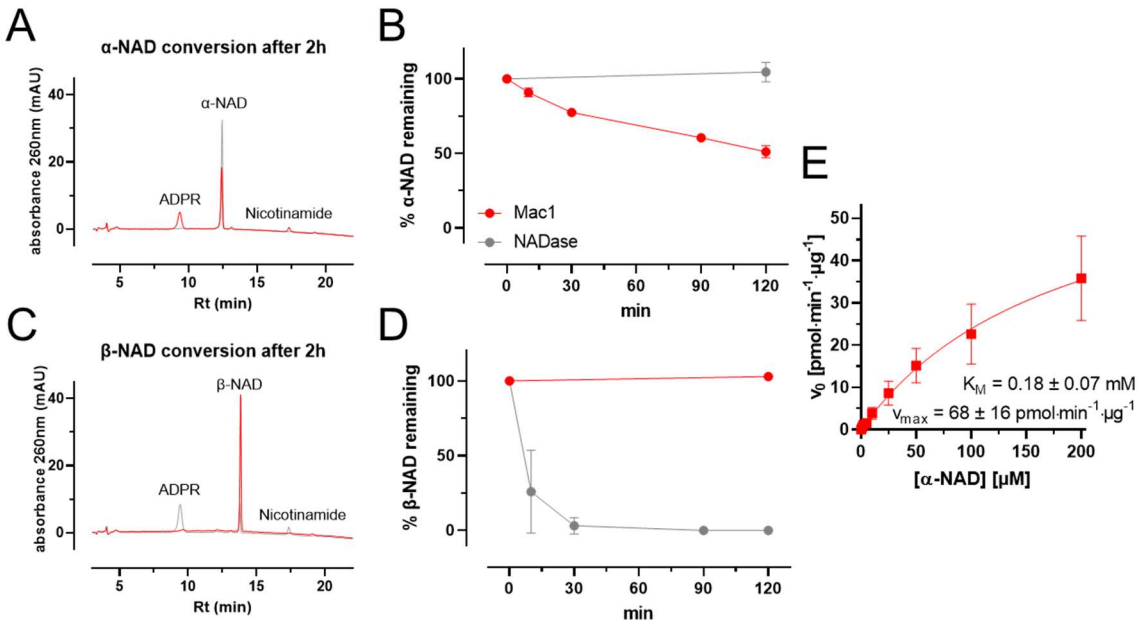

Figure 9: High performance liquid chromatography (HPLC)-based activity assay for Mac1.
A) HPLC chromatogram of the reaction products formed after 2 h incubation of 0.1 mM α-NAD with wildtype Mac1 (3 µM, red) or *Neurosporra crassa* NADase (2 µg/ µl, grey) and **B**) time course of the reaction. **C**) HPLC chromatogram of the reaction products formed after 2 h incubation of 0.1 mM β-NAD with wildtype Mac1 (3 µM, red) or *Neurosporra crassa* NADase (2 µg/ µl, grey) and **D**) time course of the reaction. **E**) Substrate saturation plot for Mac1 with α-NAD. Initial reaction rates were calculated from ADPR concentrations by HPLC. Data points are shown as mean ± SD (n ≥ 3) and were fit to a Michaelis-Menten model to derive K_M and v_{max}.

Furthermore, since the time course of the Mac1 catalyzed reaction (Figure 9B) indicated that the digest might not run to completion (plateau at ~ 50%), this suggested that ADPR, a product of this reaction, might act as a competitive inhibitor of the enzyme. This is consistent with the low micromolar affinity for the binding of ADPR to Mac1 (Figure 10), which is in agreement with previously reported K_D values (Frick et al., 2020; Michalska et al., 2020; Alhammad et al., 2021; Schuller et al., 2021).

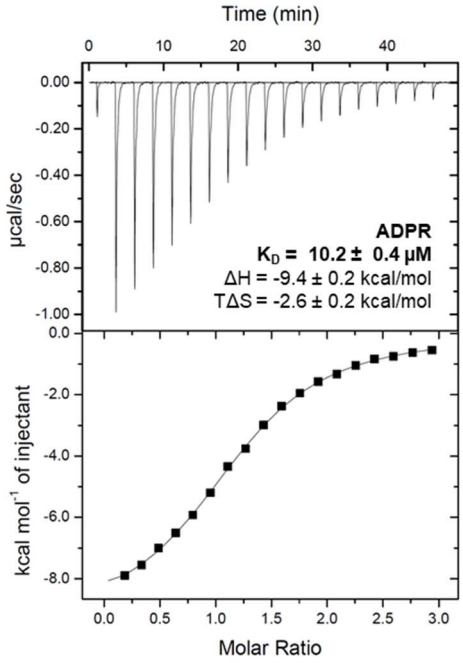

Figure 10: Isothermal titration calorimetry (ITC) of wildtype Mac1 binding to ADPR.
Top graph shows a representative baseline corrected thermogram for titration of 0.75 mM ADPR against 50 µM wildtype Mac1. The bottom graph depicts the integrated values of each titration point (squares) fitted to a one-site binding model (solid line). K_D, ΔH and TΔS are indicated as mean ± SD (n ≥ 3).

5.2.1.2 Test of the O-glycosides 1″-*O*-methyl-ADPR and TFMU-ADPR

In addition to the different N-glycosidic NAD variants, different O-glycosides were also tested. In solution, the anomeric configuration of the 1″-hydroxyl group is in an equilibrium between the α- or β-isomer, but methylation of the hydroxyl-group results in formation of full acetals, which stabilizes the respective anomeric configurations, allowing them to be individually tested on Mac1.

First, 1″-*O*-methyl-ADPR anomers were tested, which mimicks ADPR-conjugates of serines and nucleic acids (Figure 11A). However, no detectable ADPR was formed when either β- or α-1″-*O*-methyl-ADPR were incubated with the viral macrodomain (Figure 11B), indicating that both nucleotides were no Mac1 substrate.

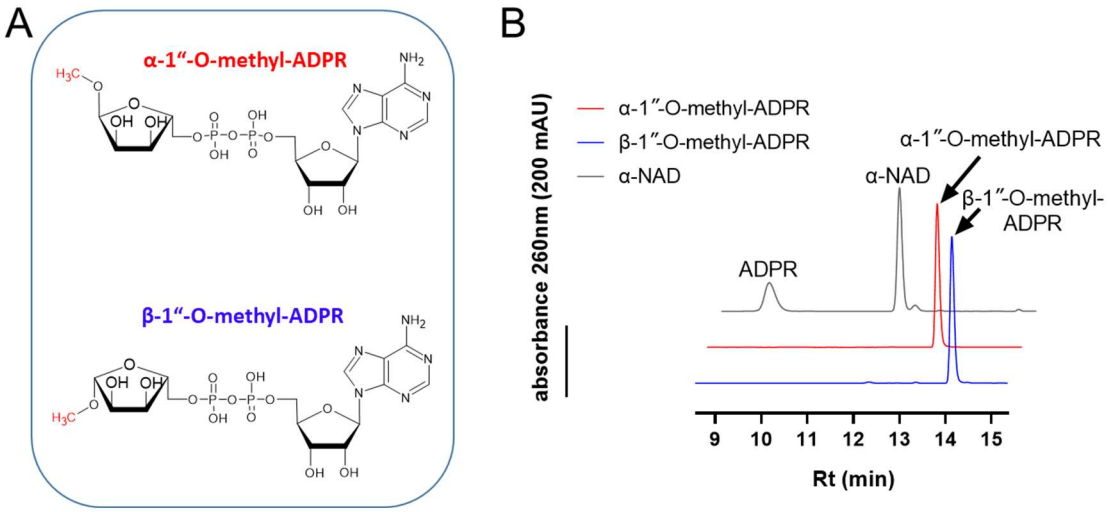

Figure 11: Neither α- nor β-anomeric 1″-*O*-methyl-ADPR were Mac1 substrates.
A) Chemical structures of the substrates and **B**) HPLC chromatograms for the reaction products (right) of wildtype Mac1 after 2 hours of incubation with 0.1 mM of either α-1″-*O*-methyl-ADPR (blue), β-1″-*O*-methyl-ADPR (red), or 0.1 mM α-NAD (grey) as control respectively.

Next, α-TFMU-ADPR was tested, as it was recently shown to be a substrate for continuous monitoring of human ADP-ribosyl-glycohydrolase activity (Drown et al., 2018).

The assay was adopted for Mac1 using similar conditions as for the previously established HPLC-assisted α-NAD assay and was carried out in a 96-well microplate fluorimeter (Figure 12A + B). Compared to the human PARG control, conversion of α-TFMU-ADPR to free TFMU by Mac1 was ~ 10-fold less, indicating poor substrate acceptance by the viral macrodomain.

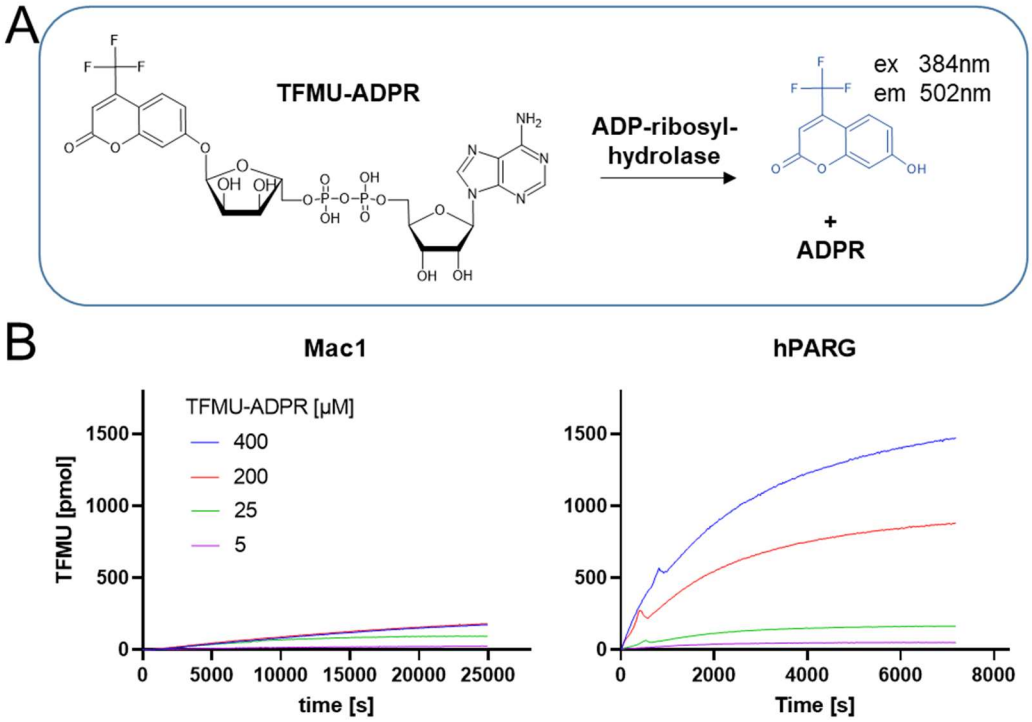

Figure 12: α-TFMU-ADPR is a poor substrate for Mac1.
A) Concept of the fluorimerter assay for continuous monitoring of enzymatic hydrolysis of TFMU-ADPR and **B**) the time-courses of TFMU formation corrected for chemical hydrolysis at the indicated substrate concentrations by either wildtype Mac1 (left) or human PARG (right) as control.

5.2.2 Investigation of functionally important protein residues by mutagenesis

As MacroD-type macrodomain, the most frequently discussed enzymatic mechanism for Mac1 is the substrate-assisted catalysis (Michalska et al., 2020; Rack et al., 2020b; Correy et al., 2022; Suskiewicz et al., 2023). This requires activation and coordination of a water nucleophile in close proximity to the C1″ to facilitate S_N2-mediated hydrolysis of the ADP-ribosylated substrate. In order to test for aminoacids that might be involved in that process, this chapter focuses on the effect of two distinct Mac1 point mutations (N40A and F132A) and their effect on ligand binding and catalytic activity (Figure 13).

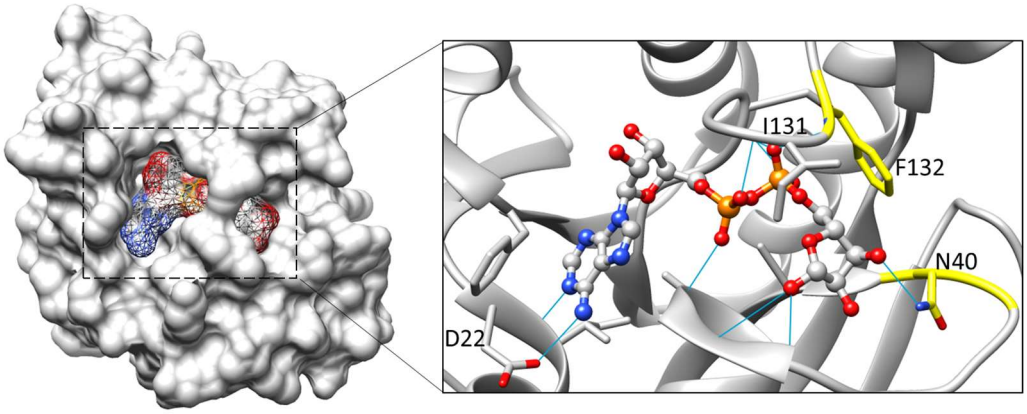

Figure 13: Structure of Mac1 in complex with ADPR.
Surface representation of the X-ray diffraction model for Mac1 (solid grey) bound to ADPR (colored meshed lines) from the protein data bank (PDB: 7CZ4) and a close up view of the binding site with the ligand as ball and stick representation and the protein as ribbon diagram. Blue lines indicate hydrogen bonds predicted by Chimera. The residues shown in yellow represent the point-mutated sites investigated.

5.2.2.1 Expression and enzymatic analysis of the N40A mutant

The first residue, asparagine 40 of Mac1 (Figure 13) was selected since a homologous mutation for alanine in the SARS-CoV macrodomain has been previously shown to abrogate ADP-ribosylhydrolase activity (Fehr et al., 2016).

First attempts to express the N40A mutant resulted in very low yield in comparison to wildtype Mac1, although the same production protocols were used (Figure 14A + B). Of note, protein stability prediction by the DUET onlinetool (https://biosig.lab.uq.edu.au/duet/, Pires et al., 2014, using PDB: 7CZ4 as reference structure) indicated a destabilizing effect after exchange of aspargine for alanine at this position (ΔΔG = -0.366 kcal/mol).

In addition, the catalytic activity of Mac1 N40A was completely abrogated as ADPR formation did not exceed the level of α-NAD chemical hydrolysis (Figure 15). Taken together, these results emphasize the importance of aspargine 40 for Mac1 stability, thereby enabling enzymatic function.

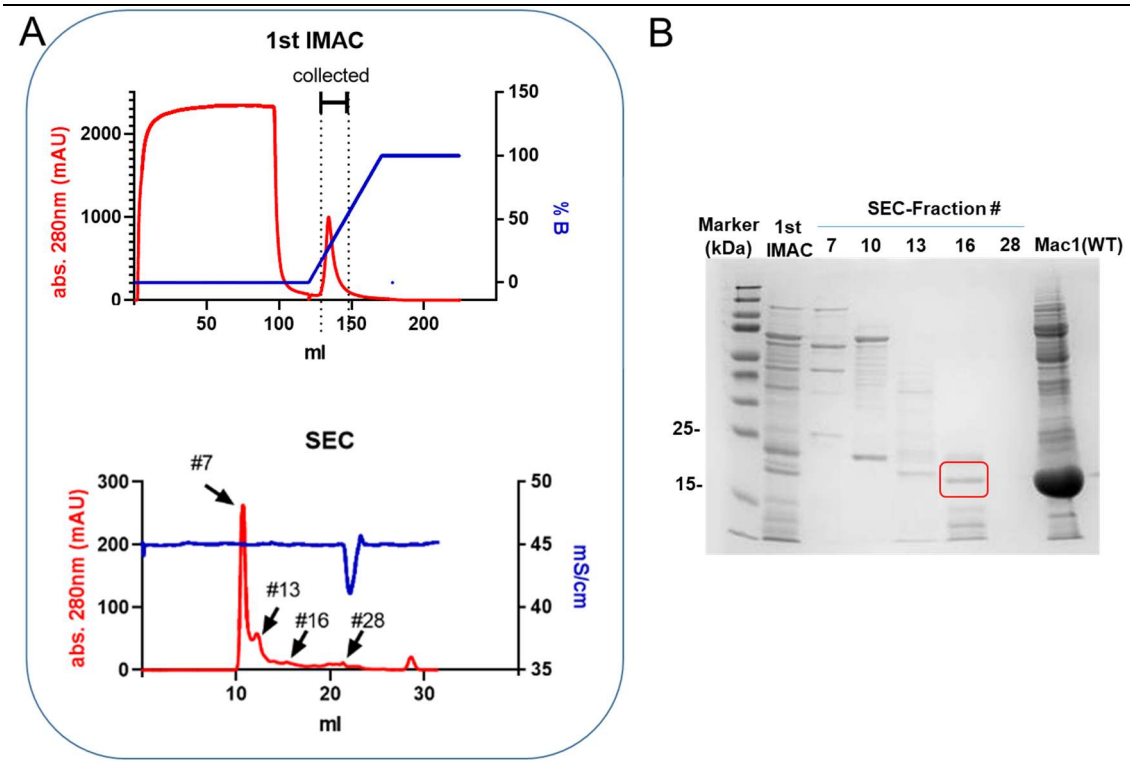

Figure 14: Production of the Mac1 mutant N40A.
A) Chromatograms of the IMAC (top) and SEC (bottom) as well as **B**) SDS-PAGE analysis of the different steps of the purification of N40A point-mutated Mac1. The red box marks the protein of interest.

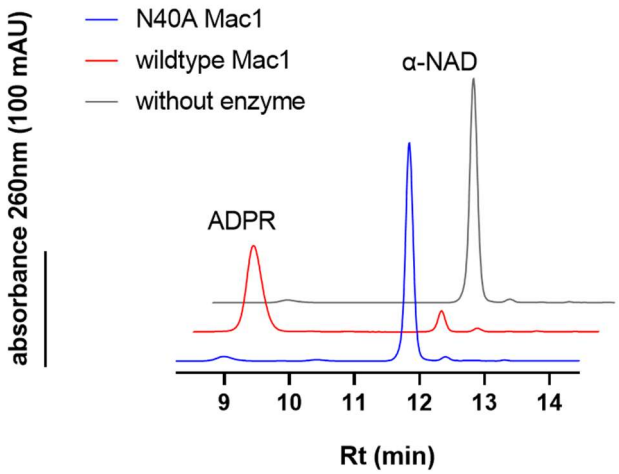

Figure 15: Mac1 N40A is catalytically inactive.
Shown are HPLC chromatograms of the reaction products of 0.1 mM α-NAD after incubation with either wildtype Mac1 (red), Mac1 N40A (blue) or without enzyme (grey) for 24 hours.

5.2.2.2 Biophysical and enzymatic analysis of the F132A mutant

Based on available high-resolution crystal structures (Figure 13), phenylalanine 132 was selected as interesting mutation site since it was hypothesized to constrain the terminal ribose in a more U-shaped conformation, thereby aiding the substrate-assisted catalysis of Mac1. Interestingly, ADPR binding affinity towards the F132A mutant was ~ 2-fold higher than for the wildtype (4.9 ±0.2 µM) due to higher net binding entropies (-0.8 ± 0.1 kcal/mol), whilst the released binding ethalphies were somewhat smaller (-8.0 ± 0.1 kcal/mol) (Figure 16A). In addition, the F132A mutant exhibited severely reduced catalytic activity, as ADPR formation was barely detectable above the chemical hydrolysis of α-NAD. In conclusion, phenylalanine 132 of Mac1 is important for ADP-ribosylhydrolase activity (Figure 16B).

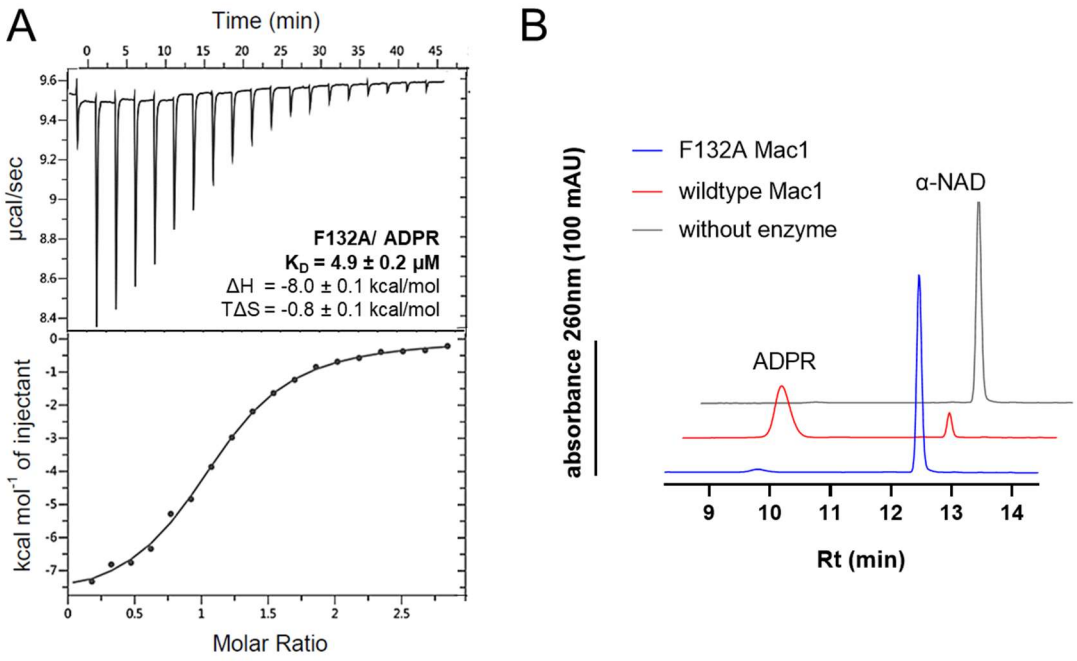

Figure 16: Mac1 F132A binds ADPR but has severely reduced catalytic activity.
A) Isothermal titration calorimetry (ITC) data are presented. Top graph shows a representative baseline corrected thermogram for titration of 0.75 mM ADPR against 50 µM Mac1 F132A. The bottom graph depicts the integrated values of each titration point fitted to a one-site binding model (solid line). The derived values K_D, ΔH and TΔS are indicated as mean ± SD (n ≥ 3).
B) HPLC chromatograms of the reaction products of 0.1 mM α-NAD after incubation with either wildtype Mac1 (red), Mac1 F132A (blue) or without enzyme (grey) for 20 hours.

5.3 Development of biochemical assays for monitoring of ADP-ribosyl-hydrolase activity

This chapter describes the development of activity-based enzyme assays for the viral macrodomain Mac1 as well as the human macrodomains MacroD1 and MacroD2.

5.3.1 Activity-based microplate assay for Mac1 Screening

Since HPLC analysis is limited to rather low sample throughput, a recently published post-reaction derivatisation method was adopted (Wazir et al., 2021) allowing for fluorescent detection of α-NAD and set up of a microplate endpoint assay for Mac1 inhibitor screens (Figure 17A).

Initially, linearity of the acetophenone-based method was confirmed (R^2 = 0.99, Figure 17B). Furthermore, as expected from a previous publication (Nakamura & Tamura, 1978), the derivatisation method was specific for the substrate α-NAD as well as other quaternary imines (β-NMN and β-NAD), whereas the expected hydrolysis products ADPR and nicotinamide were not derivatized (Figure 17B).

Next, based on the previously developed HPLC-assisted α-NAD assay, the conditions were optimized to meet the criteria for high-throughput inhibitor screening applications (Zhang et al., 1999; Acker & Auld, 2014).

Accordingly, assay sensitivity was optimized by competition trials that were conducted in 96-well microplates under different substrate concentrations. As product inhibition has been observed earlier for Mac1, ADPR was selected as model inhibitor. Consistently, ADPR showed competitive inhibition of Mac1 (IC_{50} ≈ 0.01-0.03 mM, Figure 17C) in the assay. Furthermore, IC_{50} values gradually decreased at low substrate concentrations reaching a minimum at < 30 µM α-NAD (~16% K_M, Figure 17C).

In order to guarantee assay robustness, a sufficiently high signal window (SW) had to be maintained and the assay variability ratio (AVR) minimized. As the latter was achieved by standardizing of the assay components (protein, substrate, media and plastic ware) and semi-automated, parallelized liquid and sample handling, the signal window was adressed by an increase of substrate

conversion. Therefore, enzyme reactions were allowed to proceed until 80% completion (~90 min), whilst an initial α-NAD concentration of 10 µM (~5% K_M) finally yielded a robust screening assay with a Z′-factor > 0.6 (SW > 5.7, AVR < 0.4, Figure 17D).

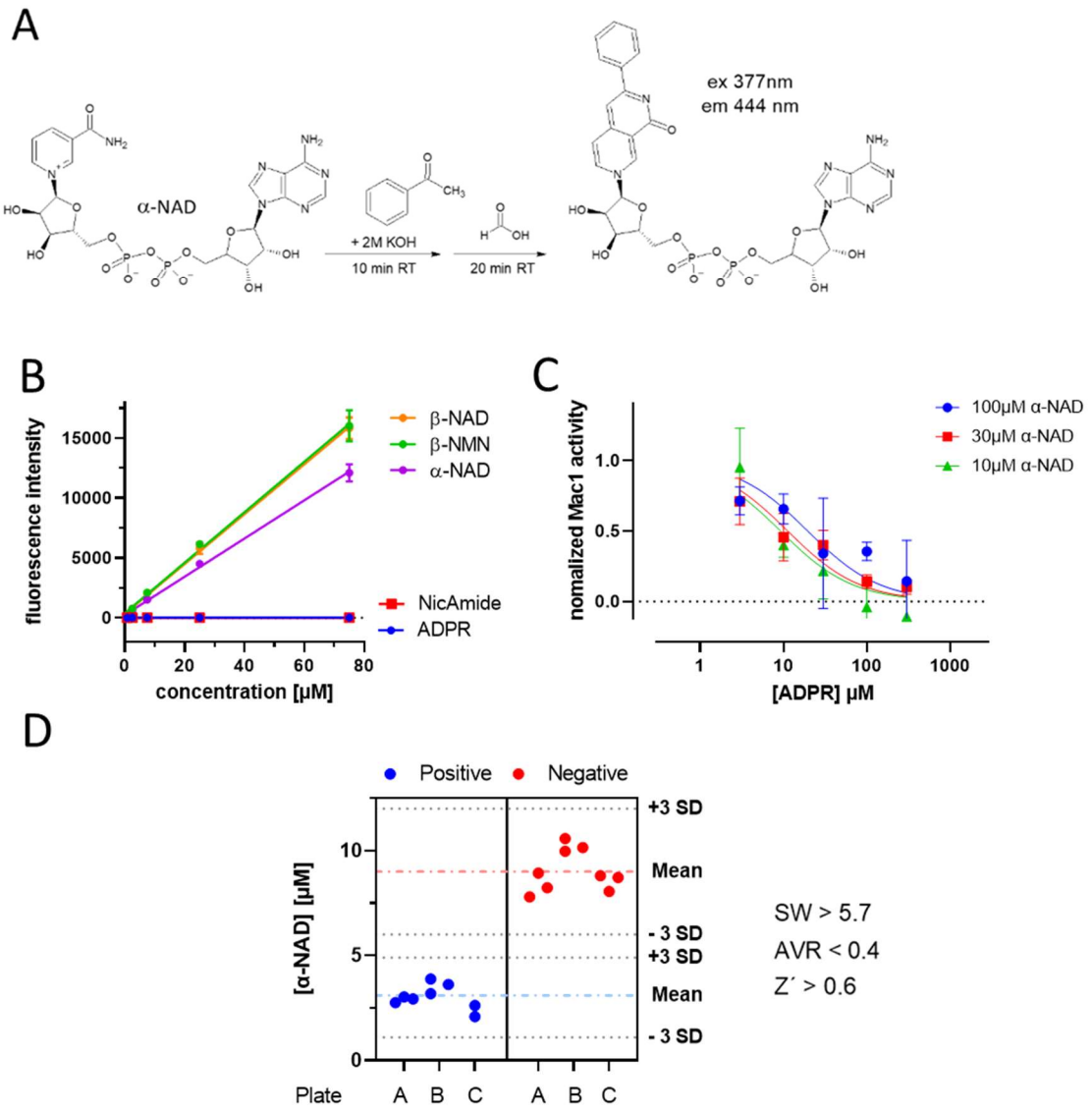

Figure 17: Fluorescent α-NAD depletion assay for Mac1 activity screening.
A) Outline of the post-reaction derivatisation of α-NAD for quantification of enzyme activity by substrate depletion. **B**) Test of the specificity and linearity of the derivatisation reaction for the educts and the expected hydrolysis products respectively. Data are shown as mean ± SD (n ≥ 3). **C**) Concentration-responses for inhibition of wildtype Mac1 with ADPR at different α-NAD concentrations fitted by sigmoidal function. Data are shown as mean ± SD from three technical replicates. **D**) Evaluation of the assay performance in 96-well format. Shown are the remaining α-NAD levels after co-incubation with (positive control) or without Mac1 (negative control) of 3 independent assays (plate A-C) to determine signal window (SW), assay variability ratio (AVR) and robustness (Z´).

5.3.2 Comparison between the plate and the HPLC-assisted Assay

To test for assay comparability, we used the ADPR analogue 8-Br-ADPR as competitor in both the HPLC- and microplate α-NAD assay. In both cases, 8-Br-ADPR acted as Mac1 inhibitor and the derived concentration responses were not significantly different (IC_{50} = 40 ± 7 µM by HPLC- and 48 ± 4 µM by microplate assay), indicating good comparability between the assays (Figure 18A).

In addition, the same competition assays were conducted with the human macrodomains MacroD1 and MacroD2. Using assay conditions, that were established previously for the HPLC and microplate setup (Ocenas, 2022), the measured concentration responses of 8-Br-ADPR were in good agreement for MacroD1 (IC_{50} = 16 ± 2 µM by HPLC and 19 ± 2 µM by plate assay) and MacroD2 (IC_{50} = 52 ± 21 µM by HPLC and 32 ± 3 µM by plate assay) respectively (Figure 18B).

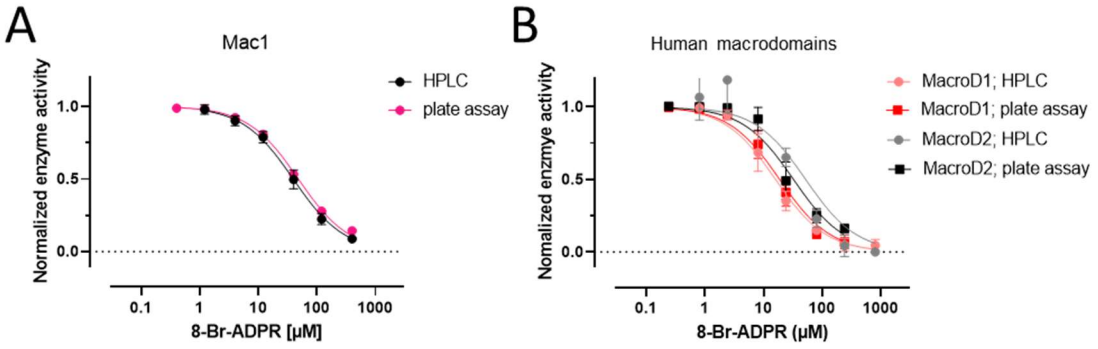

Figure 18: HPLC-based and microplate α-NAD assay yield comparable results.
Concentration response of 8-Br-ADPR for **A**) 3 µM Mac1 as well as **B**) 1 µM MacroD1 and 3 µM MacroD2 obtained in the microplate or the HPLC-assisted α-NAD assay respectively. Data were fitted by a sigmoidal function and are shown as mean ± SD (n ≥ 3).

5.3.3 HPLC-assisted de-MARylation Assay

For testing of inhibitor potency against the de-ADP-ribosylating activity of Mac1 and to assess off-target effects on MacroD1 and MacroD2, a de-MARylation assay was developed. Human PARP10 was selected as substrate, which was previously described to be de-ADP-ribosylated by viral and human macrodomains (Alhammad et al. 2021).

The first pilot experiments were conducted with Mac1. Here, an auto-ADP-ribosylated PARP10-GST fusion protein was incubated with the viral macrodomain and the release of ADPR was quantified by HPLC over time (Figure 19A). Remarkably, Mac1-mediated de-MARylation progressed quickly and reached a plateu already after 30 min, whilst chemical hydrolysis of the substrate steadily continued making up to ~25% of the total released ADPR after 120 min (Figure 19B). Thus, incubation times for the de-MARylation assay were limited to 30 min. Since this assay was not intended for high-throughput screening, a rather low substrate conversion rate was preferred to ameliorate product inhibiton. To account for that and to optimize assay sensitivity for inhibitors with high affinity, Mac1 concentrations were titrated. Among the tested concentrations, 0.3 µM Mac1 showed a considerably low conversion of the MARylated PARP10, whilst being still above the chemical hydrolysis level (Figure 19C). Finally, as proof-of concept, concentration responses of 8-Br-ADPR were measured for both viral and human macrodomains using the previously established assay conditions, whilst enzyme concentrations for MacroD1 and MacroD2 were kept as in the α-NAD assays. Interestingly, the derived IC_{50} values of 8-Br-ADPR for MacroD1 (0.09 ± 0.02 mM) and MacroD2 (0.04 ± 0.01 mM) in the de-MARylation assay were in good agreement with the α-NAD assays (Figure 19D). In contrast, the IC_{50} value of 8-Br-ADPR for Mac1 in the de-MARylation assay was somewhat higher (0.3 ± 0.2 mM) than in the α-NAD assays, hinting towards a higher affinity of the viral macrodomain for auto-modified PARP10 compared to α-NAD.

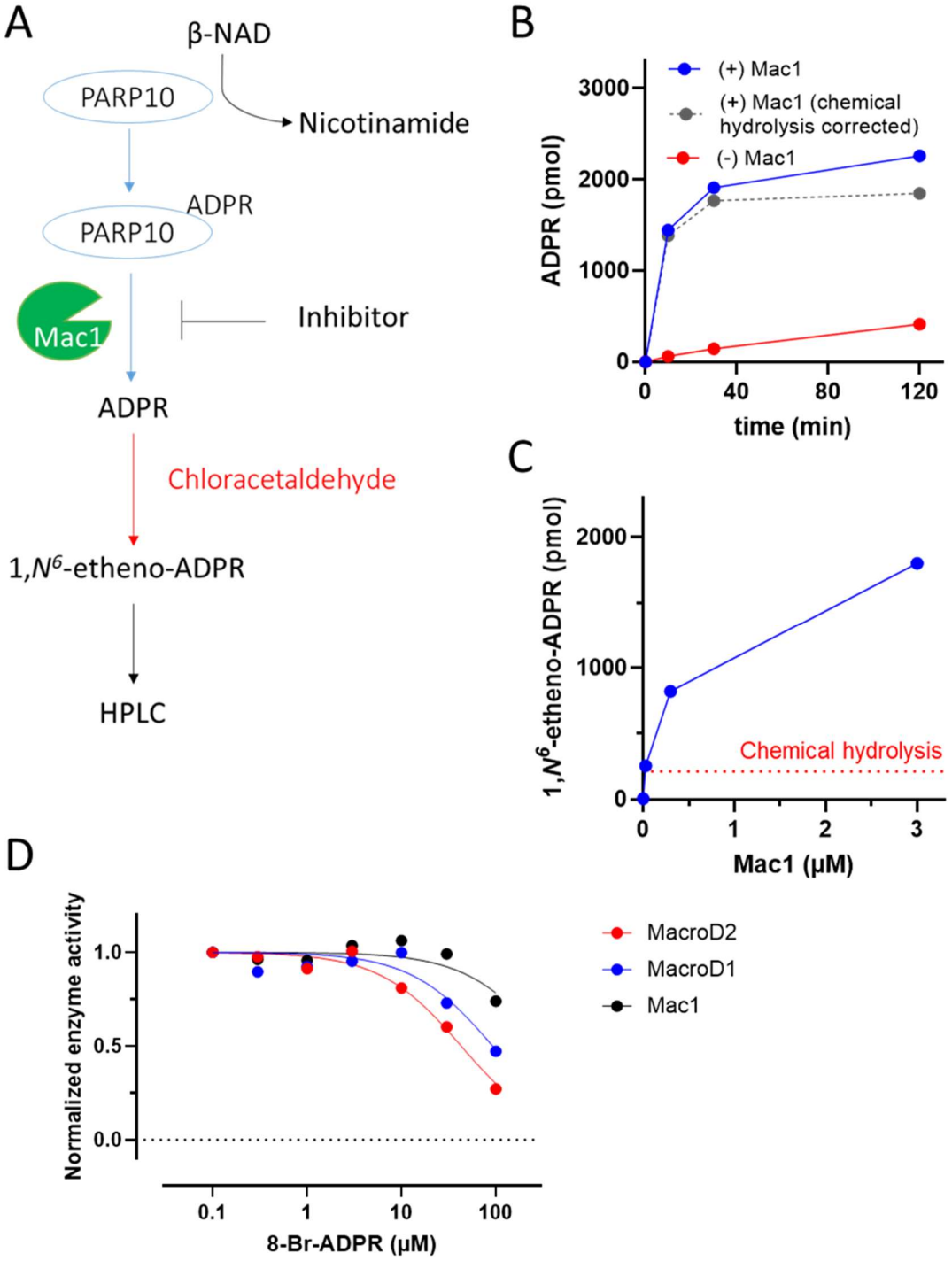

Figure 19: De-MARylation assay for macrodomains.
A) Outline of the assay principle. **B**) HPLC analysis of free ADPR from MARylated PARP10 after incubation with Mac1 (wildtype, 3 µM) or without Mac1 at the indicated timepoints and **C**) final yield of 1,N^6-etheno-ADPR corrected for chemical hydrolysis of the substrate after incubation for 30 min at the indicated Mac1 (wildtype) concentrations. **D**) Concentration response of 8-Br-ADPR after 30 min incubation with either 0.3 µM Mac1, 1 µM human MacroD1 or 3 µM human MacroD2 respectively. Data were fitted by a sigmoidal function.

5.4 Mac1 Inhibitor Screenings

The following chapters describe the test and identification of initial inhibitor candidates and lead structures from various compound libraries assorted for Mac1 by either virtual screening or rational considerations. Furthermore, an initial structure-activity relationship for Mac1 binding to an ADP-ribosylated substrate will be presented.

5.4.1 Test of virtually pre-screened small molecule drug candidates

As first compound panel, 28 drug-like small molecules of *in silico* modelled Mac1 ligands by Johannes Kirchmaier (University of Vienna) were screened against the viral macrodomain using the α-NAD microplate assay (Figure 20A).

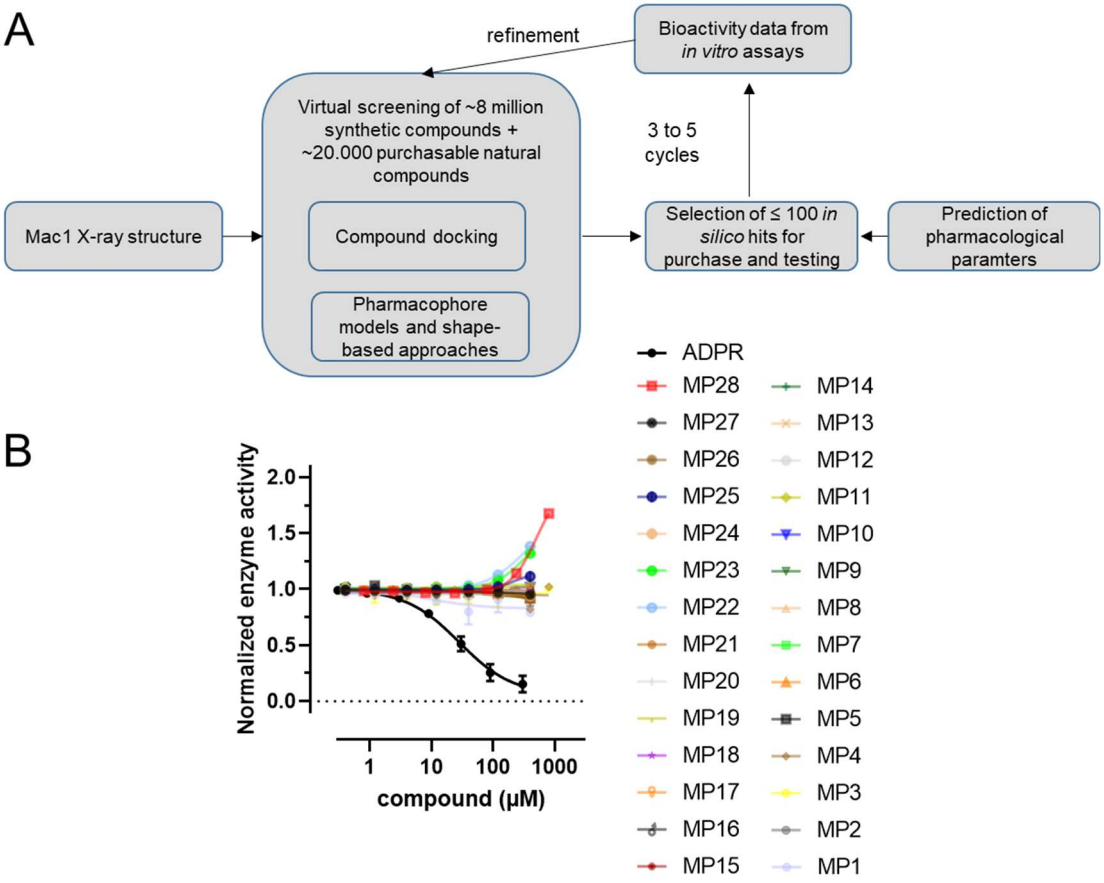

Figure 20: No promising Mac1 inhibitors in a chemically diverse library of virtually pre-selected compounds.
A) Outline of the virtual pre-screening of Mac1 inhibitor candidates conducted by Johannes Kirchmaier and **B**) corresponding concentration responses of the compounds tested in the α-NAD microplate assay for Mac1. ADPR was used as inhibition control. Data were fitted using a sigmoidal function and are shown as mean ± SD (n ≥ 1)

With exception of four potential modulators, none of the compounds showed readable signs of effecting Mac1 activity (Figure 20B). Among these four small molecules, only one (MP1) seemed to have partial inhibition of Mac1 by ~10%, whereas the rest (MP12, MP23 and MP28) appeared to have an activating effect at concentrations > 0.1 mM.

In addition, a number of previously published *in silico* predicted Mac1 ligands (Selvaraj et al., 2021) and compounds from commercially available screening libraries for the viral macrodomain were sourced and screened against Mac1 by the α-NAD microplate assay (Figure 21). Among these, four potential modulators were identified. Telmisartan and α-Estradiol appeared to have weak inhibitory potential (IC_{50} > 400 µM), whereas ZINC8792474 and ZINC8879336 seemed to exhibit activating effects on Mac1 at concentrations > 0.1 mM.

Taken together, no promising inhibitor candidate could be identified from the two screening rounds of virtually predicted Mac1 ligands.

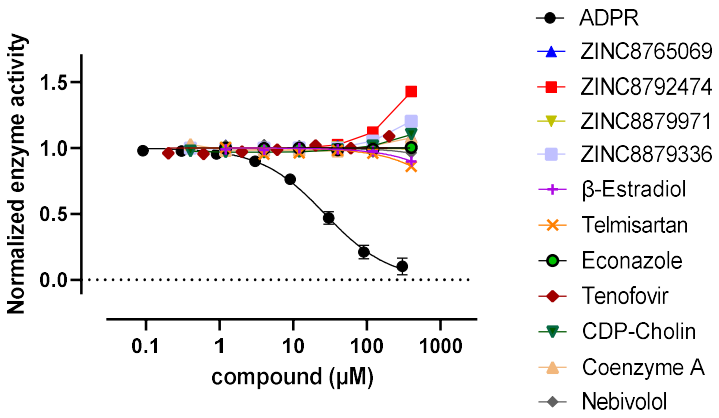

Figure 21: Poor inhibitory potential of *in silico* predicted Mac1 ligands. Concentration response of the compounds tested in the previously established microplate assay for Mac1. ADPR was used as inhibition control. Data were fitted by a sigmoidal function and are shown as mean ± SD (n ≥ 1).

5.4.2 Probing of ADPR analogues and structure-activity relationship (SAR) development

As the first two screening rounds failed to provide potent Mac1 inhibitors, a more targeted approach was chosen for the next round. Based on the previous observation that free ADPR impairs Mac1 activity, a unique collection of > 40 ADPR derivatives with modifications at different functional groups (Figure 22)

was used to investigate the complex interaction between Mac1 and an ADP-ribosylated substrate.

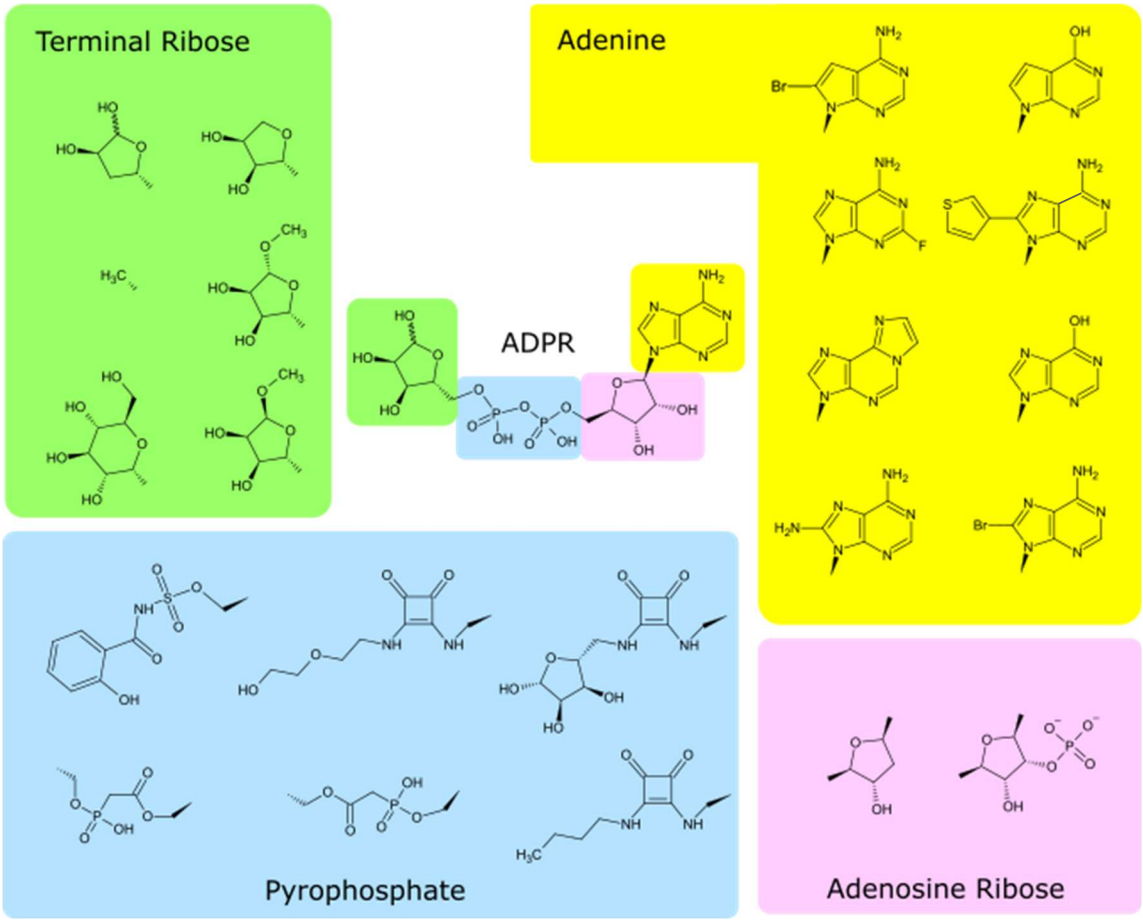

Figure 22: Selection of the ADPR analogues tested in this work.
Shown are chemical structures of the parental nucleotide (ADPR) and the respective modifications at the different functional groups.

5.4.2.1 Adenosine panel

ADPR analogues with different modifications at the adenine base were probed (Figure 23) and were summarized in Table 1. Whilst ADPR inhibited Mac1 in the low micromolar range (IC_{50} = 24 ± 5 µM), derivatisation of the adenine´s base resulted in generally less potent Mac1 inhibitors, indicating a low tolerance towards changes in the adenine moiety and arguing for a high substrate specificity.

In line with that, substitution of the hydrogen-bond-donor N6 for oxygen (IDPR, 7-deaza-IDPR), or the introduction of an etheno-modification bridging between the N1 and N6 (1,N^6-etheno-ADPR) abrogated Mac1 inhibition, indicating crucial ligand-enzyme interactions at these positions.

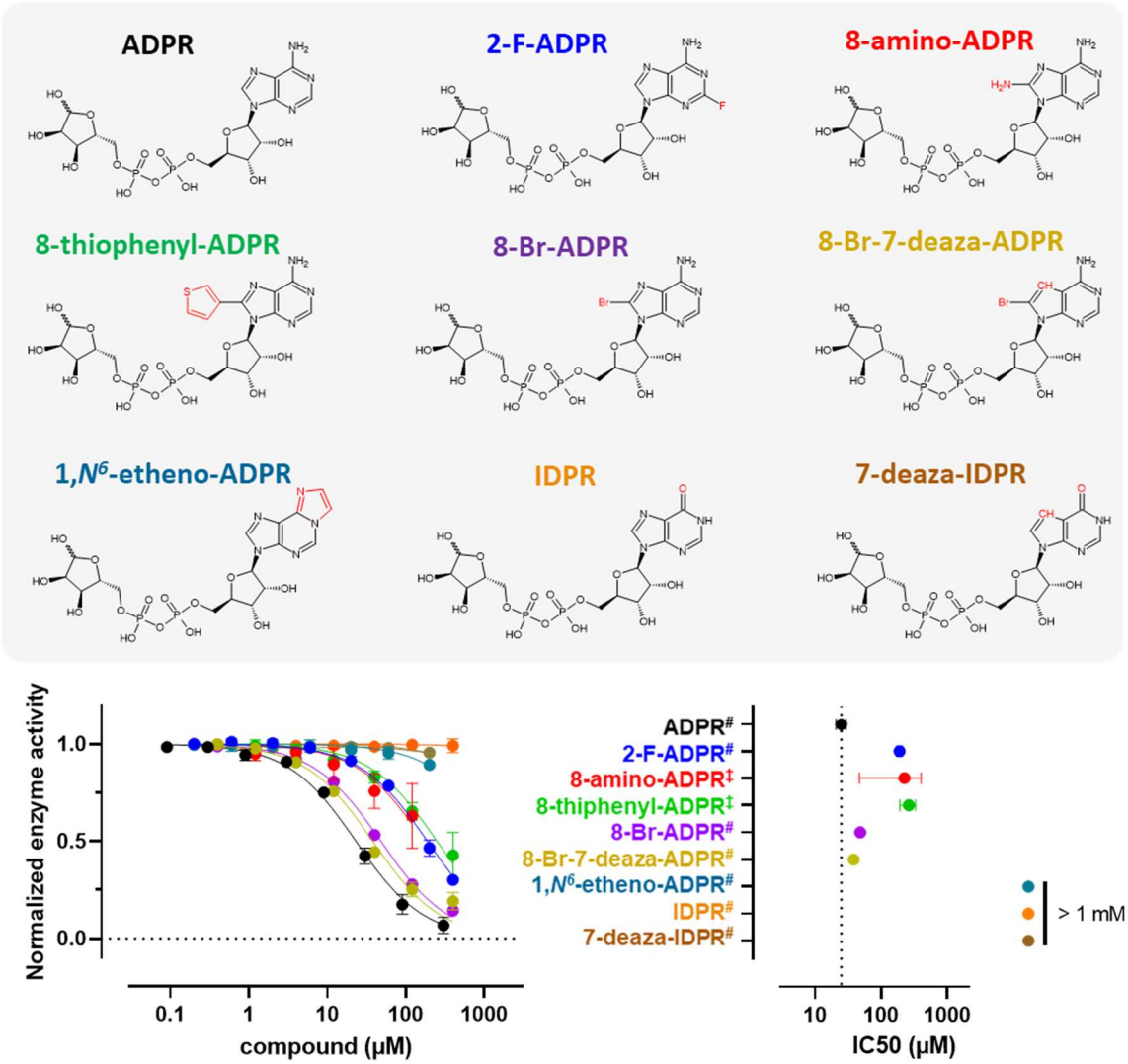

Figure 23: Effect of purine base-modified ADPR derivatives on Mac1 activity.
Shown are the chemical structures of the tested compounds (top) and the corresponding concentration responses for Mac1 (bottom left) obtained by the previously established microplate (#) or the HPLC-assisted α-NAD assay (‡) respectively. Curves were fitted by a sigmoidal function and the derived IC_{50} values are summarized (bottom right). For comparison, the previous plate assay dataset for 8-Br-ADPR was included. Data are shown as mean ± SD (n ≥ 3).

Addressing the 2-position of the adenine by testing 2-F-ADPR on Mac1 showed a ~7-fold lower inhibitory potency than ADPR (IC_{50} = 190 ± 20 µM).

Next, modifications at the C8 were tested. 8-thiophenyl-ADPR showed a ~10-fold lower inhibitory potency than ADPR (IC_{50} = 260 ± 70 µM).

In contrast, increasing polarity at the C8 of ADPR by addition of an amino-group (8-amino-ADPR) had no significant effect on Mac1 inhibition (IC_{50} = 224 ± 177 µM).

To test if the inhibitory effect might correlate with size of the substituent at the C8, 8-brominated ADPR analogues were investigated, due to the rather small size of a bromine compared to apolar organic substituents (i.e. thiophenyl).

Both, the initially tested 8-Br-ADPR as well as the derivative 8-Br-7-deaza-ADPR were > 5-fold more potent inhibitors than the other C8-modified compounds (IC_{50} = 48 ± 4 µM and 38 ± 6 µM), which suggested that bulky adducts at the C8 of the adenine negatively affect inhibitory potential.

The concentration response of 8-Br-ADPR and 8-Br-7-deaza-ADPR did not significantly differ, which was further investigated in orthogonal binding studies (Figure 24, Table 1).

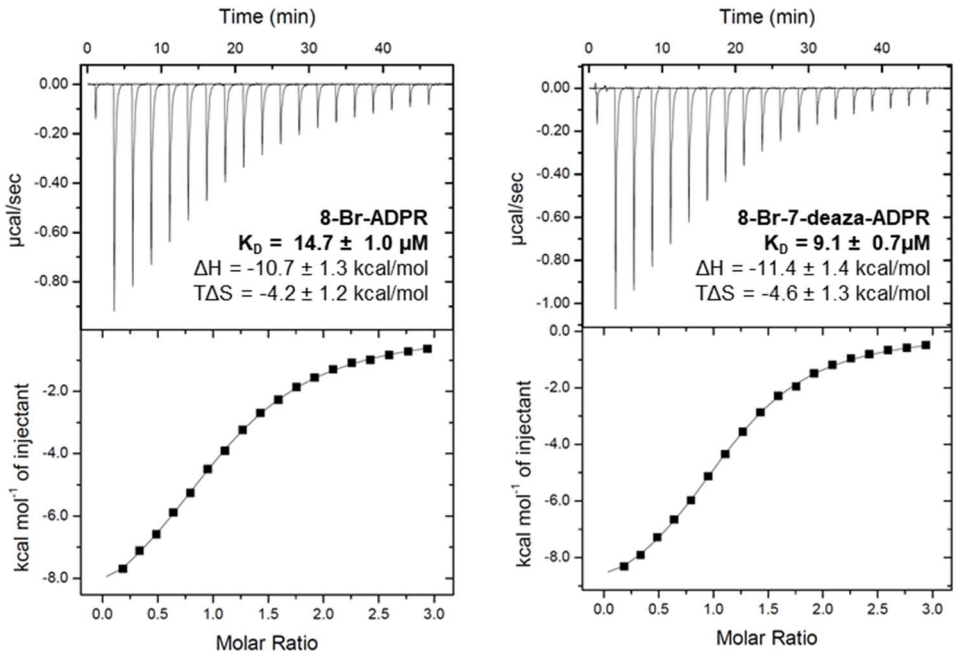

Figure 24: Binding of 8-Br-ADPR and 8-Br-7-deaza-ADPR to Mac1.
Isothermal titration calorimetry (ITC) data are presented. Top graphs show representative baseline corrected thermograms for titration of 0.75 mM of the respective compounds against 50 µM wildtype Mac1. The bottom graphs depict the integrated values of each titration point (squares) fitted to a one-site binding model (solid line). The derived values for K_D, ΔH and TΔS are indictated as mean ± SD (n ≥ 3).

Whilst K_D values for 8-Br-ADPR reflected the decreased inhibitory potency against Mac1 (K_D = 14.7 ± 1.0 µM), the binding affinity for 8-Br-7-deaza-ADPR

was not significantly different to ADPR (K_D = 9.1 ± 0.7µM), which confirmed that the 7-deaza-modification of the adenine base increases inhibitor affinity.
Furthermore, net binding enthalpies were higher for both 8-brominated ADPR analogues, which only partially compensated for the high entropic penalties due to the substituent at C8.

Table 1: Summary of the inhibitory potency and affinity of purine base modified ADPR analogues towards Mac1.

Compound	IC_{50} (µM)	K_D (µM)
ADPR	24 ± 5	10.2 ± 0.4
2-F-ADPR	190 ± 20	n.d.
8-amino-ADPR	224 ± 177	n.d.
8-thiophenyl-ADPR	260 ± 70	n.d.
8-Br-ADPR	48 ± 4	14.7 ± 1.0
8-Br-7-deaza-ADPR	38 ± 6	9.1 ± 0.7
1,N^6-etheno-ADPR	> 1000	n.d.
IDPR	>> 1000	n.d.
7-deaza-IDPR	> 1000	n.d.

n.d.: not determined.

In order to confirm the findings from the ADPR panel, an additional panel of ADP-derivatives containing similar modifications was screened (Figure 25) and the results are summarized in Table 2.
Thus, a 7-deaza-modification of ADP showed across different structures, i.e. 7-deaza-ADP (IC_{50} = 1.2 ± 0.3 mM) and 7-deaza-2′-deoxy-ADP (IC_{50} = 2.7 ± 0.3 mM) significantly lower IC_{50} values compared to the respective parental nucleotides ADP and 2′-deoxy-ADP (IC_{50} = 4.3 ± 0.2 mM and 5.8 ± 0.2 mM), which confirmed the apparent trend towards better Mac1 inhibition seen for 8-Br-7-deaza-ADPR (compared to 8-Br-ADPR).
Interestingly, 8-amino-ADP showed a somewhat higher IC_{50} value than ADP (IC_{50} = 5.8 ± 2.3 mM), which is in line with the same trend towards lower inhibitory potency for 8-amino-ADPR (compared to ADPR). Together with the observations

for thiophenyl-ADPR this might hint that modifications of the C8 are disfavored independent of group polarity.

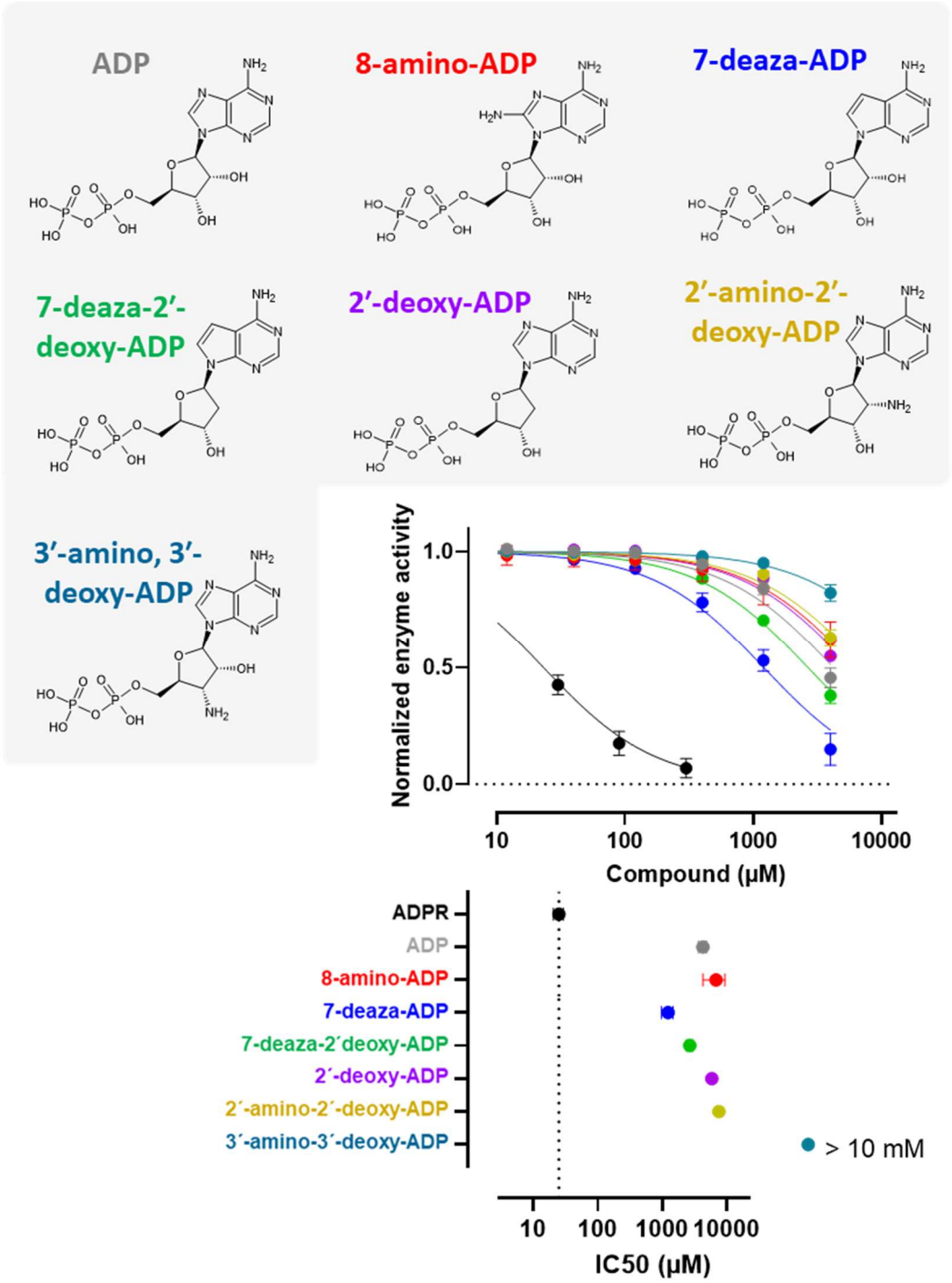

Figure 25: Effect of ADP derivatives on Mac1 activity.
Shown are the chemical structures of the tested compounds (top) and the corresponding concentration responses for Mac1 (mid right), which were obtained by the previously established microplate assay. Curves were fitted by a sigmoidal function and the derived IC_{50} values are summarized (bottom right). For comparison, the previous dataset for ADPR was included. Data are shown as mean ± SD (n ≥ 3).

Table 2: Summary of the inhibitory potency of purine base-modified ADP derivatives towards Mac1.

Compound	IC_{50} (mM)
ADP	4.3 ± 0.2
8-amino-ADP	6.8 ± 2.5
7-deaza-ADP	1.2 ± 0.3
7-deaza-2′-deoxy-ADP	2.7 ± 0.3
2′-deoxy-ADP	5.8 ± 0.2
2′-amino-2′-deoxy-ADP	7.6 ± 1.3
3′-amino-3′-deoxy-ADP	> 10

5.4.2.2 Ribose panel

To further elucidate the role of the sugar moieties for Mac1 inhibition, the role of ribose-modified ADP derivatives was tested initially (Figure 25).

Overall, the ADP derivatives used in this study were less potent inhibitors and started to compete with the Mac1 substrate in the millimolar range, highlighting the importance of the terminal ribose for Mac1 ligand engagement.

Interestingly, 2′-deoxy-ADP as well as 2′-amino-2′-deoxy-ADP were significantly less potent inhibitors than ADP (IC_{50} = 5.8 ± 0.2 mM and 7.6 ± 1.3 mM respectively) and substitution of the 3′-OH of ADP for an amino-group further increased IC_{50} values (3′-amino-3′-deoxy-ADP, IC_{50} > 10 mM).

These findings were also in agreement with enzyme activity data for ADPR analogues with similar modifications at the adenosine ribose (Figure 26, 27), which were summarized in Table 3. Thus, phosphorylation of the 2′-hydroxyl group (ADPRP), removal of 2′-OH (2′-deoxy-ADPR) or substitution via fluorine (2′-F-,2′-deoxy-ADPR) resulted in only mild, yet measurable increase of IC_{50} values compared to ADPR (IC_{50} = 40 ± 19 µM, 40 ± 4 µM and 50 ± 13 µM).

In conclusion, integrity of both 2′- and 3′-hydroxyl group of adenosine contribute to the interaction of Mac1 with ADPR.

To explore the SAR of the terminal ribose moiety, ADPR analogues harboring methoxy-groups at the C1″ were tested, which were shown in section 5.2.1.2 to be no Mac1 substrates.

Whilst the β-anomer was no Mac1 inhibitor, the α-1″-*O*-methyl-ADPR was able to reduce the enzymatic activity of Mac1, albeit with a ~3-fold higher IC_{50} compared to ADPR (IC_{50} = 79 ± 14 µM), confirming the stereo-selectivity of Mac1 for α-anomeric substrates shown for the NAD anomers.

Next, the role of the individual hydroxyl group of the terminal ribose for Mac1 interaction was determined. Starting with the 1″-position, which is the catalytic target of hydrolase activity and thereby of special interest, we tested ADP-HPD, a known Mac1 ligand (Rack et al., 2020b) as well as 1″,2′-dideoxy-ADPR, both lacking the 1″-OH.

These compounds showed rather low inhibitory potencies in our activity assay. IC_{50} values were 2-fold higher for ADP-HPD versus ADPR (IC_{50} = 64 ± 14 µM) and over 3-fold for 1″,2′-dideoxy-ADPR compared to 1″-OH proficient 2′-deoxy-ADPR (IC_{50} = 148 ± 33 µM).

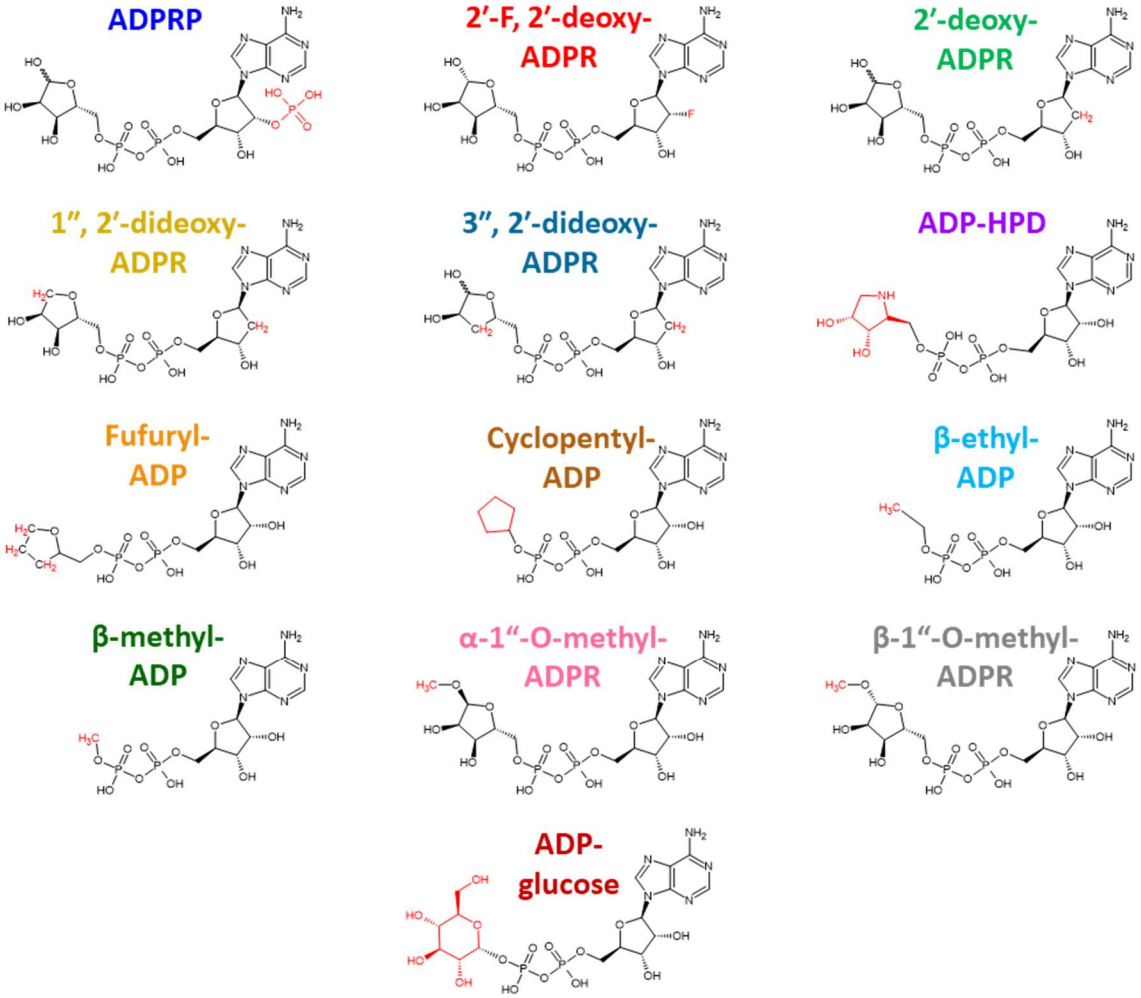

Figure 26: Structures of the ribose-modified ADPR derivatives in this study.

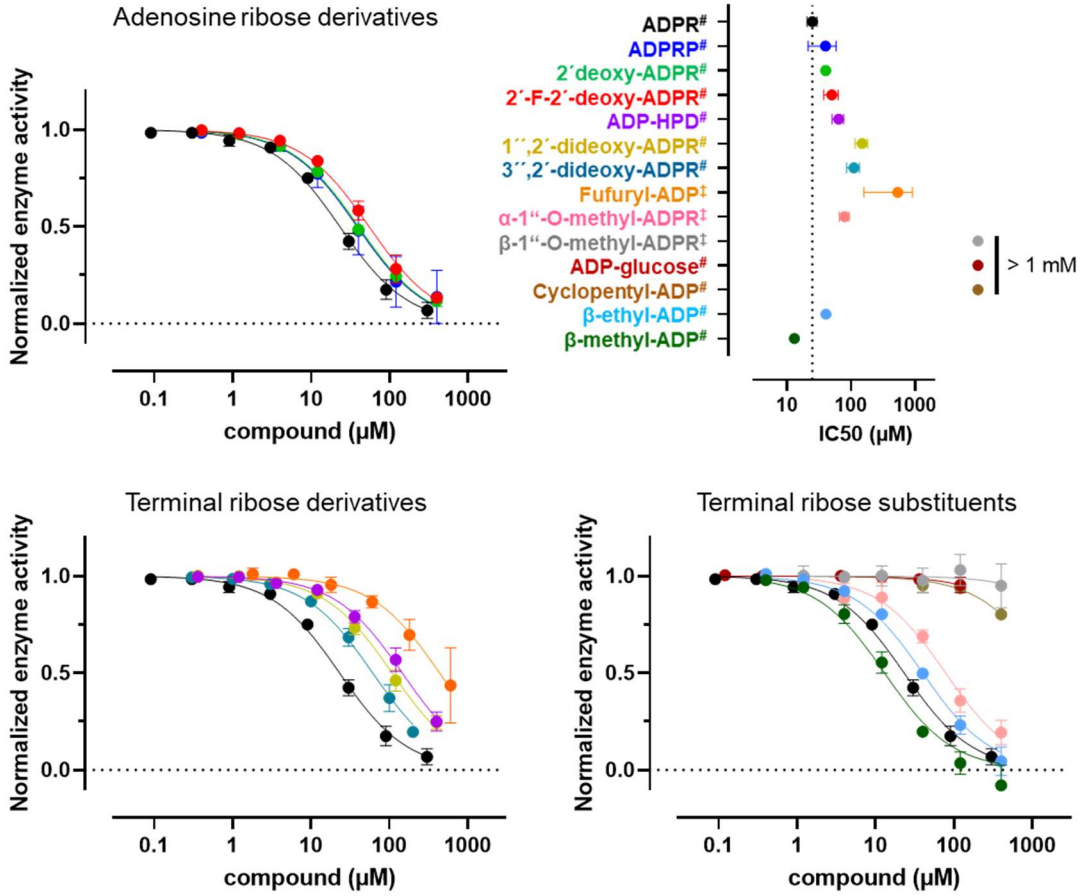

Figure 27: Effect of ribose-modified ADPR derivatives on Mac1 activity. Shown are the chemical structures of the tested compounds (top panel) and the corresponding concentration responses for Mac1 (lower panel) obtained by the previously established microplate (#) or the HPLC-assisted α-NAD assay (‡) respectively. Curves were fitted by a sigmoidal function and the derived IC_{50} values are summarized. For comparison, the previous dataset for ADPR was included. Data are shown as mean ± SD (n ≥ 3).

In addition, 3″,2′-dideoxy-ADPR showed over 2-fold increased IC_{50} compared to the parental 2′-deoxy-ADPR (IC_{50} = 110 ± 25 μM), which demonstrated that both hydroxyl groups at the C3″ and the C1″ are equally important for Mac1 binding.

In contrast, Fufuryl-ADP, an ADPR derivative that has no hydroxyl groups at the terminal tetrahydrofuran ring showed approximately 21-fold lower potency (IC_{50} = 535 ± 376 μM) than ADPR, underlining the necessity of all the hydroxyl-groups for the ligand engagement by Mac1.

Then, the effect of terminal ribose substitutents was investigated. Interestingly, ADP-glucose had no detectable effect on Mac1 activity in the assay

(IC_{50} >> 1 mM), demonstrating that replacement of the terminal ribose for glucose was unfavored.

Furthermore, Mac1 was probed with different ADPR analogues substituting the terminal ribose by different alkyl-residues. Whilst Cyclopentyl-ADP exhibited severely increased IC_{50} (> 1 mM), the opposite trend was observed for smaller alkyl-chains, i.e. ethyl- and methyl-group (IC_{50} = 40 ± 6 µM and IC_{50} = 13 ± 2 µM respectively).

Moreover, the findings of the activity screen for the adenosine ribose-modified ADPR analogues were validated by ITC measurements (Figure 28). The measured Mac1 affinities for 2′-deoxy-ADPR as well as 2′-F-2′-deoxy-ADPR were in good agreement with the concentration responses (K_D = 12.5 ± 0.3 µM and 19.3 ± 5.0 µM respectively) and the K_D value of ADPRP (K_D = 35.2 ± 0.9 µM) was matching IC_{50} value.

Compared to ADPR, binding of these C2′-modified-ADPR derivatives towards Mac1 was highly entropically unfavored, resulting in the somewhat lower affinities.

Next, binding studies for the terminal ribose-modified compounds were conducted (Figure 29). Thermograms of α-1″-*O*-methyl-ADPR revealed reduced net binding enthalpy and subsequently ~5-fold higher K_D values versus ADPR (K_D = 48 ± 10 µM), which was consistent with the less potent inhibition of Mac1.

In addition, binding affinities of β-ethyl-ADP (K_D = 19.9 ± 5.0 µM) and β-methyl-ADP (K_D = 6.7 ± 0.8 µM) were in good agreement with the Mac1 inhibition data, suggesting the latter one as first Mac1 inhibitor candidate.

Since net binding enthalpies for β-methyl-ADP were nearly as high as for ADPR (ΔH = -8.3 ± 0.3 kcal/mol), the increased affinity towards Mac1 was due to reduced entropy (TΔS = -1.3 ± 0.5 kcal/mol). Interestingly, although entropic gain was even higher upon titration of β-ethyl-ADP against Mac1 (TΔS = 1.2 ± 0.3 kcal/mol), binding enthalphies were remarkably low (ΔH = -5.2 ± 0.1 kcal/mol).

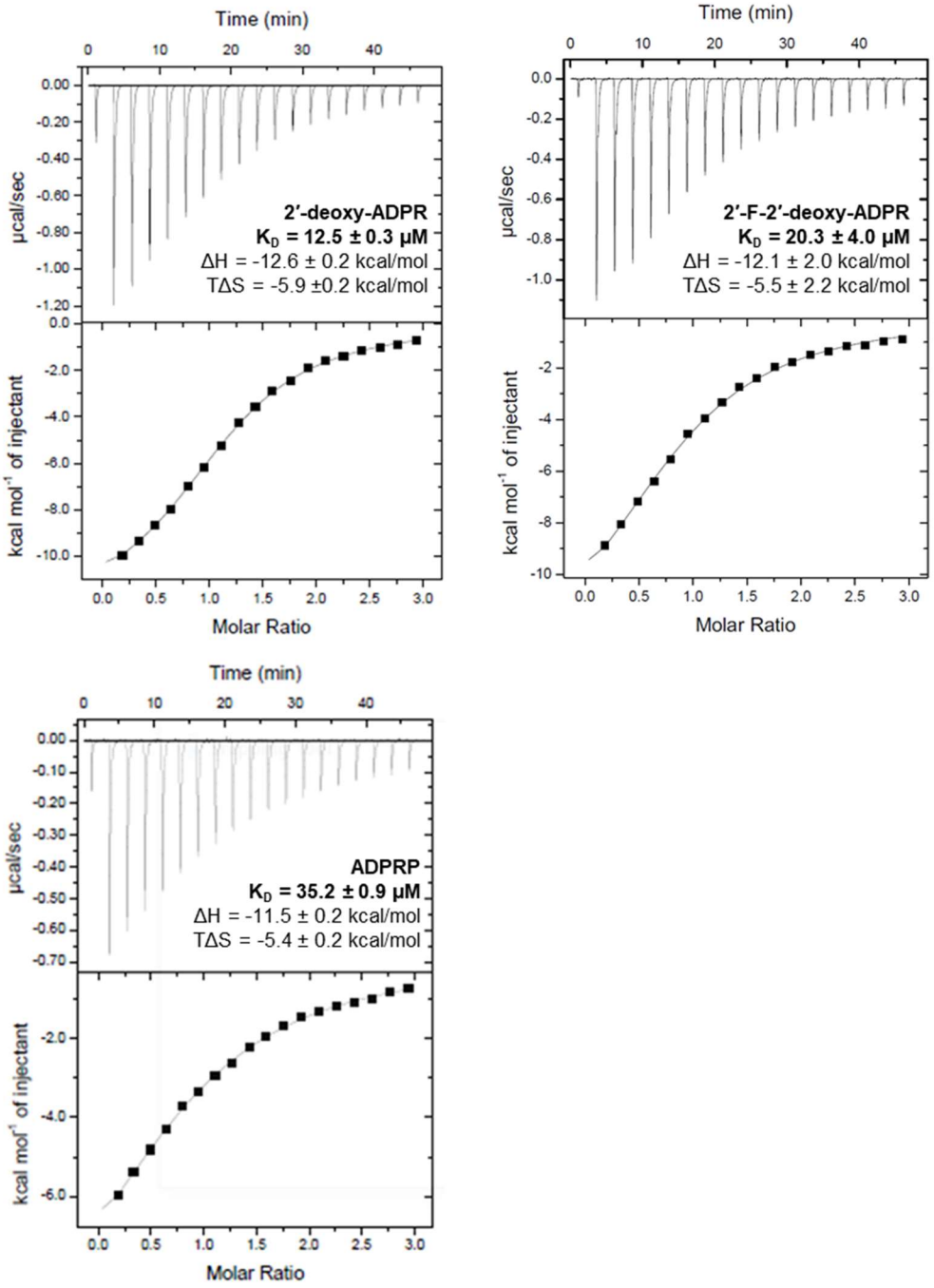

Figure 28: Binding of ADPR analogues modified at the 2′-position to Mac1. Isothermal titration calorimetry (ITC) data are presented. Top graphs show representative baseline corrected thermograms for titration of 0.75 mM of the respective compounds against 50 µM wildtype Mac1. The bottom graphs depict the integrated values of each titration point (squares) fitted to a one-site binding model (solid line). The derived values for K_D, ΔH and TΔS are indictated as mean ± SD (n ≥ 3).

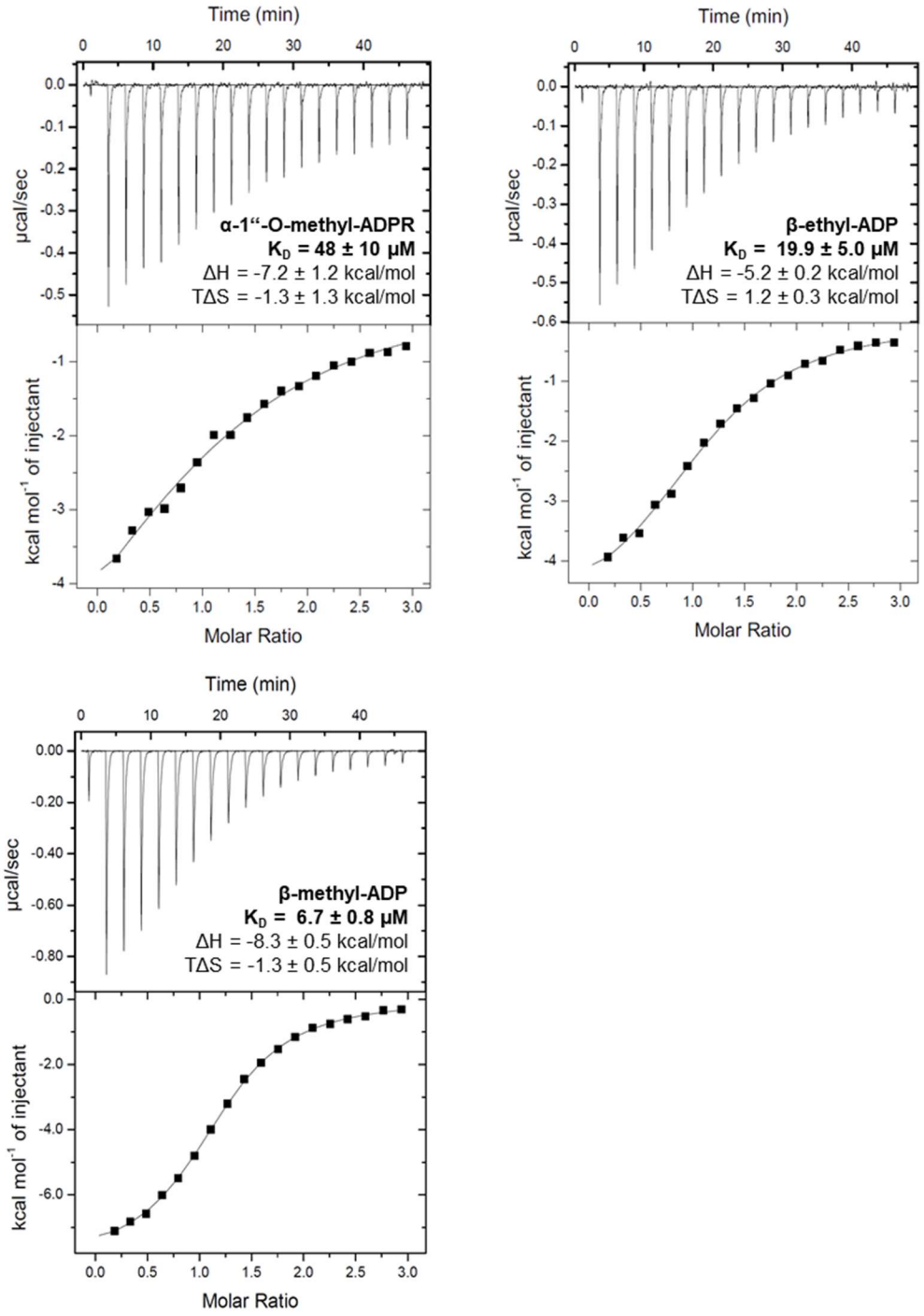

Figure 29: Mac1 binding of ADPR analogues modified at the terminal ribose. Isothermal titration calorimetry (ITC) data are presented. Top graphs show representative baseline corrected thermograms for titration of 0.75 mM of the respective compounds against 50 µM wildtype Mac1. The bottom graphs depict the integrated values of each titration point (squares) fitted to a one-site binding model (solid line). The derived values for K_D, ΔH and TΔS are indictated as mean ± SD (n ≥ 3).

Table 3: Summary of the inhibitory potency and affinity of ribose-modified ADPR analogues towards Mac1.

Compound	IC_{50} (µM)	K_D (µM)
ADPR	24 ± 5	10.2 ± 0.4
ADPRP	40 ± 19	35.2 ± 0.9
2′-deoxy-ADPR	40 ± 4	12.5 ± 0.3
2′-F-2′-deoxy-ADPR	50 ± 13	19.3 ± 5.0
ADP-HPD	64 ± 14	n.d.
1″,2′-dideoxy-ADPR	148 ± 33	n.d.
3″,2′-dideoxy-ADPR	110 ± 25	n.d.
Fufuryl-ADP	535 ± 376	n.d.
α-1″-*O*-methyl-ADPR	79 ± 14	48 ± 10
β-1″-*O*-methyl-ADPR	> 1000	n.d.
ADP-glucose	> 1000	n.d.
Cyclopentyl-ADP	> 1000	n.d.
β-ethyl-ADP	40 ± 6	19.9 ± 5.0
β-methyl-ADP	13 ± 2	6.7 ± 0.8

n.d.: not determined.

5.4.2.3 Pyrophosphate panel

Next, different adenosine diphosphates with modifications at the pyrophospate (Figure 30) were tested against the active site of Mac1. The concentration responses were recorded (Figure 31) and the corresponding IC_{50} values were summarized in Table 4.

With exception of 5′-((2-hydroxybenzoyl)-sulfamoyl)-adenosine (SAL-AMS, IC_{50} = 0.6 ± 0.3 mM), none of compounds harboring the commonly used pyrophosphate bioisosteres, i.e. squarates, acetylphosphonates nor methylenediphosphates showed an inhibitory effect on Mac1 (IC_{50} > 10 mM).

However, in contrast to the β-S-thiophosphonate, thiol substitution at the α-phosphate resulted in >2-fold more potent inhibition of the viral macrodomain

compared to the parental ADP. Thus, IC_{50} values were quite low for both the R- (IC_{50} = 2.6 ± 0.4 mM) and the S-isomer (IC_{50} = 1.8 ± 0.4 mM).

In conclusion, these data argue for a highly conserved Mac1 interaction network around the pyrophosphate with only little room for ligand modification, such as substitution of phosphate hydroxyl groups for thiols, which subsequently lowers the pK_a and contributes to Mac1 inhibition.

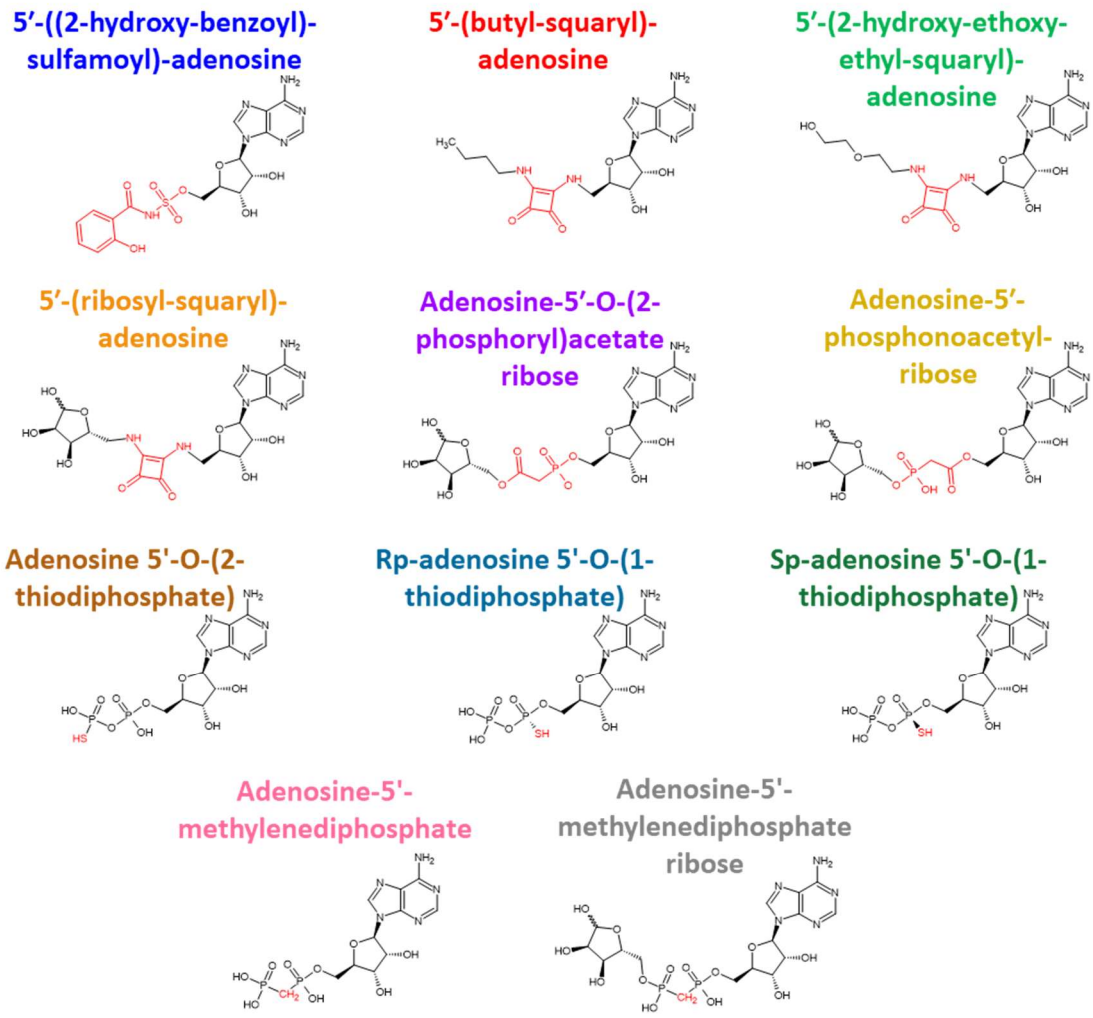

Figure 30: Structures of pyrophosphate-modified ADP and ADPR derivatives in this study.

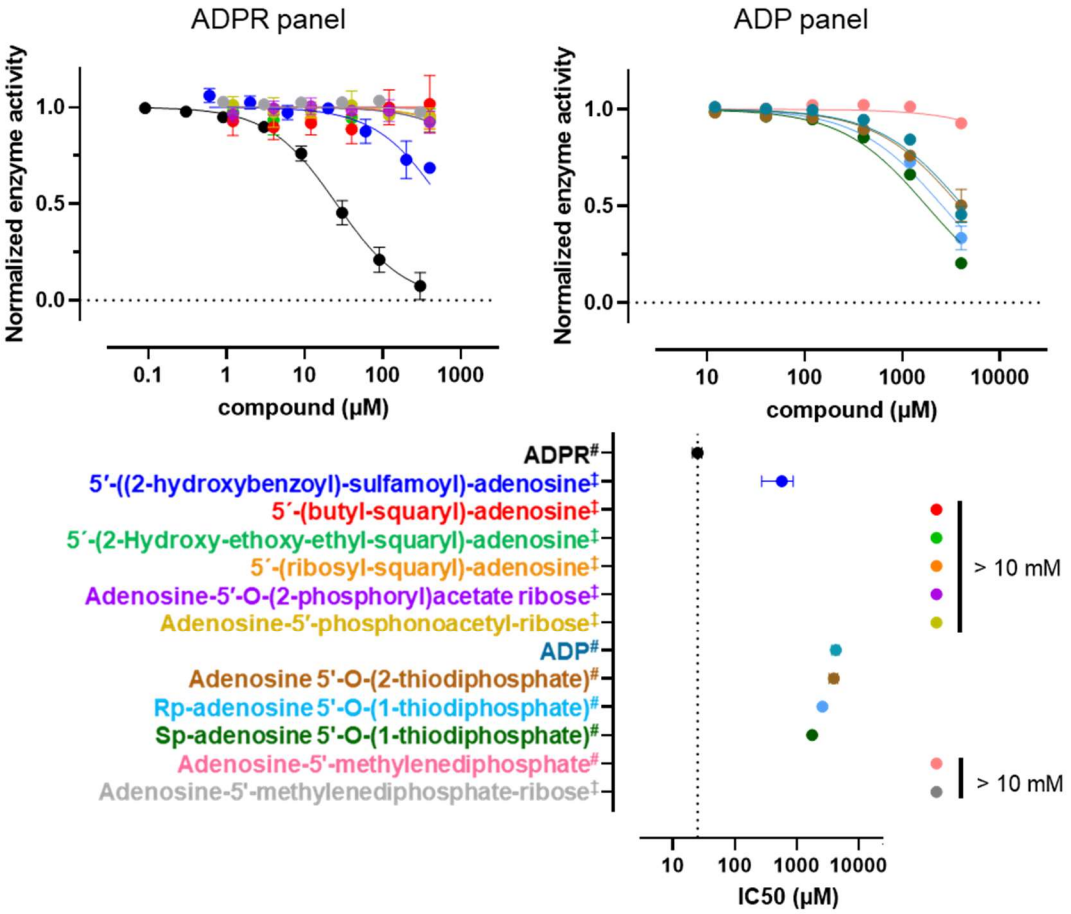

Figure 31: Effect of pyrophosphate-modified ADP and ADPR derivatives on Mac1 activity.
Shown are the concentration responses for Mac1 from the ADPR panel (top left) and the ADP panel (top right) obtained by the previously established microplate (#) or the HPLC-assisted α-NAD assay (‡) respectively. Curves were fitted by a sigmoidal function and the derived IC_{50} values are summarized (bottom). For comparison, the previous datasets for ADPR and ADP were included. Data are shown as mean ± SD (n ≥ 3).

Table 4: Summary of the inhibitory potency of ADP derivatives and ADPR analogues with modifications at the pyrophosphate towards Mac1.

Compound	IC_{50} (mM)
ADPR	24 ± 5
5′-((2-hydroxybenzoyl)-sulfamoyl)-adenosine	0.6 ± 0.3
5′-(butyl-squaryl)-adenosine	> 10
5′-(2-hydroxy-ethoxy-ethyl-squaryl)-adenosine	> 10
5′-(ribosyl-squaryl)-adenosine	> 10
Adenosine-5′-O-(2-phosphoryl)acetate ribose	> 10
Adenosine-5′-phosphonoacetyl-ribose	> 10
ADP	4.3 ± 0.2
Adenosine 5'-O-(2-thiodiphosphate)	4.0 ± 0.6
Rp-adenosine 5'-O-(1-thiodiphosphate)	2.6 ± 0.4
Sp-adenosine 5'-O-(1-thiodiphosphate)	1.8 ± 0.1
Adenosine-5'-methylenediphosphate	> 10
Adenosine-5'-methylenediphosphate-ribose	> 10

5.5 Rational drug design

This chapter describes the generation a novel Mac1 inhibitor based on the previous SAR data followed by biophysical characterization and biochemical validation *in vitro*. In addition, initial pharmacological data of a cell membrane-permeable derivativative will be presented.

5.5.1 SAR-guided development of β-methyl-GS-441524-5′-diphosphate as novel Mac1 inhibitor

In order to generate small molecule inhibitors, different minimal structures of ADPR were probed against Mac1 and molecule complexity was consequently reduced to the nucleoside level (Figure 32). Data were summarized in Table 5. Despite cAMP, which was as potent as ADP (IC_{50} = 4.6 ± 0.6 mM), adenosine and AMP had barely any influence on Mac1 activity (IC_{50} > 5 mM).

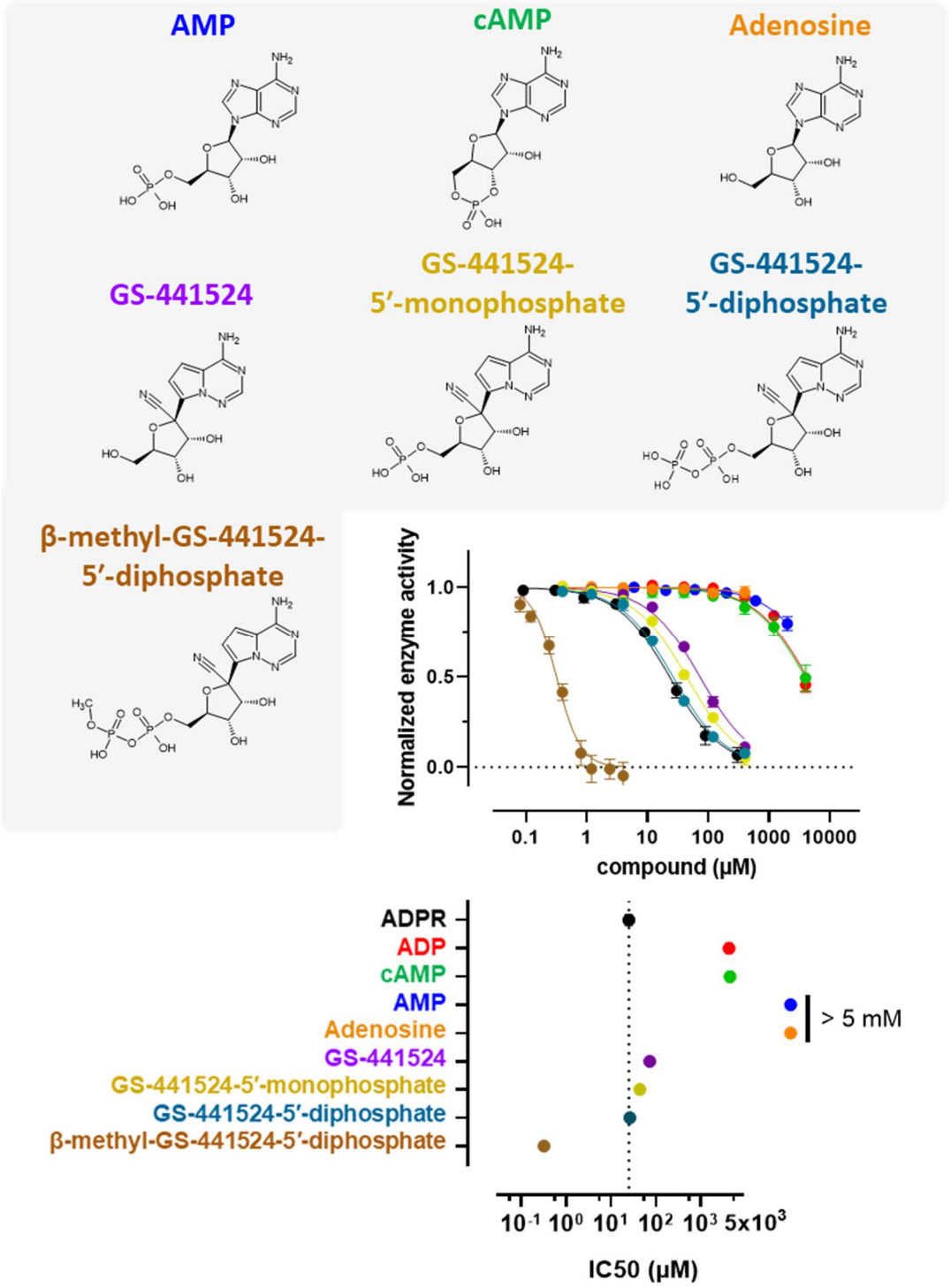

Figure 32: Bioactivity of rationally designed Mac1 inhibitors.
Shown are the chemical structures of the tested compounds (top panel) and the corresponding concentration responses for Mac1 (mid right), obtained by the established microplate assay protocol, whilst β-methyl-GS-441524-5′-diphosphate was incubated for 8 h with 0.6 μM enzyme. Curves were fitted by a sigmoidal function and the derived IC_{50} values are summarized (bottom right). For comparison, the previous datasets for ADPR and ADP were included. Data are shown as mean ± SD (n ≥ 3).

Remarkably, the remdesivir metabolite GS-441524, which was recently reported as potential Mac1 ligand (Ni et al., 2021), was comparable to ADPR in the microplate assay (IC_{50} = 73 ± 3 µM).

Capitalizing on the previous SAR data, the key chemical features of both, the initial inhibitor candidate β-methyl-ADP and GS-441524 were combined in order to improve IC_{50} values.

Thus, a GS-441524-5´-diphosphate with a methyl-group at the β–phosphate was predicted to be a potent Mac1 inhibitor. Interestingly, testing of β-methyl-GS-441524-5´-diphosphate precursors showed significant inhibitor improvement during nucleoside phosphorylation (IC_{50} = 44 ± 3 µM for GS-441524-5´-monophosphate and 26 ± 2 µM for GS-441524-5´-diphosphate).

Strikingly, initial testing of β-methyl-GS-441524-5´-diphosphate in the Mac1 microplate assay hit the stoichiometric limitation of the plate assay of ~1.4 µM, which was still the case after reduction of the Mac1 concentration by 75%, demonstrating > 40-fold higher inhibitory potency than β-methyl-ADP and > 75-fold higher than ADPR (IC_{50} = 0.32 ± 0.05 µM).

Consistent with the activity data, ITC measurements for β-methyl-GS-441524-5´-diphosphate showed high Mac1 affinity in the nanomolar range (K_D = 0.17 ± 0.01 µM), whereas GS-441524-5´-diphosphate was a significantly less affine ligand (K_D = 10.9 ± 1.2 µM) (Figure 33).

These data argue for an enthalpy-driven benefit upon esterification of the β-phosphate GS-441524-5′-diphosphate leading to improved Mac1 inhibition as analogously seen for ADP.

In line with that, net binding enthalpies towards the viral macrodomain were nearly identical for β-methyl-ADP and β-methyl-GS-441524-5′-diphosphate but only the latter one was entropically favored.

In conclusion, β-methyl-GS-441524-5´-diphosphate appears to be a promising lead-like structure for a competitive inhibitor against enzymatic activity of Mac1.

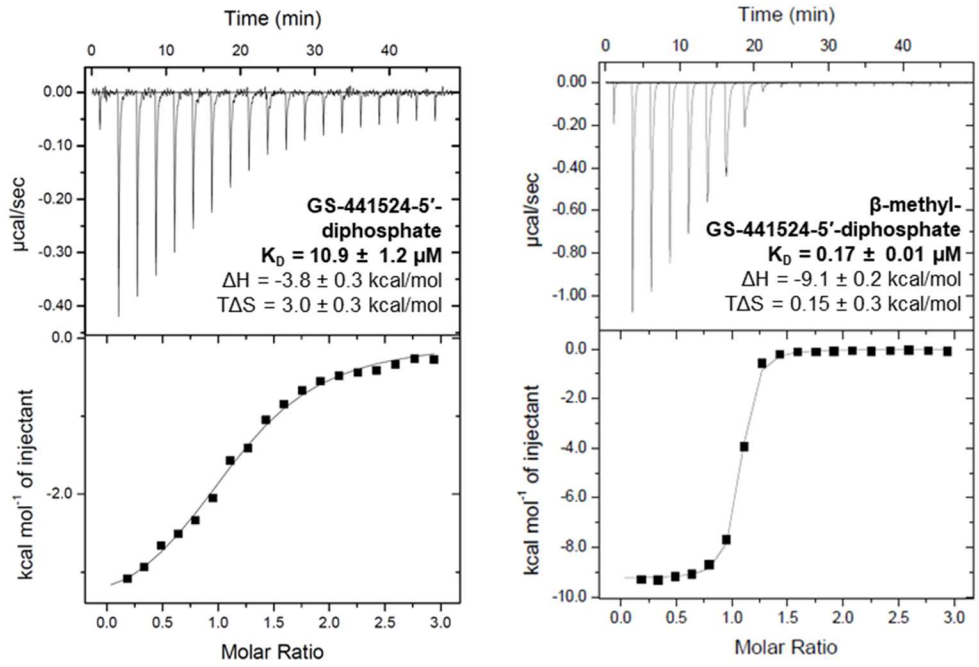

Figure 33: Binding of GS-441524-5′-diphosphate and β-methyl-GS-441524-5′-diphosphate to Mac1.
Isothermal titration calorimetry (ITC) data are presented. Top graphs show representative baseline corrected thermograms for titration of 0.75 mM of the respective compounds against 50 µM wildtype Mac1. The bottom graphs depict the integrated values of each titration point (squares) fitted to a one-site binding model (solid line). The derived values for K_D, ΔH and TΔS are indictated as mean ± SD (n ≥ 3).

Table 5: Summary of the inhibitory potency and affinity of minimal ADPR structures and GS-441524 derivatives towards Mac1.

Compound	IC_{50} (µM)	K_D (µM)
ADPR	24 ± 5	10.2 ± 0.4
ADP	4.3 ± 0.2	n.d.
cAMP	4.6 ± 0.6	n.d.
AMP	> 10	n.d.
Adenosine	> 10	n.d.
GS-441524	73 ± 3	n.d.
GS-441524-5′-monophosphate	44 ± 3	n.d.
GS-441524-5′-diphosphate	26 ± 2	10.9 ± 1.2
β-methyl-GS-441524-5′-diphosphate	0.32 ± 0.05[a] 1.3 ± 0.1[b]	0.17 ± 0.01

n.d.: not determined. (a) Microplate assay. (b) de-MARylation assay.

5.5.2 Validation and off-target assessment for β-alkylated adenosine- and GS-441524-5′-diphosphates

In order to assess off-target potential of the β-alkylated nucleotides in this study, countertests on human macrodomains were conducted (Figure 34) and the data were summarized in Table 6. Here, β-methyl-ADP showed weak potency against MacroD1 (IC_{50} = 0.53 ± 0.07 mM) and MacroD2 (IC_{50} > 0.8 mM) respectively. Interestingly, concentration responses for β-ethyl-ADP were not significantly different to β-methyl-ADP, although there might be a slight trend towards weaker inhibition for MacroD1 (IC_{50} = 0.9 ± 0.2 mM) and MacroD2 (IC_{50} > 0.8 mM), hinting to the same reciprocal relation between inhibitory potency and alkyl chain length, which was previously observed for Mac1.

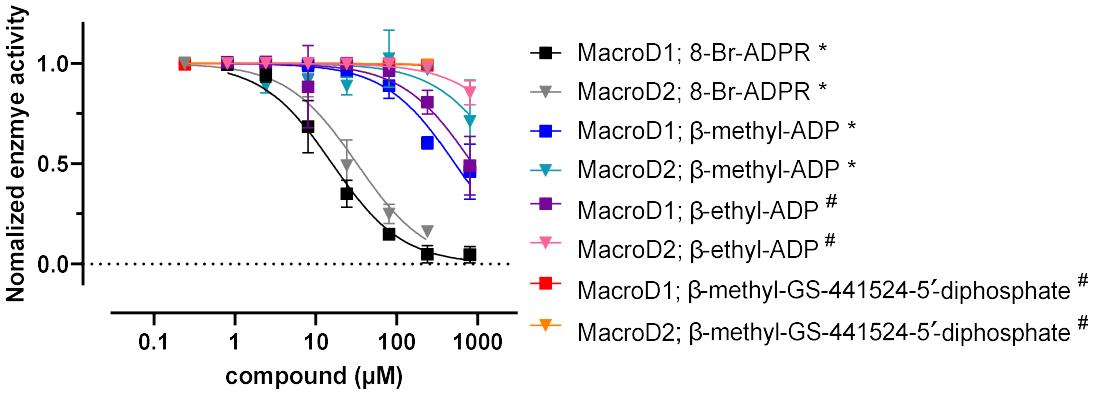

Figure 34: β-methyl-GS-441524-5′-diphosphate does not inhibit human MacroD1 and MacroD2.
Shown are concentration responses obtained by the HPLC-assisted α-NAD (*) or microplate assay (#) using 1 µM MacroD1 or 3 µM MacroD2 respectively. For better comparison, the previous datasets of 8-Br-ADPR for the human macrodomains were included. Curves were fitted by a sigmoidal function. Data are presented as mean ± SD (n ≥ 3).

Importantly, β-methyl-GS-441524-5′-diphosphate had no significant effect on both human macrodomains in the α-NAD assay (IC_{50} > 0.3 mM) as well as in the de-MARylation assays (IC_{50} > 0.1 mM, Figure 35), whilst impairing the de-ADP-ribosylating activity of Mac1 in the low micromolar range (IC_{50} = 1.3 ± 0.1 µM), suggesting at least 100-fold higher selectivity for Mac1.

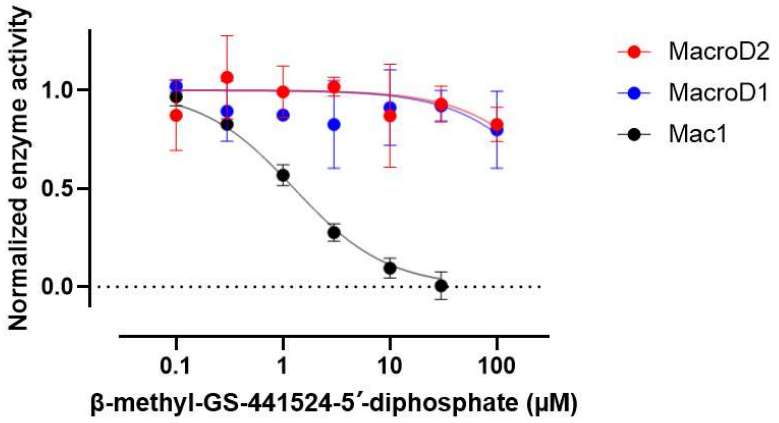

Figure 35: β-methyl-GS-441524-5′-diphosphate inhibits the de-ADP-ribosylating activity of Mac1 but not of human MacroD1 and MacroD2. Shown are concentration responses for β-methyl-GS-441524-5′-diphosphate in the PARP10 de-MARylation assay using either 0.3 μM Mac1, 1 μM MacroD1, or 3 μM MacroD2 respectively. Curves were fitted by a sigmoidal function. Data are shown as mean ± SD (n ≥ 2).

Table 6: Summary of the inhibitory potency of Mac1 inhibitors towards human macrodomains.

Compound	IC_{50} (mM)	
	MacroD1	MacroD2
8-Br-ADPR	0.016 ± 0.002[a] 0.09 ± 0.02[b]	0.033 ± 0.004[a] 0.043 ± 0.005[b]
β-methyl-ADP	0.53 ± 0.07[a]	> 0.8[a]
β-ethyl-ADP	0.9 ± 0.2[c]	> 0.8[c]
β-methyl-GS-441524-5′-diphosphate	> 0.3[c] > 0.1[b]	> 0.3[c] > 0.1[b]

Determined by (a) HPLC-assisted α-NAD assay, (b) De-MARylation assay, (c) Microplate assay.

5.5.3 Treatment of CaLu-3 cells with a C_{11}-acyloxybenzyl (AB)-masked prodrug of β-methyl-GS-441524-5′-diphosphate

In order to directly target Mac1, inhibitors need to be available intracellulary. However, the therapeutic usage of nucleotides is usually limited due to their high negative charge, leading to low membrane permeability. Therefore, strategies were developed for administration of these compounds as prodrugs by

introduction of bio-reversible groups, which not only can mask the charge of the nucleotide and increase lipophilicity, but also help entrapment of the active compound inside the cell due to final deprotection by esterases and subsequent reduction of lipophilicity (Meier, 2017).

Using the prodrug approach, β-methyl-GS-441524-5′-diphosphate was masked with an additional C_{11}-acyloxybenzyl (AB) group at the β-phosphate and uptake by CaLu-3 cells was measured (Figure 36A + B).

As expected, accumulation of β-methyl-GS-441524-5′-diphosphate in the lysates was significantly more efficient when CaLu-3 cells were incubated with the prodrug compared to treatment of the cells with the unprotected β-methyl-GS-441524-5′-diphosphate.

For the latter, cellular uptake reached an equilibrium already after 15 min, whereas for the prodrug group β-methyl-GS-441524-5′-diphosphate levels rapidly increased and did not plateau even after 60 min of incubation.

The final intracellular concentration of β-methyl-GS-441524-5′-diphosphate was at least 5-fold higher when CaLu-3 cells were treated with the prodrug instead of the unmasked compound, reaching up to ~0.16 mM after one hour (Figure 36B + C), which was approximated using published data of cytoplasmic volume of CaLu-3 cells (Min et al., 2017).

Furthermore, metabolization of the compound in the presence of CaLu-3 cells only occurred with the prodrug (Figure 36C). GS-441524-5′-monophosphate levels were 24 ± 14% of the β-methyl-GS-441524-5′-diphosphate peaks after one hour of incubation with 50 µM compound, indicating a reduced stability of the pyrophosphate due to the masking group.

Interestingly, upon treatment with high prodrug concentrations (>5 µM) for 60 min, β-NAD levels in the Calu-3 cells decreased by 42 ± 25%, which was less pronounced for the unmasked compound (~14 ± 11%) hinting towards cellular stress evoked by the masking group.

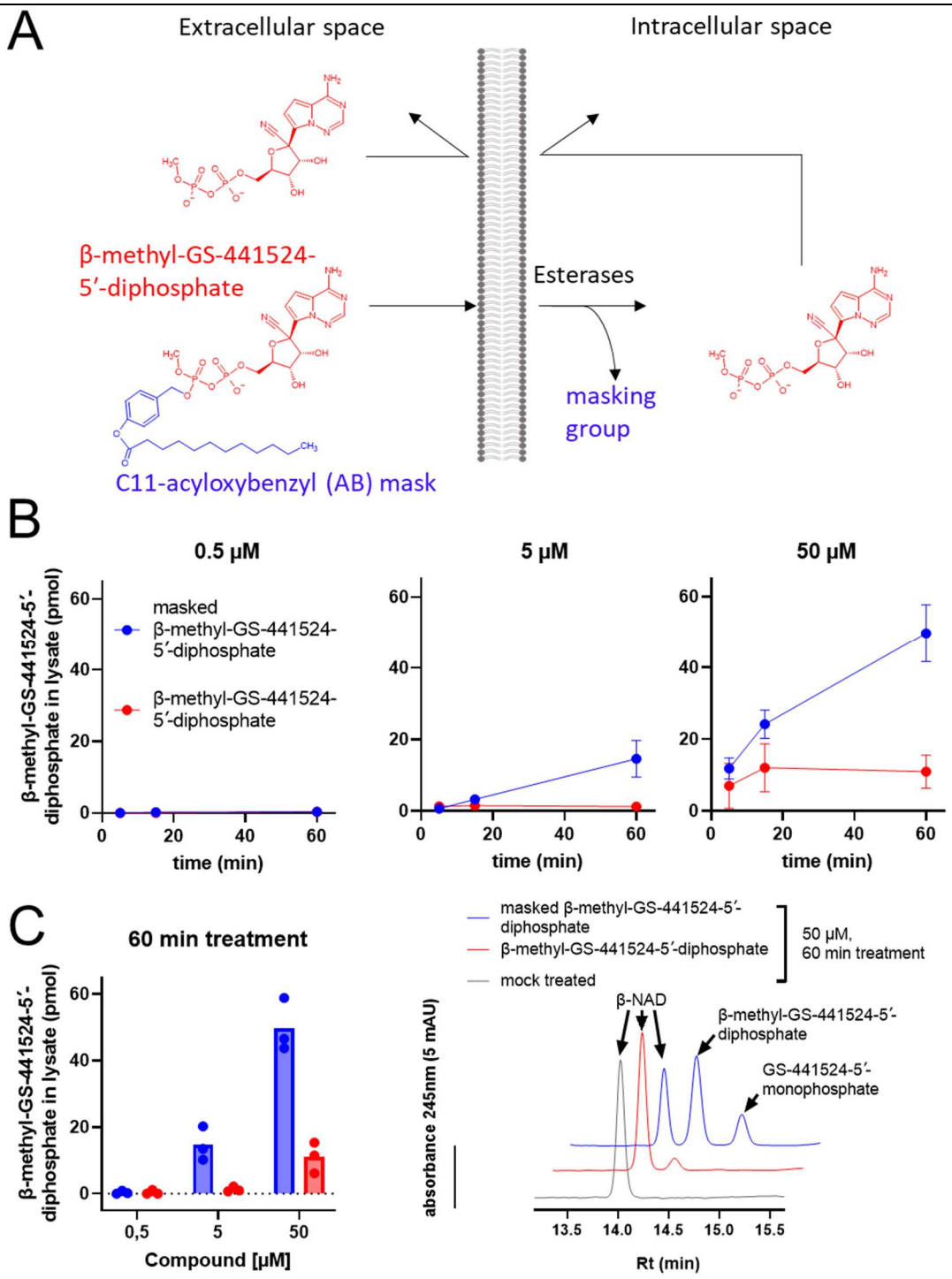

Figure 36: Masking of β-methyl-GS-441524-5′-diphosphate increases uptake by CaLu-3 cells but decreases stability.
A) Outline of the prodrug strategy for β-methyl-GS-441524-5′-diphosphate. **B**) CaLu-3 cells were treated with either β-methyl-GS-441524-5′-diphosphate (red) or the C_{11}-AB-masked prodrug (blue) at the indicated concentrations. At the indicated timepoints, cells were washed and lysated prior to HPLC analysis. Shown are time-courses for the β-methyl-GS-441524-5′-diphosphate amount in the lysates as well as an **C**) overview for the different conditions after 60 min of treatment (left) and representatitive HPLC-chromatograms (right) for the incubation with 50 µM compound.

5.5.4 Biostability of β-methyl-GS-441524-5′-diphosphate derivatives

To estimate compound stability, metabolization of β-methyl-GS-441524-5′-diphosphate and its prodrug were assessed *in vitro* as well as in CaLu-3 cell assays. HPLC analysis showed that nucleotide monophosphates were the main metabolite of the tested compounds across the different conditions (Figure 37). However, β-methyl-GS-441524-5′-diphosphate appeared to be rather stable both on cells (3.0 ± 0.3 % GS-441524-5′-monophosphate after 60 min) and after exposure to cell lysates (~13% metabolization after 20 h). Of note, enzymatic activity of the lysate was confirmed by 1,N^6-etheno-ADPR hydrolysis (~25% 1,N^6-etheno-AMP formation after 20 h).

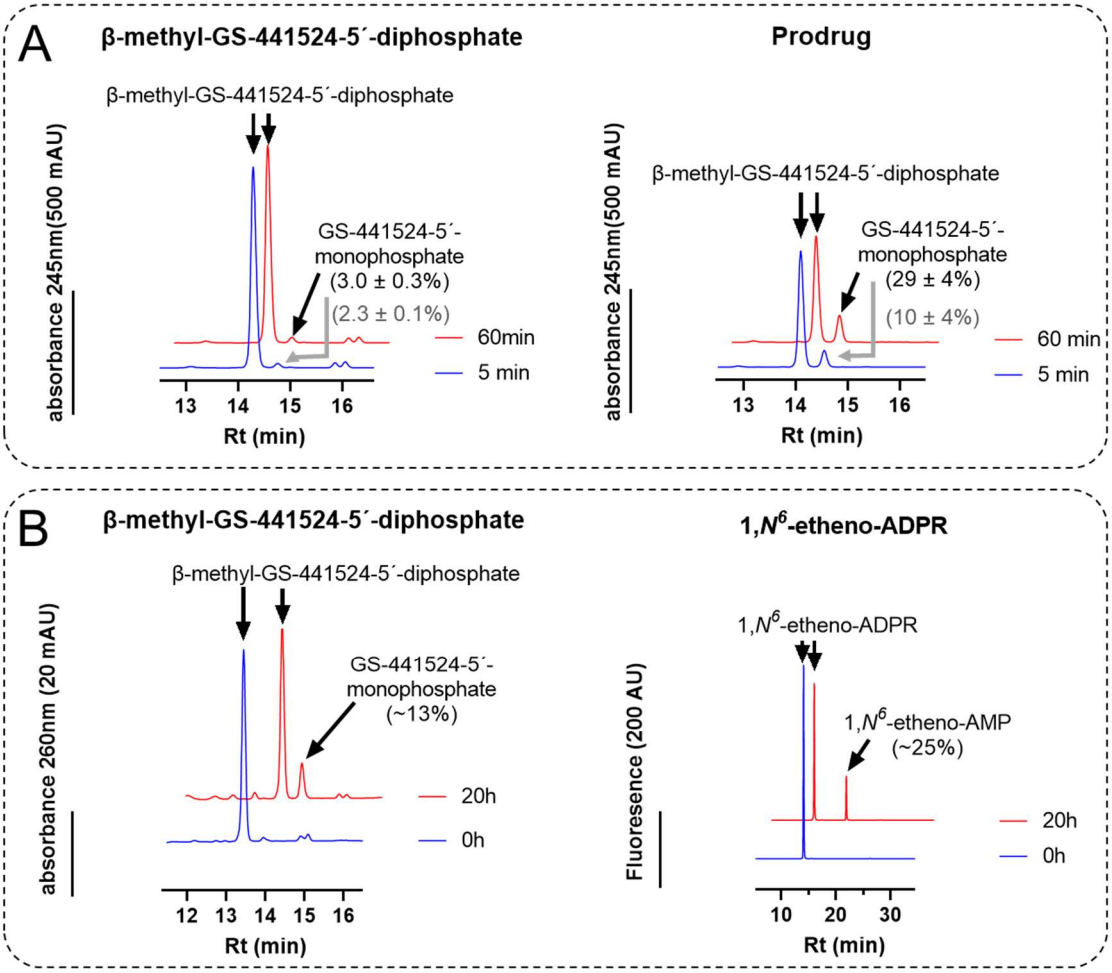

Figure 37: Masked β-methyl-GS-441524-5′-diphosphate is less stable than the unprotected compound in biological media.
Shown are HPLC chromatograms of the **A**) supernatants of CaLu-3 cells after extracellular treatment with 50 µM of either β-methyl-GS-441524-5´-diphosphate or the prodrug derivative for the indicated timepoints as well as reaction products of **B**) β-methyl-GS-441524-5´-diphosphate or the 1,N^6-etheno-ADPR control after incubation with crude CaLu-3 cells extracts for the indicated timepoints.

In contrast to the unmasked compound, the prodrug was rapidly metabolized in the first 5 min on CaLu-3 cells (70 ± 12 % deprotected) and exhibited higher formation of GS-441524-5′-monophosphate (10 ± 4%), which increased ~3-fold after 1 h (29 ± 4%). This is consistent with the metabolization data of the previous uptake studies and further confirmed the low pyrophosphate stability resulting from the masking of β-methyl-GS-441524-5′-diphosphate.

5.5.5 Toxicity of the β-methyl-GS-441524-5′-diphosphate prodrug on CaLu-3 cells

Finally, a MTS-assay was conducted with CaLu-3 cells upon prodrug treatment (Figure 38). As control, the parental nucleoside GS-441524 was selected, which is known to be permeable for CaLu-3 cells (Tao et al., 2021). Interestingly, the prodrug started to exhibit cytotoxic effects in the micromolar range (CC_{50} = 0.03 ± 0.01 mM), resulting in a selectivity index (SI) of ~30 ($CC_{50,prodrug}$/ $IC_{50,β\text{-}methyl\text{-}GS\text{-}441524\text{-}5′\text{-}diphosphate}$).

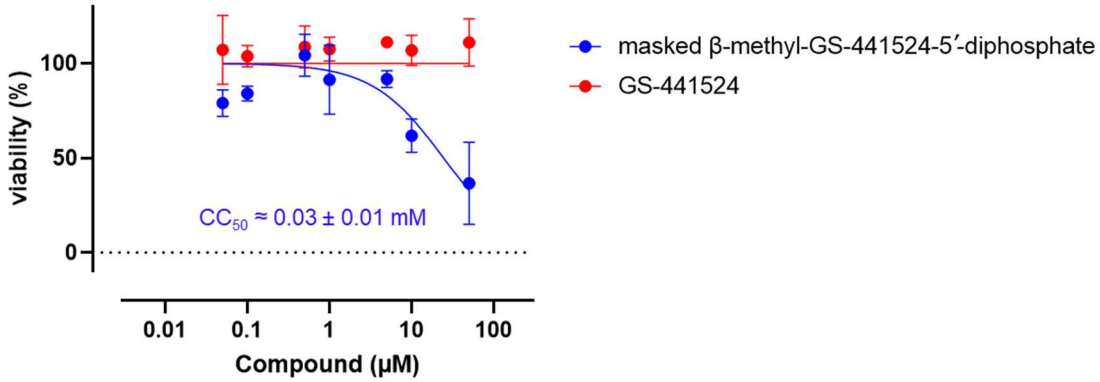

Figure 38: The prodrug of β-methyl-GS-441524-5′-diphosphate is more cytotoxic for CaLu-3 cells than the parental nucleoside.
MTS assay data for CaLu-3 cells treated with either masked β-methyl-GS-441524-5′-diphosphate or the GS-441524 control for 1 hour at the indicated concentrations. Concentration response curves were fitted by a sigmoidal function. Data are shown as mean ± SD of three technical replicates.

6 Discussion

Macrodomains represent novel targets for antiviral drugs targets as their de-ADP-ribosylating function determines viral titer in SARS-CoV-1 and MHV infections *in vivo* (Fehr et al., 2016; Voth et al., 2021), which was also later demonstrated for replication of SARS-CoV-2, both *in vitro* and *in vivo* (Alhammad et al., 2023; Taha et al., 2023).

However, targeting the active site of macrodomains, which are structurally well conserved among coronaviruses, represents a challenging task, but also offers the opportunity to generate broad-spectrum antivirals with a novel mode of action (Rack et al., 2020b).

6.1.1 Power of HTS and virtually pre-screened small molecule drug libraries for Mac1 screening

High-throughput screening (HTS) of compounds often appears to be a straightforward way for discovery of small molecule inhibitors or drug repurposing. But so far, using conventional approaches, no HTS study yielded very promising inhibitors for the viral macrodomain with sub-micromolar potency (Virdi et al., 2020; Sowa et al., 2021; Dasovich et al., 2022; Roy et al., 2022). Only the use of enormous resource- and labor-intensive screening procedures of large compound libraries (Schuller et al., 2021) and the subsequent extensive bioinformatical effort and involvement of commercial partners finally yielded a few compounds with sub-micromolar affinity (best candidate K_D = 0.4 µM) towards Mac1 (Gahbauer et al., 2023).

On the one hand, these findings demonstrate the rather low hit rate of the *in silico* pre-selection approach for early drug discovery, which is likely due to the inaptness of the computational models to accurately and simultaneously account for the molecular requirements of the Mac1-ADPR interaction. Thus, involvement of the water molecule networks (Correy et al., 2022), the pronounced induced fit (Frick et al., 2020; Michalska et al., 2020; Alhammad et al., 2021; Zhao et al., 2021) and physicochemical dependencies, e.g. pH and temperature (Correy et al., 2022) need to be taken into account.

On the other hand, utilization of small molecule libraries limit early drug discovery and SAR development to small sections of the macrodomain. However, the

successful targeting of the accessible sub-pocket of the adenine in a previous screening study (Schuller et al., 2021) emphasized the choice of an assorted purine-targeted library for generating of a SAR. Thus, probing of Mac1 with ADPR analogues allowed to embrace the entire binding site and finally proved to be a quite successful as well as resource- and time-efficient approach for design of potent and selective Mac1 inhibitors.

6.1.2 Physicochemical and structural properties of ADPR determining ligand engagement of Mac1

To aid the SAR development, structural information of Mac1-ligand complexes from available structures in the protein data bank (PDB) as well as from X-ray diffraction crystallography data, which were obtained in collaboration with the labs of Henning Tidow and Maria Garcia Alai at the Deutsches Elektronen-Synchrontron (DESY) campus, have been included for interpretation of the bioactivity data.

6.1.2.1 SAR of the adenine base of ADPR

Thus, as many adenine nucleotide binding proteins, Mac1 engages ADPR in a well conserved pattern by forming hydrogen bonds between D22 and the adenine´s N6 as well as between the backbone-NH of isoleucine at position 23 (I23) and the N1 (Denessiouk & Johnson, 2003; Karras et al., 2005) (Figure 39). Consistently, IDPR and 1,N^6- etheno-ADPR, which either chemically or sterically lack the ability for engagement in hydrogen bonding with the D22 and I23 respectively, are no Mac1 inhibitors. This is also in line with a previous report showing that etheno-modified ADP-ribosylated proteins are no substrates for Mac1 (Rack et al., 2020).

In addition, Mac1 inhibition was influenced by either fluorination of the C2 or substitution of the N7 for carbon (7-deaza), which, although being chemically distinct modifications, both influence the acidic strength of the N1, which normally has a pK_a of 3.5. Whilst the N1 of 2-F-adenosine exhibits lower acidic strength ($pK_a < 1$), which weakens H-bond acceptance for NH of the peptide backbone of I23, adenosine derivatives with a 7-deaza modification harbor a more basic N1 (pK_a ~5.2) (Sydam & Strobel, 2008), thereby fostering hydrogen bond acceptor capatibilities, resulting in more potent Mac1 inhibitors.

This is even more favored due to the fact that a 7-deaza modification of adenine bases reduces polarity, thereby improving compatibility with the overall hydrophobic adenosine binding site of Mac1.

In conclusion, these data highlighted the importance of hydrogen bond formation of the adenine base via the N1 and N6 with Mac1 for ligand binding.

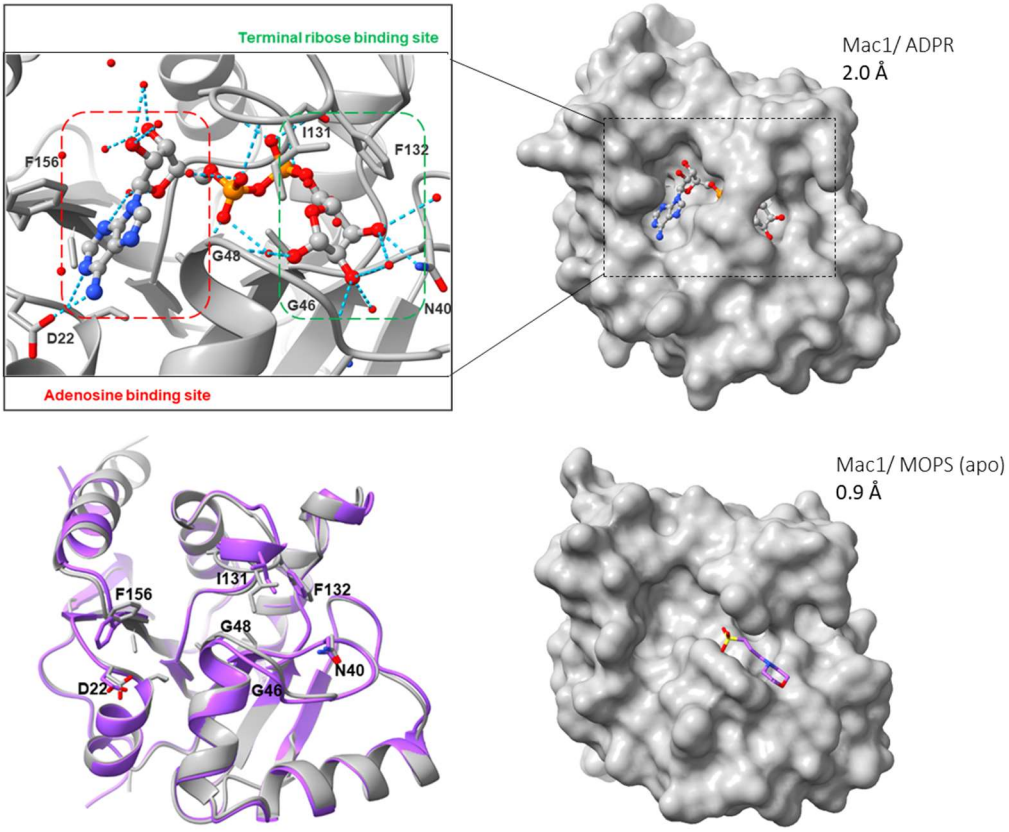

Figure 39: X-ray crystal structure of Mac1 apo and the Mac1-ADPR complex. The top panel shows the ADPR-bound structure (PDB: 8AZD) as well as a zoom-in of the predicted hydrogen bond interactions (blue meshed lines) of Mac1 and ADPR. The lower panel shows (bottom right) the MOPS-bound (apo, PDB: 8AZC) structure and (bottom left) a superimposition of the closed (ADPR) and open (apo) state of Mac1.

Modification of the C8 of the adenine base generally resulted in less potent inhibition of Mac1. Although binding modes of the 8-brominated ADPR derivatives were identical to ADPR (Figure 40), less affine binding occurred, which likely resulted from two circumstances: a) sterical clashes between the bromine and the protein backbone as adduct bulkiness was negatively correlated with Mac1 inhibition. b) spatial constrainment and formation of H-bonds require

the adenosine to bind in the *anti*-conformation, but the additional bromine favores the *syn*-state, which has been already reported for apolar C8-substituents (Figure 41) (Westhof et al., 1975; Harder et al., 2015). However, both, 8-amino-ADP and 8-amino-ADPR were poor Mac1 inhibitors, although 8-amino-adenosine has been shown to adopt the *anti*-conformation (Harder et al., 2015).

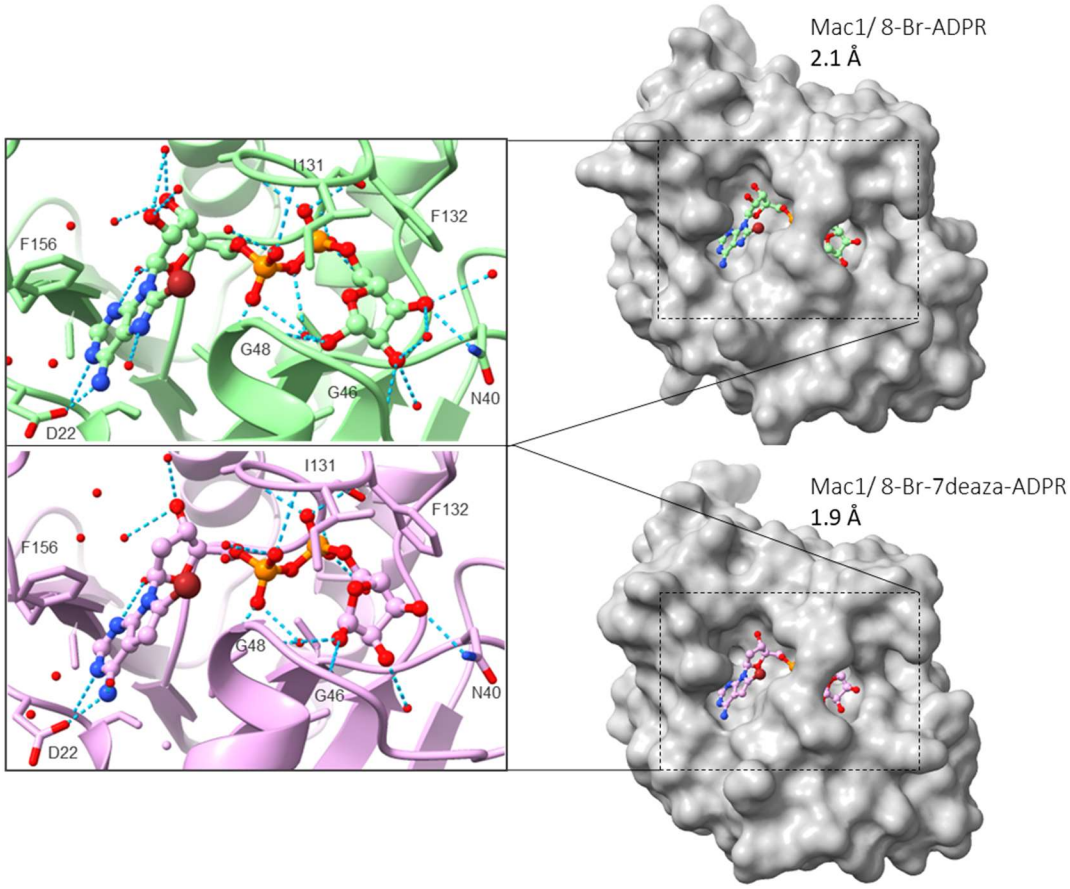

Figure 40: Co-crystal structures of Mac1 in complex with 8-Br-ADPR and 8-Br-7-deaza-ADPR.
The right panel shows the ligand-bound structures of Mac1 with either 8-Br-ADPR (top, PDB: 8AZM) or 8-Br-7-deaza-ADPR (bottom, unpublished). The left panel depicts the zoom-ins of the predicted hydrogen bond interactions (blue meshed lines) between the protein and the respective ligands.

Although there seems to be no obvious sterical impairment inside the binding pocket, amination of the C8 disfavores ligand engagement likely due to a) increased polarity, which elevates local incompatibilities with the apolar adenosine binding site (G46-G48 loop). b) disruption of intra-molecular hydrogen

bonds between the 8-amino-group and the 5′-OH (Harder et al., 2015), likely due to a disadvantageous H-bond engagement angle that is expected upon Mac1 binding for a modelled complex with 8-amino-ADPR assuming a binding mode similar to the parental structure (Figure 41). Taken together, spatial, electrostatic and conformational attributes of the nucleobase of ADPR favor binding towards Mac1.

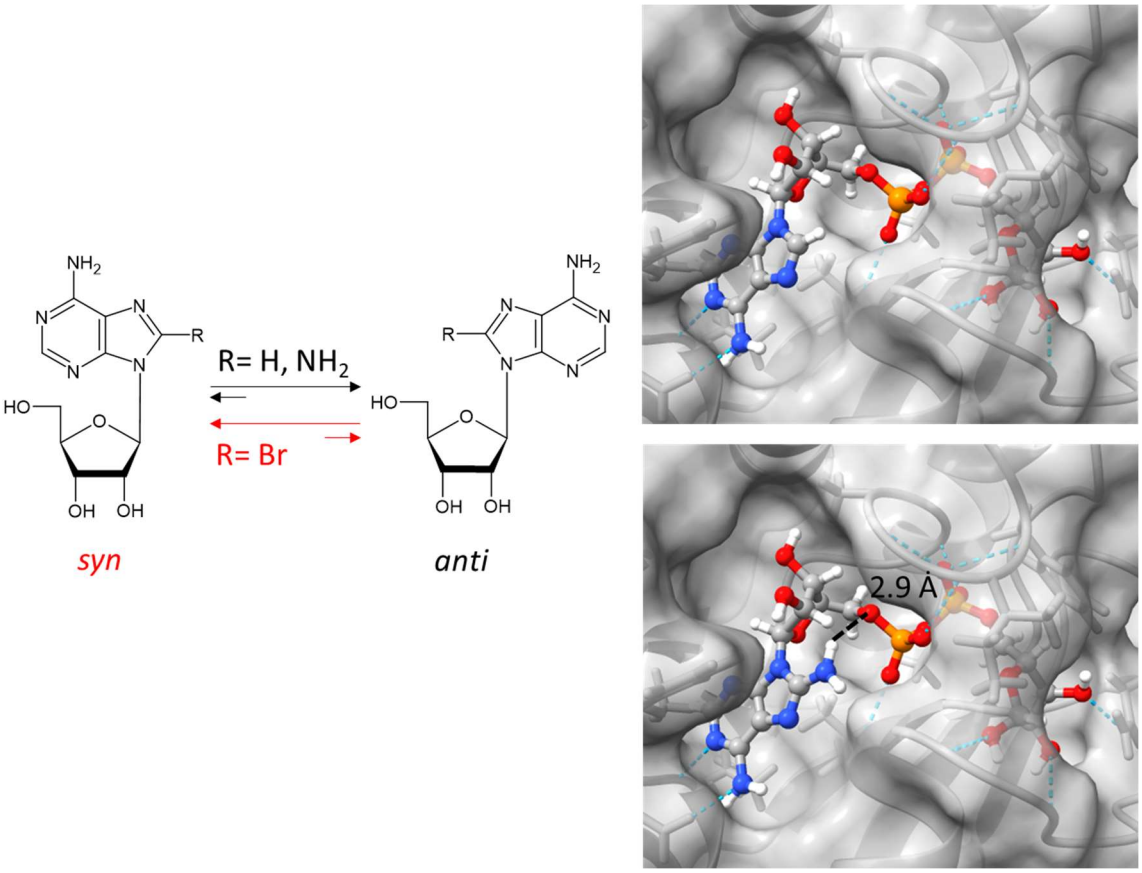

Figure 41: Comparison of prospected effects of C8 derivatives of the adenosine base on ligand conformation and Mac1 binding.
Shown is a sketch (left) of the equilibrium of the *syn*- and *anti*-state of the nucleobase upon modification and the co-crystal structures (right) of Mac1 with ADPR (top, PDB: 8AZD) and a simulated complex with 8-amino-ADPR (bottom). Dashed blue lines indicate the predicted H-bond interactions and dashed black lines depict the expected distance between the C8 amino group and O5′.

6.1.2.2 SAR of the adenosine ribose of ADPR

Across different ADP and ADPR derivatives, modifications at the C2′- and C3′-position of the adenosine ribose resulted in less potent Mac1 inhibition. Although binding modes of the 2′-deoxy-ADPR, 2′-F-2′-deoxy-ADPR were very similar to

ADPR (Figure 42), in each case, ligand binding was somewhat entropically unfavored. Since the C2′ of the adenosine ribose points out of the binding pocket, steric clashes with Mac1 induced by the hydroxyl-modifications could not explain the lower affinities, which therefore are more likely a result from changes of the ribose geometry.

Normally, adenosine appears in *N*-configuration (Figure 43), but modifications at the C2′ and C3′ have been shown to influence the dynamic equilibrium with the *S*-state (Klimke et al., 1979). Thus, removal of the 2′-hydroxyl group or substitution by an amine favor the *S*-pucker (Evich et al., 2017) and prime the adenine in *syn*-conformation (Klimke et al., 1979), thereby impairing Mac1 ligand binding as discussed for the C8-modified compounds in section 6.1.2.1.

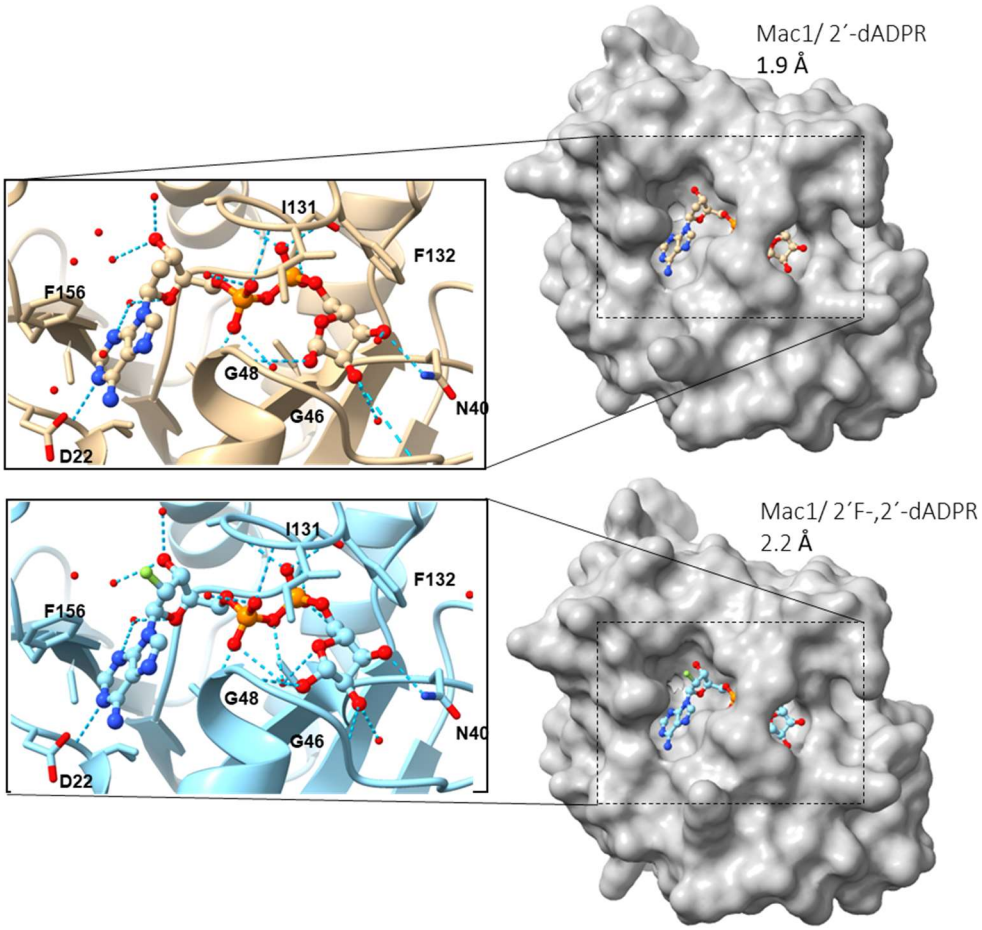

Figure 42: Co-crystal structures of Mac1 in complex with 2′-deoxy-ADPR and 2′-F-2′-deoxy-ADPR.
The right panel shows the ligand-bound structures of Mac1 with either 2′-deoxy-ADPR (top, PDB: 8AZI) or 2′-F-2′-deoxy-ADPR (bottom, PDB: 8AZL). The left panel depicts the zoom-ins of the predicted hydrogen bond interactions (blue meshed lines) between the protein and the respective ligands.

In contrast, polar mimicking of the 2′-OH by a fluorine or substitution of the 3′-OH for an amino-group stabilizes the *N*-conformer and prompt the nucleobase in *anti*-state (Klimke et al., 1979). Although an *anti*-configurated adenine base should result in improved substrate competition with Mac1, the induced changes of the adenosine ribose puckering, maybe in combination with alterations of N-glycosidic bond length (Abola & Sundaralingam, 1973; Devereaux et al., 2019) provoke an additional constrainment of the ligand and thus, adversely effect affinity.

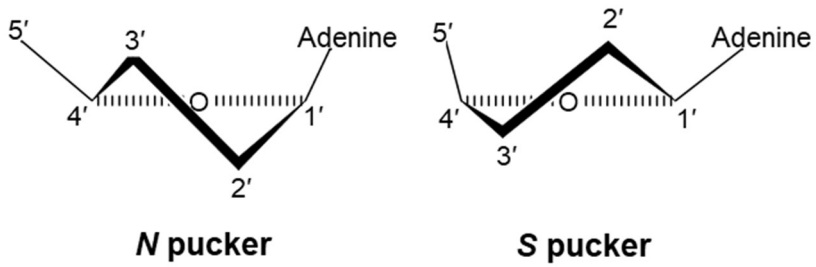

Figure 43: *Northern* (*N*) and *southern* (*S*) sugar puckering of adenosine. Depicted is the pseudorotation of the ribose ring of adenosine (according to Klimke et al., 1979) resulting in two distinct sugar conformers.

In conclusion, the adenosine ribose of ADPR is highly coordinated within the Mac1 binding pocket and preserves the *anti*-configuration of the adenine base, thereby aiding ligand engagement.

6.1.2.3 SAR of the pyrophosphate of ADPR

Upon Mac1 binding, the pyrophosphate moiety of ADPR is engulfed by two closing loops (S128-F132 and G47-V49), forming a strong hydrogen bond interaction network between the phosphate oxygens and the protein (Figure 44), which is consistent with previously published highly-resolution co-crystal structures (Correy et al., 2022).

Since the pyrophosphate of nucleotides is partially protonated at physiological pH (Stockbridge & Wolfenden, 2011), a lower pK_a due to substitution of the phosphate moieties with thiophosphonates (Frey & Sammons, 1985) improved Mac1 inhibition, because of the decreased likelihood of protonation at the α-

phosph(on)ate, promoting hydrogen-bonding with the adjacent backbone NH of V49 and I131 respectively.

In addition, none of the tested pyrophosphate bioisosteres turned out to be suitable Mac1 inhibitors, probably because critical attributes of the parental pyrophosphate, like the pK_a as well as the chemical and structural architecture were barely matched by the isosteres (Berkowitz et al., 2000; Elliott et al., 2012). Taken together, the pyrophosphate of ADPR is embedded in a highly conserved interaction network with Mac1, which requires sufficiently strong and spatially correct formation of hydrogen bonds inside the narrow pyrophosphate tunnel.

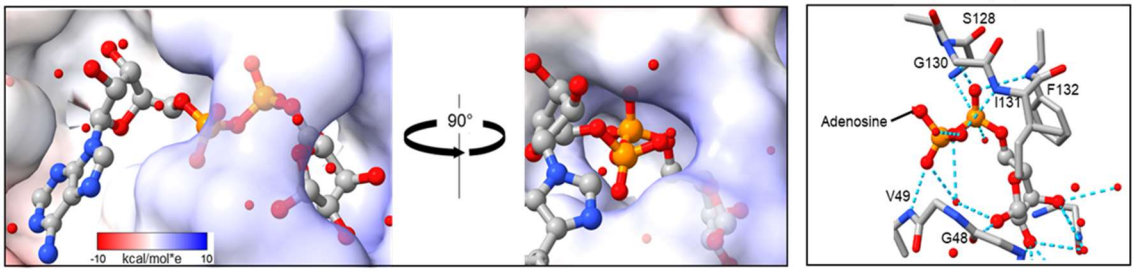

Figure 44: Interaction of the pyrophosphate of ADPR with Mac1.
Shown are the coulomb surface representation of the ADPR-bound Mac1 complex (left box, PDB: 8AZD) and a section of the predicted hydrogen bond interactions (blue meshed lines) between the protein and the pyrophosphate of ADPR (right box).

6.1.2.4 SAR of the terminal ribose of ADPR

In aquaeus solution ADPR is a very flexible molecule but becomes highly coordinated in complex with Mac1, resulting in entropic penalties. Also, among the functional groups of ADPR, the terminal ribose was found to be sterically constrained by the neighboring phenylalanine, since a F132A mutation allowed for higher degree of freedom of the ligand inside the binding pocket, which was entropically favored and consistent with previous reports (Frick et al., 2020; Michalska et al., 2020).

In line with that, substitution of the terminal ribose of ADPR by neither a bulky glucose nor placement of a cyclopentyl-group directly at the pyrophosphate were compatible with the spatial restrictions of the binding site for the terminal ribose.

However, the strong hydrogen-bonding of Mac1 with the hydroxyl groups at the C1″, C2″ and C3″ of ADPR compensated for the constrainment of the terminal ribose, as deficiency of these OH-groups resulted in poor inhibitors of the viral macrodomain.

In conclusion, hydrogen-bond interaction with the protein backbone as well as the furanose structure of the terminal ribose of ADPR contribute to Mac1 binding.

6.1.3 Generation of potent Mac1 inhibitors via β-alkylation of nucleoside diphosphates

The majority of the tested ADP derivatives, lacking the terminal ribose or a suitable replacement thereof had poor activity towards Mac1, which is consistent with a previous report showing that Mac1 is not thermally stabilized by ADP (Michalska et al., 2020). That is likely a result of the additional negative charge at the β-phosphate of ADP, elevating local electrostatic repulsion with the hydrophobic environment (I132 and F132), which is not the case for nucleoside diphosphates forming an additional ester at the pyrophosphate, e.g. ADPR or β-alkylated adenosine diphosphates. This is in line with the higher affinity of Mac1 for β-methyl-GS-441524-diphosphate compared to the parental GS-441524-diphosphate.

Whilst binding modes of both, β-methyl-ADP and β-ethyl-ADP were very similar to ADPR (Figure 45), substitution of the terminal ribose for the smaller alkyl-groups was entropically favored, presumably due to lower sterical constrainment inside the narrow binding pocket for the terminal ribose.

Importantly, β-ethyl-ADP had a lower inhibitory potency against Mac1 than β-methyl-ADP, likely because of a weaker acidic strength of the phosphoric esters with longer alkyl-chains (Kumler & Eiler, 1943) and consequently impaired hydrogen-bonding with Mac1 (as discussed in section 6.1.2.3), which results in release of less net binding enthalpy.

Taken together, whilst β-alkylation of adenosine- and GS-441524-diphosphates improves polar compatibility with the terminal ribose binding site, the alkyl-chain length is negatively correlated with Mac1 binding affinity.

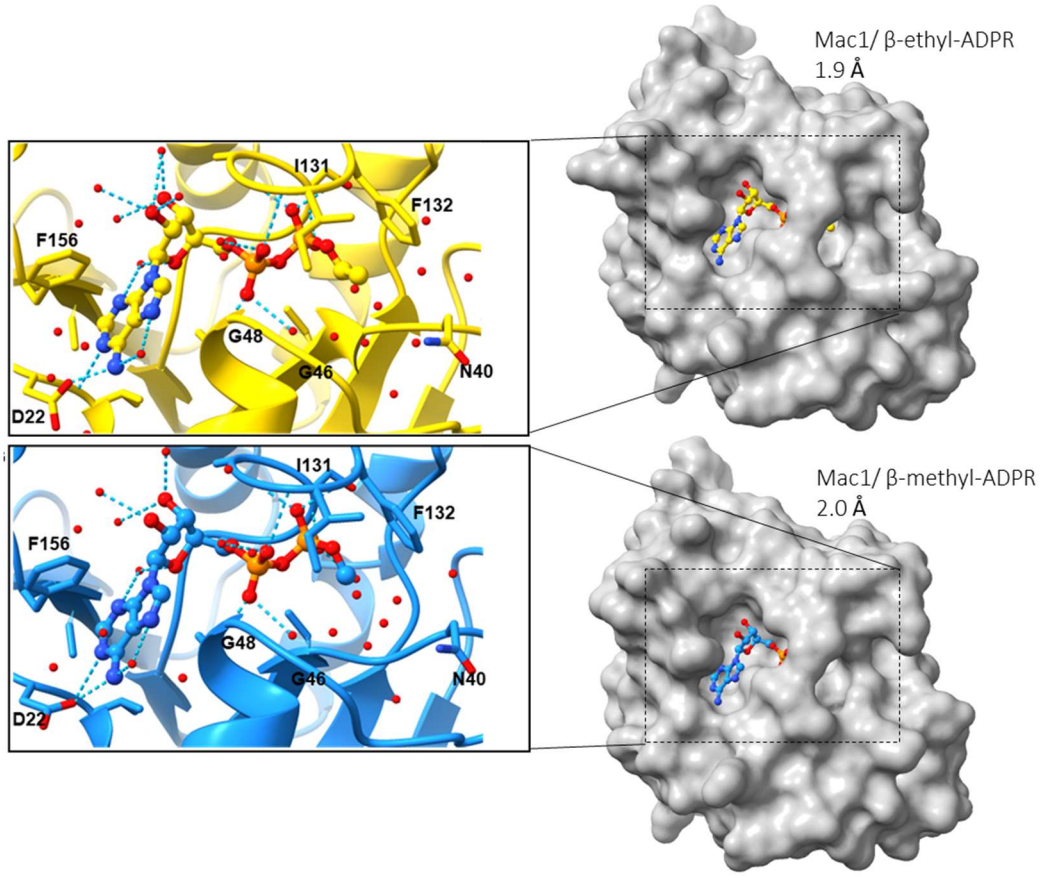

Figure 45: Co-crystal structures of Mac1 in complex with β-ethyl-ADP and β-methyl-ADP.
The right panel show the ligand-bound structures of Mac1 with either β-ethyl-ADP (top, PDB: 8AZO) or β-methyl-ADP (bottom, PDB: 8AZP). The left panel depict the zoom-ins of the predicted hydrogen bond interactions (blue meshed lines) between the protein and the respective ligands.

6.1.4 Initial pharmacological assessment of β-methyl-GS-441524-5′-diphosphate derivatives for Mac1 inhibition

Within the scope of this work, initial parameters, e.g. binding mode and molecular interaction, off-target effects and pan-specific potential of β-methyl-GS-441524-5′-diphosphate as well as absorption, metabolism and toxicity of the prodrug were tested.

However, testing for compound distribution and excretion were not conducted and remain the subject of future studies to further investigate the ADMET.

6.1.4.1 Binding mode and molecular interactions of β-methyl-GS-441524-5′-diphosphate

Cocrystal data of Mac1 binding with β-methyl-GS-441524-5′-diphosphate showed that binding mode was nearly identical to β-methyl-ADP (Figure 45) and ADPR (Figure 46). In contrast to the physiological ligand, the nitrile group as well as the nucleobase of β-methyl-GS-441524-5′-diphosphate were predicted to engage in hydrogen-bond interactions with Mac1, improving shape complementarity with the nucleoside moiety similar to the previously reported structure of Mac1 bound to GS-441524 (PDB: 7BF6) (Ni et al., 2020).

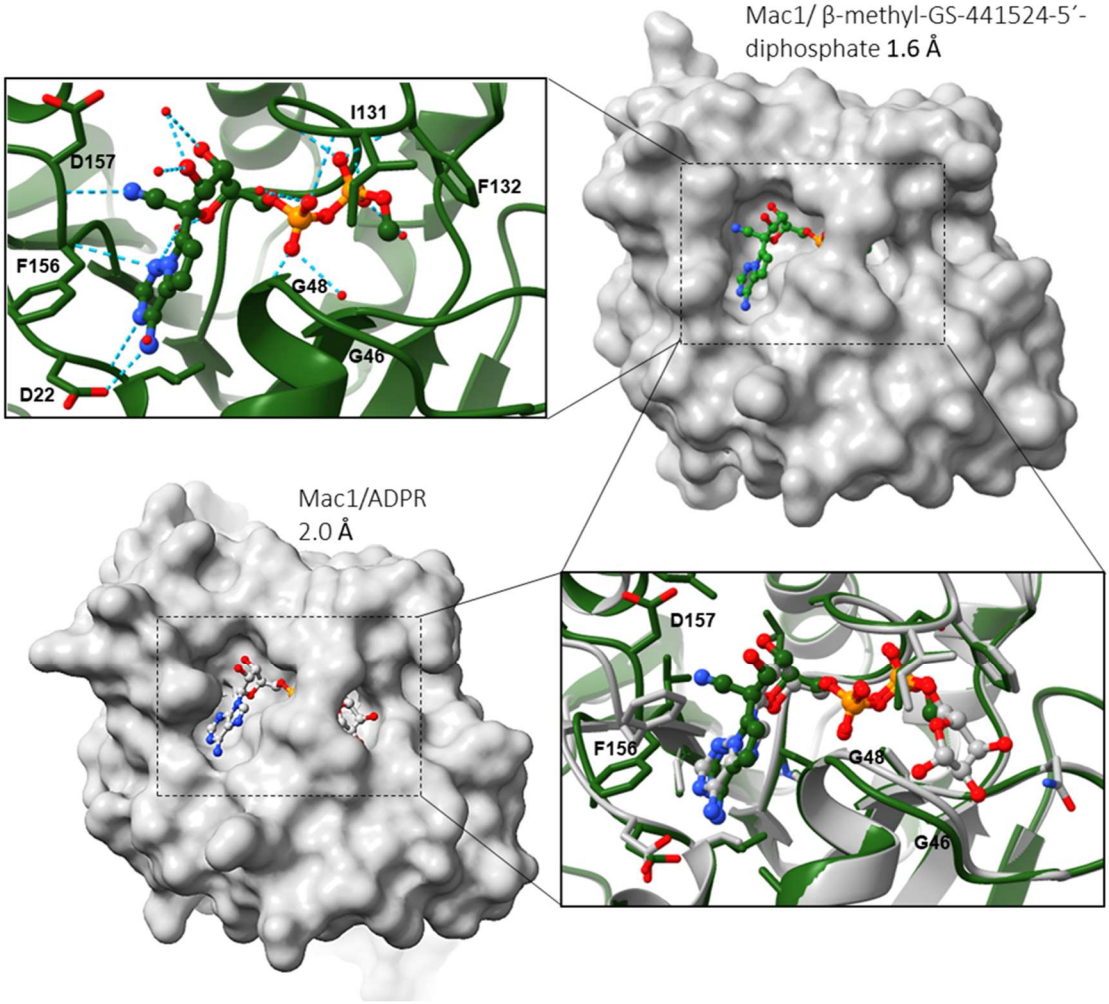

Figure 46: Comparison of the co-crystal structures of Mac1 in complex with β-methyl-GS-441524-5′-diphosphate and ADPR.
The top panel show the ligand-bound structure of Mac1 with β-methyl-GS-441524-5′-diphosphate (right, unpublished) and a zoom-in of the predicted hydrogen bond interactions (blue meshed lines) between the protein and the ligand (left). Bottom panel shows superimposed co-crystals Mac1 complexes with ADPR (grey, PDB: 8AZD) and β-methyl-GS-441524-5′-diphosphate (green).

Consistently, Mac1 binding to β-methyl-GS-441524-5′-diphosphate resulted in a net binding enthalpy slightly higher than for binding to β-methyl-ADP and nearly as high as for binding to ADPR. Displacement of water molecules in the adenosine binding site by the nitrile group of the β-methyl-GS-441524-5′-diphosphate increased entropy (versus β-methyl-ADP and ADPR) and thus, affinity for the viral macrodomain.

6.1.4.2 Absorption of the prodrug

Uptake of β-methyl-GS-441524-5′-diphosphate was rather poor and dectectable in CaLu-3 cells only at high treatment concentrations (50 µM). This might reflect unspecific binding to extracellular receptors for the GS-441524 nucleoside (Rasmussen et al., 2021). The prodrug in contrast showed superior membrane permeability, even at lower treatment concentrations.

Remarkably, even after one hour of prodrug treatment, accumulation of the deprotected β-methyl-GS-441524-5′-diphosphate in the Calu-3 cells did not reach equilibrium and exceeded the extracellular concentrations (0.16 mM or 0.06 mM β-methyl-GS-441524-5′-diphosphate for treatment with 50 µM or 5 µM prodrug respectively).

Of note, whilst incubation with 500 nM prodrug did not yield detectable intracellular β-methyl-GS-441524-5′-diphosphate signals, the maximal intracellular concentration was extrapolated to be ~ 0.02 mM from the other conditions, which would allow for complete Mac1 inhibiton.

The sustained cellular uptake of the prodrug appears to be a result of the enzymatic removal of the masking group by cellular esterases (reviewed by Meier, 2017), releasing the β-methyl-GS-441524-5′-diphosphate inside the cell. This deprotected compound is charged and thus can not cross the apolar membrane, thereby preserving the concentration gradient and uptake of the prodrug.

6.1.4.3 Metabolization of the prodrug

In contrast to β-methyl-GS-441524-5′-diphosphate, the prodrug was less biostable. Although rapid hydrolysis of the masking group would be certainly advantageous for compound uptake, formation of considerable amounts of GS-441524-5′-monophosphate indicate that the mask destabilizes the pyrophosphate bridge, which has been reported earlier for similar prodrugs (reviewed by Meier, 2017).

Although metabolization of the prodrug to GS-441524-5′-monophosphate compromises Mac1 inhibition, the subsequent formation of GS-441524-5′-triphosphate by cellular kinases would allow for an additional impairment of the RNA-dependent RNA-polymerase (RdRP) of SARS-CoV-2 (Rasmussen et al., 2021; Wang et al., 2022). This dual mode of action of the prodrug harbors the potential for efficient blockage of the viral propagation via two distinct pathways, i.e. ADP-ribosylation/ type-I IFN and the viral RNA replication axis.

6.1.4.4 Toxicity of the prodrug

Whilst GS-441524 had no effect on CaLu-3 cell viability (CC_{50} > 100 µM), which is in line with a previous report (Barua et al., 2023), the prodrug was at least 3-fold more cytotoxic, which is in the same range as similarly masked compounds (Weinschenk, 2015).

Consistently, co-incubation of CaLu-3 cells with the prodrug induced a decline of intracellular β-NAD levels, which is associated with cell stress (reviewed in Sedlackova & Korolchuk, 2020), whereas treatment with the unmasked β-methyl-GS-441524-5′-diphosphate was well tolerated, suggesting that the C_{11}-AB-moiety is cytotoxic.

Furthermore, given the efficient intracellular delivery of the masked β-methyl-GS-441524-5′-diphosphate, the initially calculated SI of 30 for the prodrug might be underestimated. In fact, preliminary data from SARS-CoV-2 infection assays, which were conducted by Susanne Pfefferle at the Universitätsklinikum Hamburg-Eppendorf (UKE) indicated an IC_{50} of ~0.2 µM for the prodrug (personal communication). Thus, the resulting SI ≈ 150 would suggest the C_{11}-AB-masked

β-methyl-GS-441524-5′-diphosphate as better option for SARS-CoV-2 treatment than remdesivir, which is a phosphoramidite prodrug of GS-441524-5′-monophosphate and a known inhibitor of the RdRP, which has an $IC_{50} \approx 0.8\mu M$, and SI = 129 (Wang et al., 2020).

6.1.4.5 Off-target effects and pan-specific potential of β-methyl-GS-441524-5′-diphosphate

Due to the high sequence and structure conservation among viral macrodomains, inhibition of their enzymatic activity poses the chance of generating multivalent antivirals, thereby hopefully improving future resilience against new SARS-CoV-2 variants but also against outbreaks of other emerging viruses (Alhammad & Fehr, 2020; Rack et al., 2020b). Thus, Mac1 competitors like β-methyl-GS-441524-5′-diphosphate should also be screened against additional viral macrodomains to assess their pan-specific potential in the future.

In contrast, sequence differences with human macrodomains can be exploited for the design of selective Mac1 inhibitors, as it was demonstrated by utilizing GS-441524 derivatives. As shown in section 6.1.4.1, the negatively charged nitrile groups of β-methyl-GS-441524-5′-diphosphate is localized in the oxyanion subsite, allowing for ion-dipol-interaction with the Mac1 backbone.

While this oxyanion hole is mostly neighbored by apolar residues in macrodomains of different viral clades (e.g. SARS-2 and VEEV), an aspartate is occupying the space proximal to this subsite in human macrodomain proteins MacroD1 and MacroD2 (Figure 47), likely resulting in increased electrostatic repulsion and thereby low off-target effects of GS-441524-based antivirals.

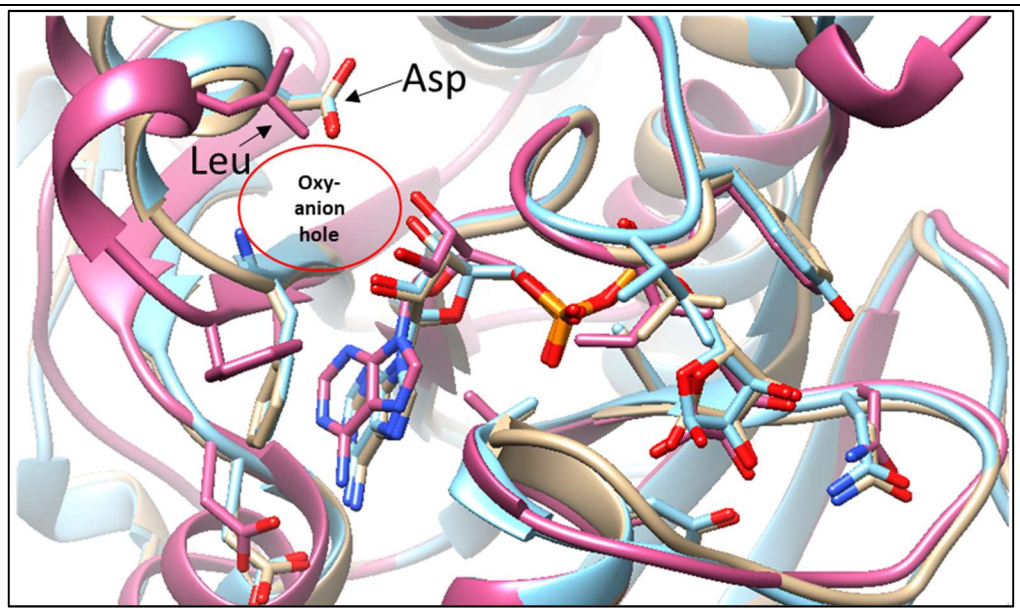

Figure 47: Superimposition of published ADPR-bound structures of viral and human macrodomains.
Shown are the overlayed ADPR co-crystal structures of Mac1 (purple, PDB: 7KQP), MacroD1 (grey, PDB: 6LH4) and MacroD2 (blue, PDB: 4IQY). The oxyanione region of Mac1 is in close proximity of a leucine, whereas the analogous region of human MacroD1/ 2 is neighbored by an aspartate.

6.1.5 Catalysis mechanism and potential physiological targets of Mac1

Mac1 appeared to be rather promiscous with regard to the chemical nature of the substrate, since ADP-ribosylated PARP10 as well as some nucleotides were accepted, which is in line with previous reports suggesting a wide range of non-protein and protein targets *in vitro* (Rack et al., 2020b; Alhammad et al., 2021; Chea et al., 2023).

As part of the nucleotide spectrum of substrates, Mac1 only hydrolyzed α- but not β-NAD, which is consistent with a recent report (Chea et al., 2023) and confirmed the stereoselective hydrolase activity similar to human and bacterial ADP-ribosylhydrolases (Drown et al., 2018; Stevens et al., 2019). This strongly argued against the previously proposed enzymatic mechanism for Mac1, which would allow for binding of β-anomeric substrates and potentially also β-NADase activity (Correy et al., 2022).

Whilst the enzymatic mechanism for Mac1 is still of debate, the most frequently discussed model is the substrate-assisted catalysis (Michalska et al., 2020;

Rack et al., 2020b; Correy et al., 2022). This mechanism has also been discussed for other macrodomain enzymes and involves the i) coordination and ii) activation of a water molecule between the α-phosphate and the terminal ribose of the ADPR-moiety, allowing for iii) nucleophilic attack of the C1″ by the water molecule via S_N2-type substitution reaction and final release of free ADPR (reviewed in Rack et al., 2020a).

This model is supported on the one hand by mutagenesis studies of the viral macrodomain, whereby the enzymatic activity of Mac1 was dependent on F132, which is located at the terminal ribose binding site and constraints ADPR in an entropically unfavored U-like shape, thereby favoring the coordination of the C1″ at the active site of Mac1.

On the other hand, the candidate nucleophile was found across all of the cocrystals presented in this work as well as in related high-resolution structures that were previously reported (PDB:6WOJ, 6W02, 7TX0, 7KQP), hinting towards a conserved structural or even catalytic function. However, α-1″-*O*-methyl-ADPR was no Mac1 substrate despite the accessibility of the C1″ by the nucleophilic water molecule (Figure 48).

This is probably due to an insufficient activation of the water molecule by the low pKa of the α-phosphate (reviewed in Barkauskaite et al., 2015), which does not enable the nucleophilic attack of a rather stable ether O-glycosidic linkage (Okumura et al., 2011), like the one of 1″-*O*-methylated ADPR. In contrast, auto-modified PARP10 is mainly ADP-ribosylated at acidic residues (reviewed in Feijs & Žaja, 2022), thereby forming less stable aspartyl- and glutamyl-esters with ADPR (Tashiro et al., 2023), that are thereby prone to cleavage by Mac1.

Consistently, the poor, yet detectable conversion of TFMU-ADPR by Mac1 correlated also with the stability of the 1″-glycosidic linkage, since acidity and thereby bond reactivity of the leaving group are expected to be higher for TFMU derivatives (e.g. pKa ~ 7.5 for umbelliferone, https://chemaxon.com/calculators-and-predictors) compared to methanol (pKa ~ 16, https://chemaxon.com/calculators-and-predictors), which is one product of the cleavage of the 1″-glycosidic bond of α-1″-*O*-methyl-ADPR.

The fact that alpha-anomeric 1″-*O*- and N-glycosides were among the accepted substrates of Mac1 suggested that not the chemical nature but rather the overall

bond stability was governing hydrolase activity. This is also in line with a previous report showing that neither serine- nor argine-conjugated ADPR were hydrolyzable by Mac1 (Chea et al., 2023), which are both forming comparably stable glycosidc linkages (Voorneveld et al., 2018; Makarov & Migaud, 2019; Voornefeld et al., 2022; Tashiro et al., 2023).

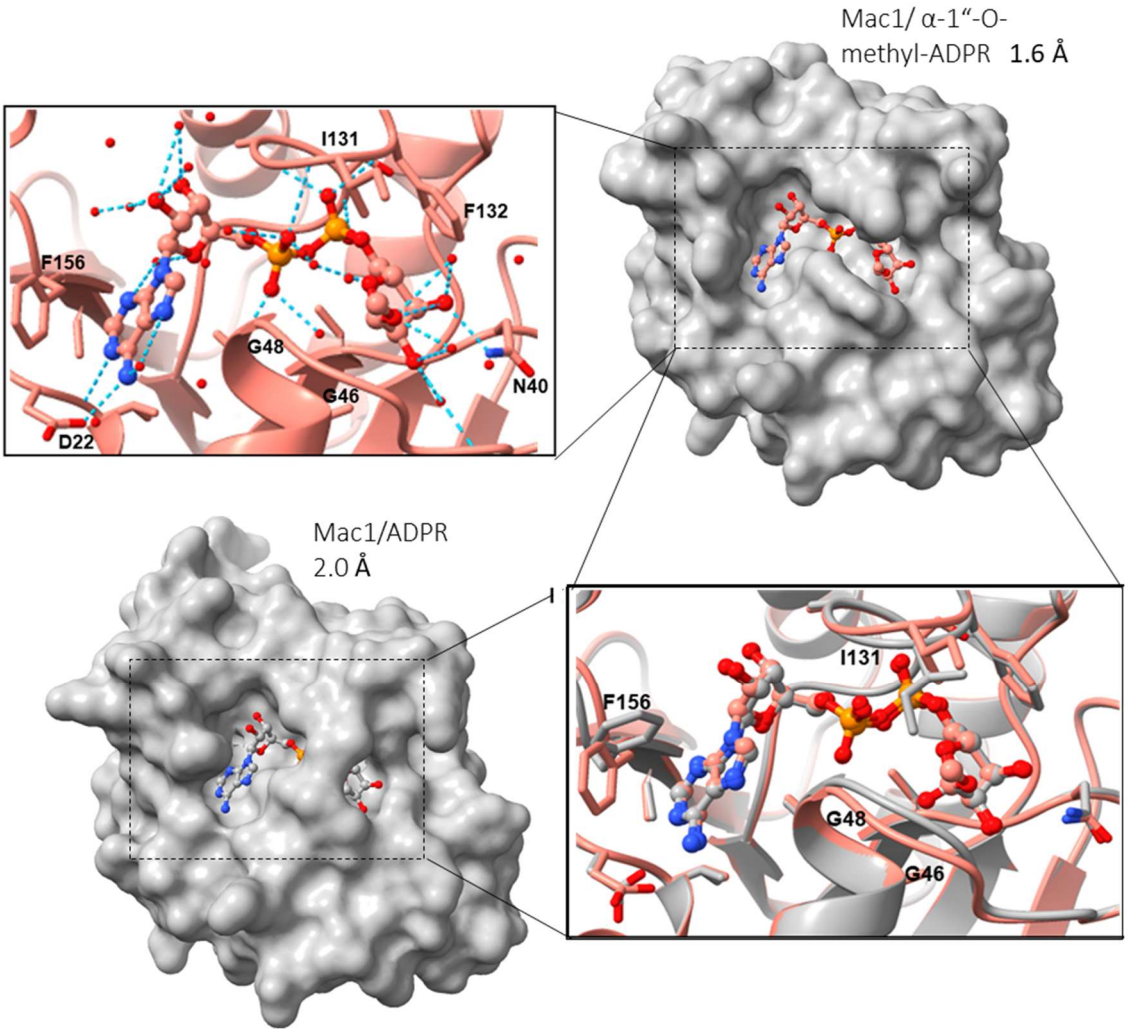

Figure 48: Comparison of the co-crystal structures of Mac1 in complex with α-1″-*O*-methyl-ADPR and ADPR.
The top panel show the ligand-bound structure of Mac1 with α-1″-*O*-methyl-ADPR (right, PDB: 8AZN) and a zoom-in of the predicted hydrogen bond interactions (blue meshed lines) between the protein and the ligand (left). Bottom panel shows superimposed co-crystals Mac1 complexes with ADPR (grey) and α-1″-*O*-methyl-ADPR (pink).

Remarkably, engagement of α-1″-*O*-methyl-ADPR by Mac1 resulted in a partially opened, apo-like conformation of the binding pocket. The i) structural

rearrangements of both closing loop (G46-G48) and I131, which were pushed outside, in combination with the ii) rearrangements of the H-bond interaction network at the terminal ribose upon methylation resulted in lower binding affinity but also demonstrated the plasticity of the interaction of Mac1 with its ligands.

Thus, despite the recent reports that argue against a de-PARylase function of Mac1 and support de-MARylating activity exclusively for acidic target sites (Alhammad et al., 2021; Chea et al., 2023), the binding of Mac1 towards α-1″-*O*-methyl-ADPR, mimicking the O-glycosidic linkage found in e.g. ADP-ribosylated serines or in PARylated molecules, increases the spectrum of potential interaction partners beyond hydrolase function.

It will be of interest in the future, if Mac1, besides the de-ADP-ribosylase activity might also have additional roles, e.g. binding of MARylated substrates or PAR, as the latter has been *in-silico* modelled in complex with the viral macrodomain previously (Rack et al., 2020a).

For instance, PAR binding might also have pro-viral functions e.g. scavenging of unconjugated ADPR polymers, which has been shown to prevent stress granule recruitment of PARP12, an MARylating enzyme that is upregulated in SARS-CoV-2 infections (Heer et al., 2020) and exhibits anti-viral functions in many instances (reviewed by Fehr et al., 2020).

7 Material and Methods

This chapter summarizes the materials and experimental protocols that were used in this study.

7.1 Biological materials, chemicals, instruments and labware

Table 7: Instruments

Designation	Manufacturer
Äkta pure FPLC system	GE Healthcare
Balance 400M	Precisa
Centrifuge 5810 R	Eppendorf
CF1 cell disruptor	Constant Systems Ltd
CK2 microscope	Olympus
Converter plate	Vilber Lourmat
Fusion FX	Vilber Lourmat
Heraeus incubator	Thermo
HERASafe KSP laminar flow hood	Thermo Fisher Scientific
HPLC 1260 Infinite system	Agilent Technologies
Infinite M plex plate reader	Tecan
LEX 12-6x500 rotor	Thermo Scientific
LEX 20-12x50 rotor	Thermo Scientific
Mastercycler	Eppendorf
Mettler H54 precision balance	Mettler
MicroCal iTC200	Malvern Panalytical
Mini Protean Tetra Cell	Bio-Rad
Multichannel pipette, 8-channel, 10-100 µl	Eppendorf
Multitron Standard bacteria shaker	Infors HT
Nanodrop One[c]	Thermo Scientific
PEAQ-ITC	Malvern Panalytical
Pipetboy 2	Integra

Table 7 (continued)

Designation	Manufacturer
Power Pac^{HC}	Bio-Rad
Purelab® Chorus	ELGA LabWater
Seven Compact pH Meter	Mettler Toledo
Sonorex Super RK 100 H	Bandelin
Sorvall LYNX 6000 centrifuge	Thermo Scientific
Superdex 75 Increase 10/300 GL	Cytiva
Thermomixer compact	Eppendorf
Trayster digital tube rotator	IKA
VX-150 Autoclave	Systec

Table 8: General chemicals and reagents

Designation	Remarks	Supplier
Acetophenon	99% purity	Sigma Aldrich
Bromphenol Blue	sodium salt, ≥90% purity	Sigma Aldrich
CellTiter 96® AQueous One Solution		Promega
Chloramphenicol	≥98.5% purity	Th. Geyer
cOmplete EDTA-free protease inhibitor	tablet	Roche
Coomassie staining	Bio-Safe solution	Bio-Rad
DL-Dithiothreitol (DTT)	≥98% purity	Sigma Aldrich
DMEM	high glucose, Glutamax supplement	Thermo Fisher Scientific
Ethanol	>99.9% purity	Th. Geyer
$FeCl_3$	≥97% purity	Sigma Aldrich
Foetal calf serum		Biochrom
Formic acid	≥99% purity	Th. Geyer
Glucose x H_2O	≥98% purity	Merck
Glycerol	87%	Cytiva

Table 8 (continued)

Designation	Remarks	Supplier
Glycine	≥99% purity	Sigma Aldrich
HCl	>25%	Th. Geyer
HEPES	≥99.5% purity	Th. Geyer
Imidazole	≥95% purity	Th. Geyer
Kanamycin	≥95% purity	Th. Geyer
KCl	≥99% purity	Sigma Aldrich
KH_2PO_4	≥99% purity	Sigma Aldrich
KOH	90% purity	Sigma Aldrich
Methanol	≥99.8% purity	Th. Geyer
$MgCl_2$ x $6H_2O$	≥98% purity	Sigma Aldrich
$MgSO_4$ x H_2O	≥99% purity	Carl Roth
Mini-Protean precast gel	4-20% polyacrylamide	Bio-Rad
Na_2HPO_4 x $7H_2O$	≥98% purity	Sigma Aldrich
Na_2SO_4	≥95% purity	Sigma Aldrich
NaCl	≥99% purity	Th. Geyer
NaOH	≥99.8% purity	Sigma Aldrich
NH_4Cl	≥99.5% purity	Sigma Aldrich
Non-essential amino acids	100x solution	Thermo Fisher Scientific
Penicillin-Streptomycin	100x solution	Thermo Fisher Scientific
Phosphate buffered saline (PBS)	without Ca^{2+} and Mg^{2+}	Thermo Fisher Scientific
Pre-stained protein marker	PageRuler™ Plus, 10-250 kDa	Thermo Fisher Scientific
Pyruvate	100 mM solution	Thermo Fisher Scientific
Sodium dodecyl sulfate (SDS)	≥99% purity	Sigma Aldrich
Tris Base	≥99.9% purity	Sigma Aldrich
Triton X-100	reduced	Sigma Aldrich
Trypan blue	0.4% solution	Invitrogen

Table 8 (continued)

Designation	Remarks	Supplier
Trypsin-EDTA	10x solution	Sigma Aldrich
Tryptone		Carl Roth
Yeast extract		Sigma Aldrich
α-lactose x H_2O	≥95% purity	Carl Roth

Table 9: General consumables, plastic and glass ware

Designation	Remarks	Supplier
96-well black polypropylene flat-bottom plates		Greiner
96-well flat transparent bottom plates	sterile (irradiated)	Greiner
96-well twin.tec semi-skirted PCR plates		Eppendorf
Amicon concentrator	3 kDa and 10 kDa cutoff	Merck
Brand tips	0.1 - 20µl	Sigma Aldrich
Centrifugal concentrator	10kDa cutoff	Pall
Centrifuge bottle	500ml, polypropylene copolymer	Thermo Fisher Scientific
Eppendorf tubes	1.5ml, safe lock	Eppendorf
Eppendorf pipets	2, 5, 10, 20, 100, 200, 1000 µl	Eppendorf
Erlenmeyer flaks	1 l, baffled	DWK-LifeSciences
Falcon tubes	15, 50 ml	Sarstedt
Microplate sealing tape	optically clear	Sarstedt
Nalgene filter membranes	polyethersulfon, 0.45 µm pore size	Thermo Fisher Scientific
Neubauer chamber	0.1 mm depth, 0.0025 mm^2 area	Marienfeld Superior
Oak ridge centrifuge tubes	30 ml, polypropylene copolymer	Nalgene
Sarstedt tips	10-200 µl, 100-1000 µl	Sarstedt
Serological pipets	5, 10, 25 ml	Sarstedt
Tissue culture vessel	T75, T175, filter cap	Sarstedt

Table 10: Chromatography materials and consumables

Designation	Remarks	Supplier
250 mm × 4.6 mm C8-Luna column	5.0 µm particle size	Phenomenex
5 mL His Trap FF IMAC column	Stored in 20% ethanol	Cytiva
Gluthatione sepharose 4B	Stored in 20% ethanol, 90µm bead size	GE Healthcare
Poly-Prep Chromatography Columns		Bio-Rad
Poly-Prep Column Stack Cap		Bio-Rad
Superdex 75 Increase 10/ 300 GL	Stored in 20% ethanol	Cytivia

Table 11: Enzymes

Designation	Remarks	Supplier
Benzonase® Nuclease	>99% purity, ~25 U/ µl	Sigma Aldrich
MacroD1	human, recombinant His-tagged	Andreas Ladurner, LMU
MacroD2	human, recombinant His-tagged	Andreas Ladurner, LMU
PARG	human, recombinant His-tagged, highly active	Biomol

Table 12: Organisms

Designation	Supplier
CaLu-3 cells	Susanne Pfefferle, University Hospital Hamburg-Eppendorf (UKE)
Rosetta2 (DE3) *E. coli*.	Sigma Aldrich

Table 13: Nucleosides, nucleotides and derivatives

Designation	Remarks	Supplier
1,N^6-etheno-ADPR	sodium salt, >95% purity	Biolog
1″,2′-dideoxy-ADPR	Baszczyňski et al., 2019	Barry VL Potter, University of Bath
2′-amino-2′-deoxy-ADP	sodium salt, >95% purity	Biolog
2′-deoxy-ADP	sodium salt, >95% purity	Biolog

Table 13 (continued)

Designation	Remarks	Supplier
2′-deoxy-ADPR	sodium salt, >95% purity	Biolog
2′-F-2′-deoxy-ADPR	sodium salt, >95% purity	Biolog
2-F-ADPR	Moreau et al., 2013	Barry Potter VL, University of Bath
3″,2′-dideoxy-ADPR	Baszczyński et al., 2019	Barry Potter VL, University of Bath
3′-amino-3′-deoxy-ADP	sodium salt, >95% purity	Biolog
5′-((2-hydroxybenzoyl)-sulfamoyl)-adenosine	Moreau et al., 2013	Barry Potter VL, University of Bath
5′-(2-hydroxy-ethoxy-ethyl-squaryl)-adenosine	Moreau et al., 2013	Barry Potter VL, University of Bath
5′-(butyl-squaryl)-adenosine	Moreau et al., 2013	Barry Potter VL, University of Bath
5′-(ribosyl-squaryl)-adenosine	Moreau et al., 2013	Barry Potter VL, University of Bath
7-deaza-2′-deoxy-ADP	sodium salt, >95% purity	Biolog
7-deaza-ADP	sodium salt, >95% purity	Biolog
7-deaza-IDPR	Moreau et al., 2013	Barry Potter VL, University of Bath
8-amino-ADP	sodium salt, >95% purity	Biolog
8-amino-ADPR	Moreau et al., 2013	Barry Potter VL, University of Bath
8-Br-7-deaza-ADPR	sodium salt, >95% purity	Biolog
8-Br-ADPR	sodium salt, >95% purity	Biolog
8-thiophenyl-ADPR	Moreau et al., 2013	Barry Potter VL, University of Bath
Adenosine	≥99% purity	Sigma Aldrich
Adenosine 5'-O-(2-thiodiphosphate)	sodium salt, >95% purity	Biolog
Adenosine-5′-O-(2-phosphoryl)acetate ribose	Baszczyński et al. 2020	Barry Potter VL, University of Bath
Adenosine-5′-phosphonoacetyl-ribose	Baszczyński et al. 2020	Barry Potter VL, University of Bath
Adenosine-5'-methylenediphosphate	sodium salt, >95% purity	Biolog

Table 13 (continued)

Designation	Remarks	Supplier
Adenosine-5'-methylenediphosphate-ribose	Tóth et al., 2014	László Csanády, Semmelweis University
ADP	sodium salt, ≥95% purity	Sigma Aldrich
ADP-glucose	disodium salt, ≥93% purity	Sigma Aldrich
ADP-HPD x $2H_2O$	ammonium salt, ≥95% purity	Merck
ADPR	sodium salt, ≥93% purity	Sigma Aldrich
ADPRP	sodium salt, >95% purity	Biolog
AMP	sodium salt, ≥95% purity	Sigma Aldrich
cAMP	sodium salt, ≥98% purity	Sigma Aldrich
Cyclopentyl-ADP	Moreau et al., 2013	Barry VL Potter, University of Bath
Fufuryl-ADP	Fliegert et al. 2017	Barry VL Potter, University of Bath
GS-441524	≥99% purity	MedChem Express
GS-441524-5′-diphosphate		Benedikt Ganter, University of Hamburg
GS-441524-5′-monophosphate		Benedikt Ganter, University of Hamburg
IDPR	sodium salt, >95% purity	Biolog
Rp-adenosine 5'-O-(1-thiodiphosphate)	sodium salt, >95% purity	Biolog
Sp-adenosine 5'-O-(1-thiodiphosphate)	sodium salt, >95% purity	Biolog
TFMU-ADPR		Sahra Tajdar, University of Hamburg
TFMU		Sahra Tajdar, University of Hamburg
α-1″-*O*-methyl-ADPR	Fliegert et al. 2017	Barry VL Potter, University of Bath
α-NAD	≥95% purity	Sigma Aldrich
β-1″-*O*-methyl-ADPR	Fliegert et al. 2017	Barry VL Potter, University of Bath

Table 13 (continued)

Designation	Remarks	Supplier
β-ethyl-ADP		Sahra Tajdar, University of Hamburg
β-methyl-ADP	Fliegert et al. 2017	Barry VL Potter, University of Bath
β-methyl-GS-441524-5′-diphosphate		Sahra Tajdar, University of Hamburg
β-NAD	≥99% purity	Roche

Table 14: *In silico* predicted Mac1 ligands

Designation	Remarks	Supplier
CDP-choline	98% purity	Sigma Aldrich
Coenzyme A	sodium salt, ≥85% purity	Sigma Aldrich
Econazole	>98% purity	Sigma Aldrich
Nebivolol	≥98% purity	Sigma Aldrich
Telmisartan	≥98% purity	Thermo Fisher Scientific
Tenofovir	≥98% purity	Sigma Aldrich
β-Estradiol	≥98% purity	Sigma Aldrich
ZINC8765069	≥90% purity, Molport-005-974-659	MolPort
ZINC8792474	≥90% purity, Molport-000-854-145	MolPort
ZINC8879336	≥90% purity, Molport-002-535-735	MolPort
ZINC8879971	≥90% purity, Molport-002-535-872	MolPort

For information on chemical structure see appendix.

Table 15: Compounds identified by virtual screening

Internal identifier (MP number)	MolPort ID	Supplier
1	MolPort-044-684-957	MolPort
2	MolPort-042-561-485	MolPort
3	MolPort-005-785-603	MolPort
4	MolPort-004-220-002	MolPort
5	MolPort-019-648-600	MolPort
6	MolPort-020-099-632	MolPort
7	MolPort-005-729-701	MolPort
8	MolPort-005-687-811	MolPort
9	MolPort-004-073-151	MolPort
10	MolPort-004-122-953	MolPort
11	MolPort-004-236-511	MolPort
12	MolPort-023-132-634	MolPort
13	MolPort-039-308-883	MolPort
14	MolPort-030-003-656	MolPort
15	MolPort-009-303-471	MolPort
16	MolPort-004-233-604	MolPort
17	MolPort-009-627-566	MolPort
18	MolPort-039-236-162	MolPort
19	MolPort-009-256-864	MolPort
20	MolPort-008-340-059	MolPort
21	MolPort-038-430-201	MolPort
22	MolPort-002-731-464	MolPort
23	MolPort-005-988-009	MolPort
24	MolPort-029-999-514	MolPort
25	MolPort-027-847-524	MolPort
26	MolPort-008-334-081	MolPort
27	MolPort-000-814-721	MolPort
28	MolPort-046-597-216	MolPort

All MP compounds exhibited >90% purity. For information on chemical structure see appendix.

7.2 Media recepies

All solutions were prepared in de-ionized water and pH was adjusted using a SevenCompact pH meter. If not stated otherwise, all prepared buffers and solutions were passed through a 0.45 µm membrane. In addition, chromatography and ITC buffers were sonicated for 30 min at room temperature.

Table 16: Buffers and solutions

Name	Components	Remarks
α-NAD assay buffer	20mM KH_2PO_4 4mM $MgCl_2$ 400µM DTT pH = 7.2	
Auto-Induction Medium (1x)	10 g/l tryptone 5 g/l yeast extract 25 mM Na_2HPO_4 25 mM KH_2PO_4 50 mM NH_4Cl 5 mM Na_2SO_4 5 g/l glycerol 0.5 g/l glucose 2 g/l α-lactose 2 mM $MgSO_4$ 10 µM $FeCl_3$	Components (except tryptone and yeast extracts) were prepared as sterile-filtered stock solutions (50x) and diluted to 1x in autoclaved tryptone-yeast extract mixture
de-MARylation buffer	20mM KH_2PO_4 2mM $MgCl_2$ 200µM DTT pH = 7.2	
Detergent solution (5x)	Swelling buffer 5% (l/l) Triton X-100 15 mM $MgCl_2$	Not filtered
Electrode buffer (10x)	30.3 g/l Tris Base 144 g/l glycine 10 g/l SDS	Not filtered

Table 16 (continued)

Name	Components	Remarks
HPLC buffer A	20 mM KH_2PO_4 pH 6.0	
HPLC buffer B	50%(l/l) HPLC buffer A 50%(l/l) methanol	
HPLC buffer C	10%(l/l) HPLC buffer A 90%(l/l) methanol	
IMAC buffer A	50 mM NaH_2PO_4 500 mM NaCl 5 mM imidazole pH = 7.8	
IMAC buffer B	IMAC buffer A 500 mM imidazole	
ITC buffer	20 mM HEPES 150 mM NaCl pH = 7.5	
Isotonic phosphate buffer	10 mM KH_2PO_4 5.5 mM glucose 140 mM NaCl 1 mM $MgSO_4$ 5 mM KCl pH 7.4	
Laemmli buffer (4x)	0.125 M Tris-HCl 40 g/l SDS 435 g/l glycerol 0.1 g/l bromophenol blue pH = 6.8	Not filtered
PARP10 buffer	20 mM KH_2PO_4 400 µM DTT 4 mM MgCl2 pH = 7.2	

Table 16 (continued)

Name	Components	Remarks
SEC buffer	20 mM HEPES 500 mM NaCl pH = 7.8	
Swelling buffer	10 mM KH_2PO_4 pH 7.4	
PARG assay buffer	25 mM KH_2PO_4 1 mM DTT 50 mM KCl pH = 7.5	

7.3 Protocols

7.3.1 Cell culture

If not stated otherwise, cell maintenance and experiments were performed in a laminar flow hood.

CaLu-3 cells were a gift from Susanne Pfefferle (UKE) and were kept in high glucose DMEM with Glutamax, 10 % foetal calf serum, 100 U/ l penicillin, 100 µg/ l streptomycin, 1 mM non-essential amino acids, 1 mM pyruvate at 37˚C in a humidified 5% CO_2 atmosphere provided by a Heraeus incubator.

For cell passage, CaLu-3 cultures were washed three times in phosphate buffered saline (PBS) without bivalent cations. Then cells were detached by enzymatic digest with trypsin-EDTA at 37°C. When approximately 90% of cells were detached, the trypsination was stopped by addition of serum-containing medium. After centrifugation of the cell suspension at 300 x g for 5 min, the supernatant was removed and the cells were re-suspended in fresh medium. Usually, cell density was determined by mixing of a small aliquot of the cell suspension with an equal volume of trypan blue solution and subsequent counting in a Neubauer chamber prior to seeding in a new cell culture flaks or plate.

7.3.2 Recombinant Protein Expression and Purification

7.3.2.1 Production of recombinant His-3C protease

His-3C protease cloned into a pET28 vector, which was a kind gift by Aymelt Itzen (University Medical Center Hamburg, UKE, Germany) was transformed in Rosetta2 (DE3) *E. coli*. Cells were grown at 37°C in auto-induction medium (adopted from Studier, 2005), which was supplemented with 60 µg/ ml kanamycin and 34 µg/ ml chloramphenicol. The cells were harvested by centrifugation at 5000 x g in 500 ml centrifuge bottles and re-suspended in lysis buffer, containing IMAC buffer A, supplemented with 50 U/ ml benzonase and cOmplete EDTA-free protease inhibitor according to manufacturer recommendations. Cells were lysed by a CF1 cell disruptor at 1.8 kbar. Lysates was cleared by centrifugation at 57.000 x g in 30 ml oak ridge centrifuge tubes. Immobilized metal ion affinity chromatography (IMAC) was performed by loading of the cleared lysate onto a pre-equilibrated 5 mL His Trap FF IMAC column. An Äkta pure FPLC system was used for gradient elution of affinity-bound proteins by increasing concentration of IMAC buffer B in the mobile phase (0% to 100% B in 10 column volumes). The purest protein fractions were pooled and concentrated by a 10 kDa centrifugal concentrator (Amicon) before Äkta-assisted size exclusion chromatography through a pre-equilibrated Superdex 75 Increase 10/ 300 GL column by isocratic elution in SEC buffer. The purest protein fractions were again pooled and concentrated by a 10 kDa Amicon concentrator. Final protein concentration was determined by nanodrop at 280 nm using an extinction coefficient of 6085 M^{-1} cm^{1}, which was estimated by the ProtParam tool (https://web.expasy.org/protparam/) and followed by snap-freezing of small aliquots in liquid N_2 prior to longterm storage at -80°C.

7.3.2.2 Production of SARS-CoV-2 Mac1

Mac1 from SARS-CoV-2 was produced as GST-His-tagged fusion protein in Rosetta2 (DE3) *E. coli* transformed with the pTM33_Nsp3b_ADRP construct, which was a kind gift from Ylva Ivarsson (Addgene plasmid number 156468). Expression, cell lysis and IMAC were performed as described for His-3C-protease. In addition, after an initial IMAC, the tag was enzymatically removed by

3C protease digest. To remove the tag, uncleaved protein and the protease from the sample, a consecutive second IMAC was performed and the macrodomain was collected from the flowthrough. Finally, Mac1 was polished by SEC, concentrated by a 3 kDa centrifugal concentrator (Amicon) and quantified (using a previously published extinction coefficient, Frick et al., 2020) before snap-freezing and storage of Mac1 as described for His-3C-protease.

7.3.2.3 Production of human Parp10

Human PARP10 was produced as GST-tagged fusion protein in Rosetta2 (DE3) *E. coli* transformed with the pGEX_PARP10_GST construct, which was a kind gift from Bernhard Lüscher (RWTH Aachen). Expression and cell lysis were performed similar to His-3C-protease, but instead of IMAC buffer, PARP10 buffer was used for lysis, supplemented with 50 U/ ml benzonase and cOmplete EDTA-free protease inhibitor according to manufacturer recommendations. Next, for affinity purification of the GST-fusion protein, lysates were loaded on a Poly-Prep chromatography column with Gluthatione sepharose beads. The column sealed with column stack cap and incubated over night at 8°C with constant agitation on a rotator. The beads were washed 3 times with PARP10 buffer prior to snap-freezing and storage of the PARP10-loaded beads as described for His-3C-protease.

7.3.3 SDS-polyacrylamide gel electrophoresis (PAGE)

4x Laemmli buffer was diluted to 1x with the protein sample and boiled at 95°C for 5 min. Mixtures were then let cool down to room temperature prior to loading onto a Mini-Protean precast gel (4-20%) mounted in a Mini-Protean Tetra cell electrophoresis chamber filled with 10x Electrode buffer diluted to 1x with H_2O. Proteins were separated by applying 120 V constant for 60 min using a Power Pac^{HC} supply at room temperature. After the electrophoresis, gels were washed three times with water for 5 min before staining the gels over night with coomassie blue. To increase contrast, gels were washed three times with water prior to imaging in a Vilber Fusion FX equipped with a converter plate. Images were further analyzed by the gel band quantification tool implemented in Fiji.

7.3.4 Michaelis Menten Kinetics

Kinetics were started by dilution of a 10x Mac1 stock to a final 1x concentration (50 ng/ µl) in an ice-cold reaction mixture, containing α-NAD assay buffer supplemented with α-NAD as substrate at the indicated concentrations. Samples were incubated at 37°C until substrate conversion reached approximately 5%. To monitor the reaction progress, 50 µl of each condition were sampled, and immediately snap-frozen in liquid N_2 before storage at -80°C. Finally, HPLC analysis (described in section 7.3.7) was conducted to quantify product formation. The resulting initial reaction velocities from product formation were plotted against α-NAD concentration fit to the Michaelis-Menten model with GraphPad Prism 9.

7.3.5 Microplate Assay

For depletion assays, 96-well twin.tec semi-skirted PCR plates were used. In each microcavity, 7 µl of an enzyme stock solution (final assay concentrations were 3 µM Mac1, 1 µM MacroD1, or 3 µM MacroD2, if not stated otherwise) or SEC buffer (for negative controls) were prepared. Reactions were started by addition of 63 µl master mixture, containing 10 µM α-NAD in α-NAD assay buffer, supplemented with the test compounds at the indicated concentrations (if not stated otherwise). Plates were protected by sealing tape, briefly spun down for 1 min at 300 x g and incubated at 37°C for 120 min in a Mastercycler (if not stated otherwise). To determine enzymatic activity with or without inhibitors at the indicated concentrations, the remaining substrate was quantified by post-reaction derivatisation reaction analogous to a recently described procedure (Wazir et al., 2021). Briefly, 50 µl of the reaction mixtures were transferred into black 96-well polypropylene flat-bottom plates containing 20 µl of 2 M KOH. Samples were treated with 20 µl of 25% acetophenone in ethanol for 10 min at room temperature followed by addition of 40 µl 100% formic acid and incubation for another 30 min at room temperature. Finally, the fluorescently derivatized α-NAD was detected with a Tecan Infinite M plex plate reader using excitation at 377 nm and emission at 444 nm. The normalized enzyme activity for a $condition_i$

was calculated from α-NAD consumption as $\frac{[\alpha\text{-NAD}]_{\text{no enzyme}} - [\alpha\text{-NA}\ ]_i}{[\alpha\text{-NAD}]_{\text{no enzyme}} - [\alpha\text{-NAD}]_{\text{uninhibited control}}}$.

7.3.6 HPLC-based enzyme Assay

The HPLC-based assays were conducted similiar to the microplate assay (described in section 7.3.5). In brief, enzyme and substrate concentration, reaction buffers and incubation conditions were kept the same.To determine substrate conversion, with or without inhibitors at the indicated concentrations, the reaction progress was monitored by dilution of 20 µl of the reaction mix in 80 µl ice-cold water, followed by immediate snap-freezing in liquid N_2 and storage at -80°C until further analysis by HPLC. The normalized enzyme activites for a condition$_i$ were calculated from ADPR formation analogous to the microplate assay as $\frac{[\text{ADPR}]_i - [\text{ADPR}]_{\text{no enzyme}}}{[\text{ADPR}]_{\text{uninhibited control}} - [\text{ADPR}]_{\text{no enzyme}}}$.

7.3.7 HPLC analysis

Usually, samples were thawed on ice and passed through a 10 kDa size exclusion filter (Pall). Analysis was conducted on a reversed-phase high performance liquid chromatography system (HPLC) with a C8-Luna column as stationary phase. The mobile phase consisted of HPLC buffer A and B. The percentage of buffer B in the mobile phase was gradually increased to elute the analytes (0 min 0% buffer B, 5 min 0% buffer B, 27.5 min 100% buffer B, 30 min 100% buffer B, 32 min 0% buffer B, 43 min 0% buffer B).

For analysis of cell supernatants and lysates, the mobile phase consisted of HPLC buffer A and C. The percentage of buffer C in the mobile phase was gradually increased to elute the analytes (0 min 0% buffer C, 5 min 0% buffer C, 27.5 min 55% buffer C, 30 min 55% buffer C, 35 min 100% buffer C, 45 min 100% buffer C, 47 min 0% buffer C, 57 min 0% buffer C). The light absorption of the analytes was recorded by the diode array detector (DAD) at the indicated wavelengths. For quantification, peak area integrals were calibrated with the respective external standards.

7.3.8 TFMU-ADPR Assay

For testing of enzymatic hydrolysis, TFMU-ADPR was digested with either 2 nM human PARG in PARG assay buffer or 3 µM Mac1 in α-NAD assay buffer at the indicated concentrations in 96-well black polypropylene plates. Fluorescence was continuously monitored with a Tecan Infinite M plex plate reader using excitation at 384 nm and emission at 502 nm. Signals were substacted from chemical substrate hydrolysis and were finally calibrated by a TFMU standard.

7.3.9 Isothermal titration calorimetry (ITC)

For determination of binding isotherms, both ligands and proteins were solved in ITC buffer. Thus, 750 µM ligand (syringe) was titrated to 50 µM protein (cell) in a total of 19 injections (starting with a single injection of 0.5 µl, followed by 18 injections of 2 µl). The corresponding thermograms were recorded at 25°C under continuous stirring at 750 rpm using a MicroCal iTC200 with the reference power set to 5 µcal/ s for wildtype Mac1, whereas experiments with Mac1 F132A were conducted with a PEAQ-ITC and a reference power of 10 µcal/ s. Data were fit to a one-site binding model using the analysis software supplied by the manufacturer.

7.3.10 Preparation of auto-modified PARP10

MARylated PARP10 was prepared by co-incubation of PARP10-loaded beads with 1 mM β-NAD in PARP10 buffer over night at 4°C. Finally, the beads were washed 3 times with ice-cold PARP10 buffer (without β-NAD) prior to resuspension in PARP10 buffer to obtain a 50% bead slurry. The auto-modified PARP10 samples were immediately snap-frozen in liquid N_2 and stored at -80°C until further use.

7.3.11 De-MARylation assay

For testing of de-ADP-ribosylating activity, auto-modified PARP10 was used as substrate. If not stated otherwise, 0.3 µM Mac1, 1 µM MacroD1 or 3 µM MacroD2 were co-incubated with the substrate in de-MARylation buffer for 30 min at 37°C with or without inhibitors at the indicated concentrations. 20 µL of the reactions

were sampled and diluted in 80 µl ice-cold water before snap-freezing in liquid N_2 and storage at -80°C until further analysis by HPLC (described in section 7.3.7).

7.3.12 Permeability assay

Approximately 40,000 cells were seeded per cavity of a 96-well cell culture plate with a transparent flat bottom and grown until ~90% confluency, which was usually the case after 48-72 h. Then, supernatants were removed and cells were washed with pre-warmed isotonic phosphate buffer 3 times prior to treatment with 50 µl of the test compounds (solved in isotonic phosphate buffer). Co-incubation with the compounds was carried out at 37°C in a humidified cell culture incubator for the indicated time periods. After the treatment, cells were kept on ice and supernatants were collected, snap-frozen in liquid N_2 and stored at -80°C until HPLC analysis. Cells were washed with ice-cold swelling buffer 3 times and incubated for ~5 min on ice in 40 µl swelling buffer. Then, 10 µl of a detergent solution (5x) were added for cell lysis. Cell lysates were immediately passed through a 10 kDa size exclusion filter (Pall) and filtrates were stored at -80°C until further analysis by HPLC (described in section 7.3.7).

7.3.13 MTS-Assay

For testing of cytotoxic effects by the compounds, CaLu-3 cells initially treated with the compounds as described in the permeability assay (section 7.3.12), but after 1 h of incubation, a MTS-assay was conducted by incubating the cells for another hour with cell culture media supplemented with CellTiter 96® AQueous One solution as recommended by the manufacturer. Finally, absorbance at 490 nm was measured by a Tecan Infinite M plex plate reader. Signals were corrected for background absorbance of the CellTiter 96® AQueous One solution and normalized to the untreated cells (without compound).

7.3.14 Software and Statistics

ChemStation Software (Rev. C.01.05, Agilent Technologies) was used for HPLC peak area integration. Visualization and analysis of microplate assay as well as HPLC data (chromatograms and integrals) were performed using GraphPad

Prism 9. ITC data were visualized and processed by MicroCal PEAQ-ITC or MicroCal iTC200 analysis software (Malvern Panalytics) respectively. Fiji software (version 2.35) was used for densitometric analysis of coomassie stained SDS-PAGE gels. Chemical structures were depicted with ChemSketch (2020.2.1., ACD/ Labs). SnapGene Viewer (v.5.3.1) was used for illustration of gene vector maps. Crystallography data and related molecular graphics and analyses were performed with either UCSF Chimera (1.17.3 or version X). If not stated otherwise, all the data are presented as mean ± SD from at least three independent experiments. For statistical testing, analysis of variance (ANOVA) was conducted with GraphPad Prism 9 and the statistical significance level (α) was set to 5%.

8 Appendix

8.1 MP-compounds and *in silico* predicted Mac1 ligands

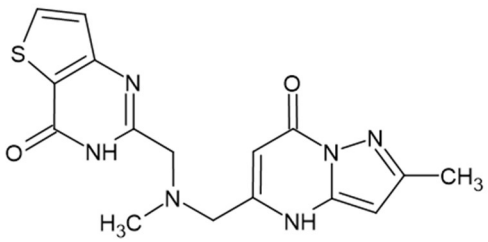

MP1 (MolPort-044-684-957)
2-methyl-5-{[methyl({4-oxo-3H,4H-thieno[3,2-d]pyrimidin-2-yl}methyl)amino]methyl}-4H,7H-pyrazolo[1,5-a]pyrimidin-7-one

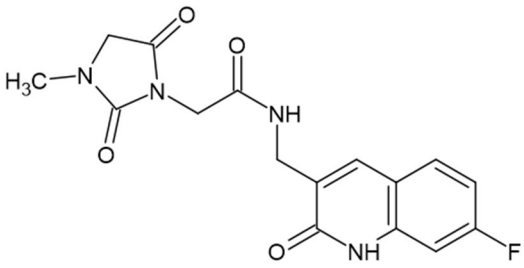

MP2 (MolPort-042-561-485)
N-[(7-fluoro-2-oxo-1,2-dihydroquinolin-3-yl)methyl]-2-(3-methyl-2,5-dioxoimidazolidin-1-yl)acetamide

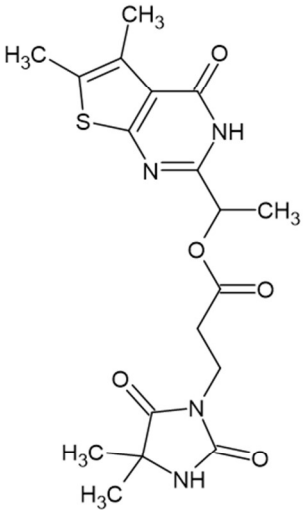

MP3 (MolPort-005-785-603)
1-{5,6-dimethyl-4-oxo-3H,4H-thieno[2,3-d]pyrimidin-2-yl}ethyl 3-(4,4-dimethyl-2,5-dioxoimidazolidin-1-yl)propanoate

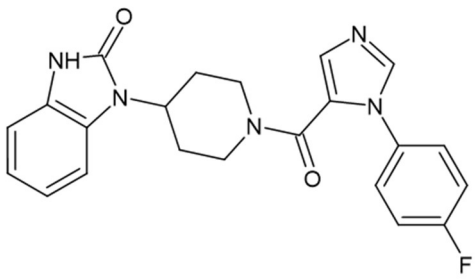

MP4 (MolPort-004-220-002)
1-{1-[1-(4-fluorophenyl)-1H-imidazole-5-carbonyl]piperidin-4-yl}-2,3-dihydro-1H-1,3-benzodiazol-2-one

Figure 49: Chemical structures of MP1-4

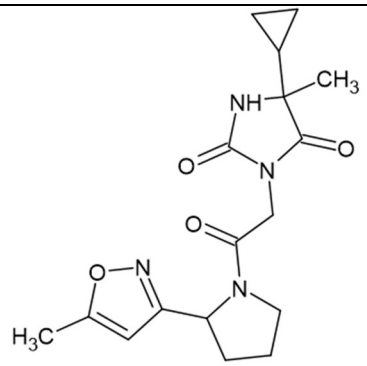

MP5 (MolPort-019-648-600)
5-cyclopropyl-5-methyl-3-{2-[2-(5-methyl-1,2-oxazol-3-yl)pyrrolidin-1-yl]-2-oxoethyl}imidazolidine-2,4-dione

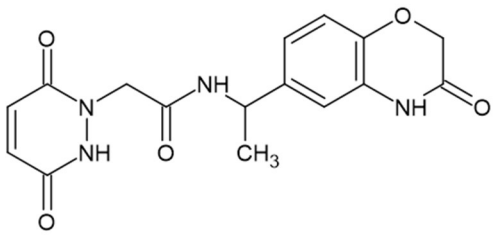

MP6 (MolPort-020-099-632)
2-(3,6-dioxo-1,2,3,6-tetrahydropyridazin-1-yl)-N-[1-(3-oxo-3,4-dihydro-2H-1,4-benzoxazin-6-yl)ethyl]acetamide

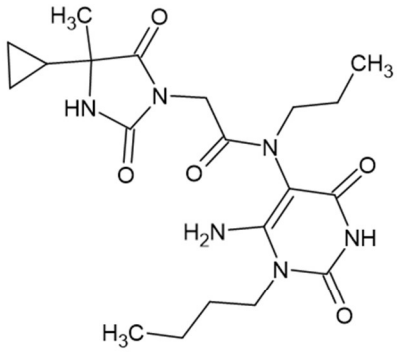

MP7 (MolPort-005-729-701)
N-(6-amino-1-butyl-2,4-dioxo-1,2,3,4-tetrahydropyrimidin-5-yl)-2-(4-cyclopropyl-4-methyl-2,5-dioxoimidazolidin-1-yl)-N-propylacetamide

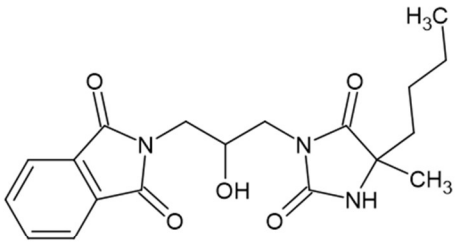

MP8 (MolPort-005-687-811)
2-[3-(4-butyl-4-methyl-2,5-dioxoimidazolidin-1-yl)-2-hydroxypropyl]-2,3-dihydro-1H-isoindole-1,3-dione

Figure 50: Chemical structures of MP5-8

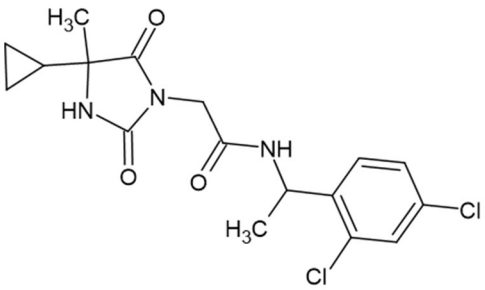

MP9 (MolPort-004-073-151)
2-(4-cyclopropyl-4-methyl-2,5-dioxoimidazolidin-1-yl)-N-[1-(2,4-dichlorophenyl)ethyl]acetamide

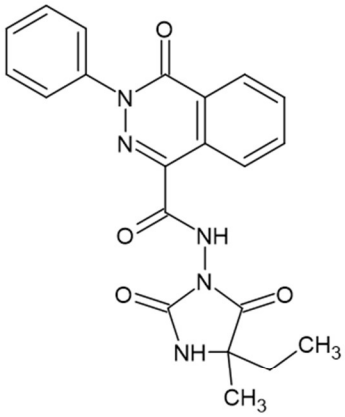

MP10 (MolPort-004-122-953)
N-(4-ethyl-4-methyl-2,5-dioxoimidazolidin-1-yl)-4-oxo-3-phenyl-3,4-dihydrophthalazine-1-carboxamide

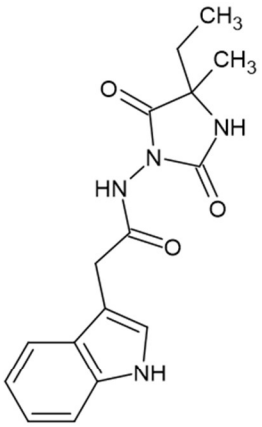

MP11 (MolPort-004-236-511)
N-(4-ethyl-4-methyl-2,5-dioxoimidazolidin-1-yl)-2-(1H-indol-3-yl)acetamide

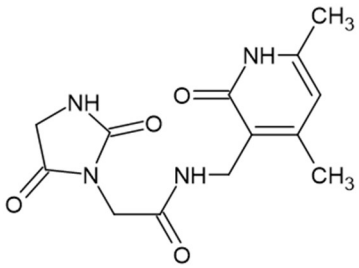

MP12 (MolPort-023-132-634)
N-[(4,6-dimethyl-2-oxo-1,2-dihydropyridin-3-yl)methyl]-2-(2,5-dioxoimidazolidin-1-yl)acetamide

Figure 51: Chemical structures of MP9-12

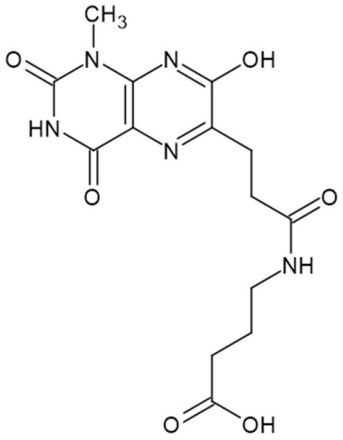

MP13 (MolPort-039-308-883)
4-[3-(7-hydroxy-1-methyl-2,4-dioxo-1,2,3,4-tetrahydropteridin-6-yl)propanamido]butanoic acid

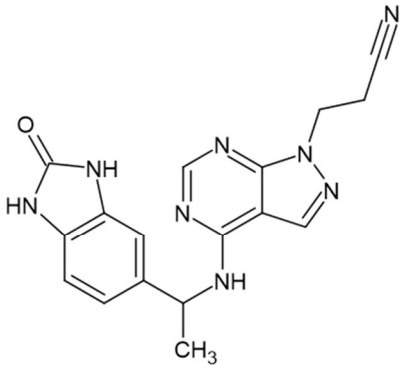

MP14 (MolPort-030-003-656)
3-(4-{[1-(2-oxo-2,3-dihydro-1H-1,3-benzodiazol-5-yl)ethyl]amino}-1H-pyrazolo[3,4-d]pyrimidin-1-yl)propanenitrile

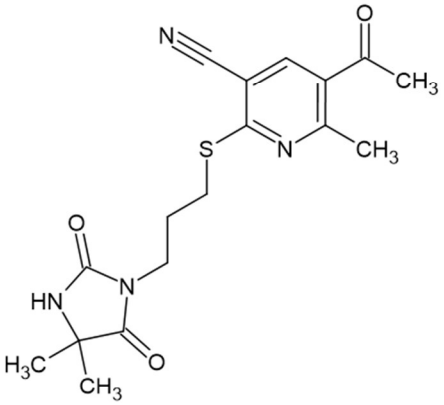

MP15 (MolPort-009-303-471)
5-acetyl-2-{[3-(4,4-dimethyl-2,5-dioxoimidazolidin-1-yl)propyl]sulfanyl}-6-methylpyridine-3-carbonitrile

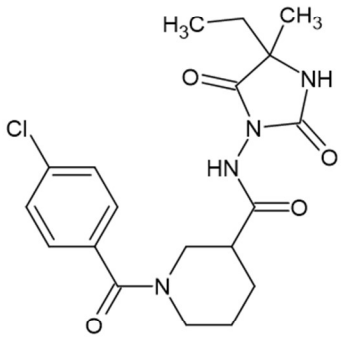

MP16 (MolPort-004-233-604)
1-(4-chlorobenzoyl)-N-(4-ethyl-4-methyl-2,5-dioxoimidazolidin-1-yl)piperidine-3-carboxamide

Figure 52: Chemical structures of MP13-16

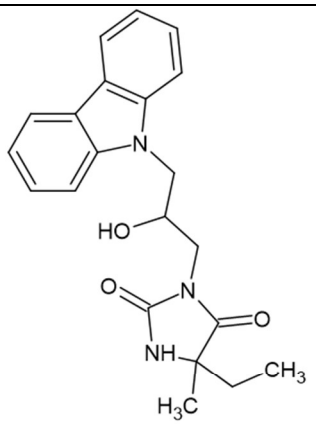

MP17 (MolPort-009-627-566)
3-[3-(9H-carbazol-9-yl)-2-hydroxypropyl]-5-ethyl-5-methylimidazolidine-2,4-dione

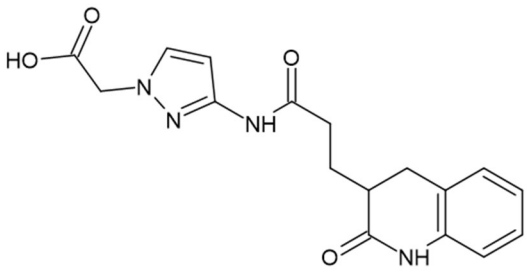

MP18 (MolPort-039-236-162)
2-{3-[3-(2-oxo-1,2,3,4-tetrahydroquinolin-3-yl)propanamido]-1H-pyrazol-1-yl}acetic acid

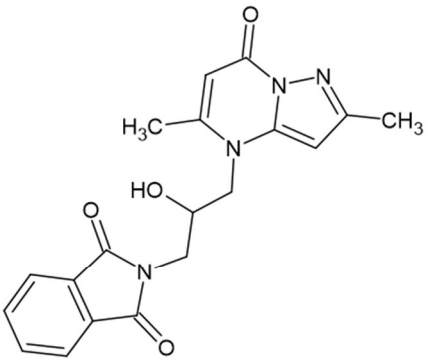

MP19 (MolPort-009-256-864)
2-(3-{2,5-dimethyl-7-oxo-4H,7H-pyrazolo[1,5-a]pyrimidin-4-yl}-2-hydroxypropyl)-2,3-dihydro-1H-isoindole-1,3-dione

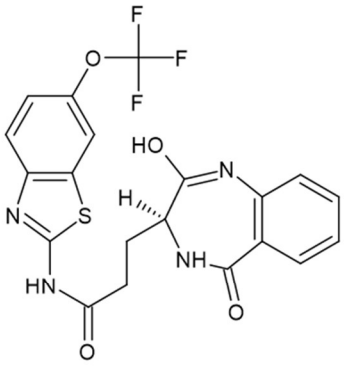

MP20 (MolPort-008-340-059)
3-[(3S)-2-hydroxy-5-oxo-4,5-dihydro-3H-1,4-benzodiazepin-3-yl]-N-[6-(trifluoromethoxy)-1,3-benzothiazol-2-yl]propanamide

Figure 53: Chemical structures of MP17-20

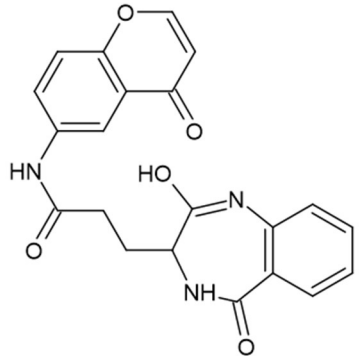

MP21 (MolPort-038-430-201)
3-(2-hydroxy-5-oxo-4,5-dihydro-3H-1,4-benzodiazepin-3-yl)-N-(4-oxo-4H-chromen-6-yl)propanamide

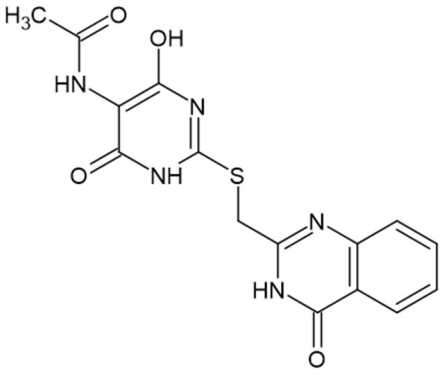

MP22 (MolPort-002-731-464)
N-(4-hydroxy-6-oxo-2-{[(4-oxo-3,4-dihydroquinazolin-2-yl)methyl]sulfanyl}-1,6-dihydropyrimidin-5-yl)acetamide

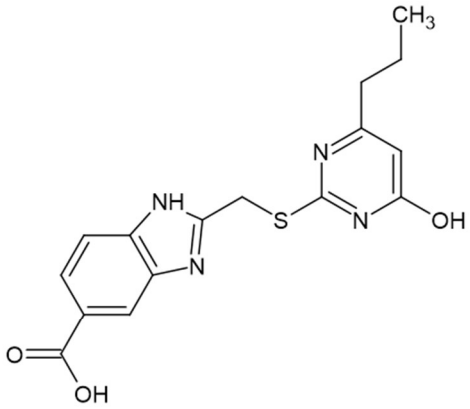

MP23 (MolPort-005-988-009)
2-{[(4-hydroxy-6-propylpyrimidin-2-yl)sulfanyl]methyl}-1H-1,3-benzodiazole-5-carboxylic acid

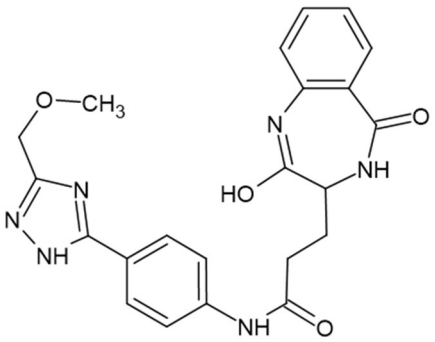

MP24 (MolPort-029-999-514)
3-(2-hydroxy-5-oxo-4,5-dihydro-3H-1,4-benzodiazepin-3-yl)-N-{4-[3-(methoxymethyl)-1H-1,2,4-triazol-5-yl]phenyl}propanamide

Figure 54: Chemical structures of MP21-24

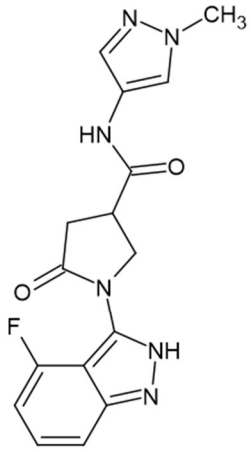

MP25 (MolPort-027-847-524)
1-(4-fluoro-2H-indazol-3-yl)-N-(1-methyl-1H-pyrazol-4-yl)-5-oxopyrrolidine-3-carboxamide

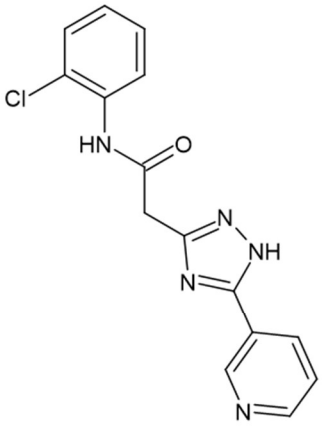

MP26 (MolPort-008-334-081)
N-(2-chlorophenyl)-2-[5-(pyridin-3-yl)-1H-1,2,4-triazol-3-yl]acetamide

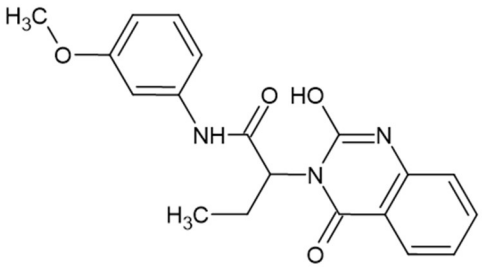

MP27 (MolPort-000-814-721)
2-(2-hydroxy-4-oxo-3,4-dihydroquinazolin-3-yl)-N-(3-methoxyphenyl)butanamide

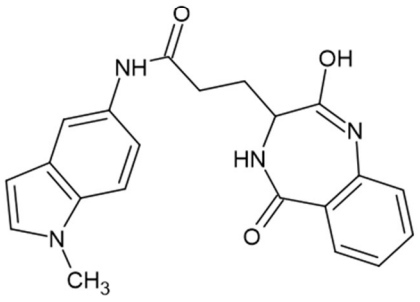

MP28 (MolPort-046-597-216)
3-(2-hydroxy-5-oxo-4,5-dihydro-3H-1,4-benzodiazepin-3-yl)-N-(1-methyl-1H-indol-5-yl)propanamide

Figure 55: Chemical structures of MP25-28

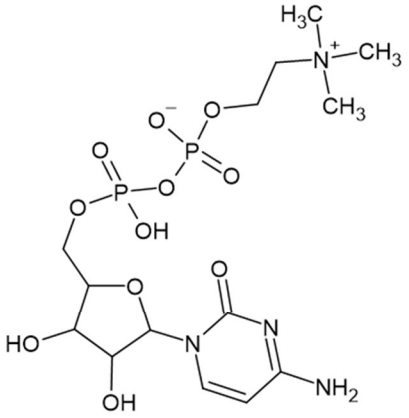

CDP-choline
[[5-(4-amino-2-oxopyrimidin-1-yl)-3,4-dihydroxyoxolan-2-yl]methoxy-hydroxyphosphoryl] 2-(trimethylazaniumyl)ethyl phosphate

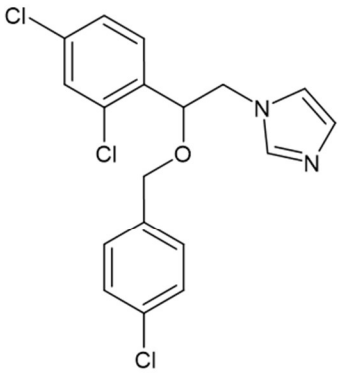

Econazole
1-[2-[(4-chlorophenyl)methoxy]-2-(2,4-dichlorophenyl)ethyl]imidazole

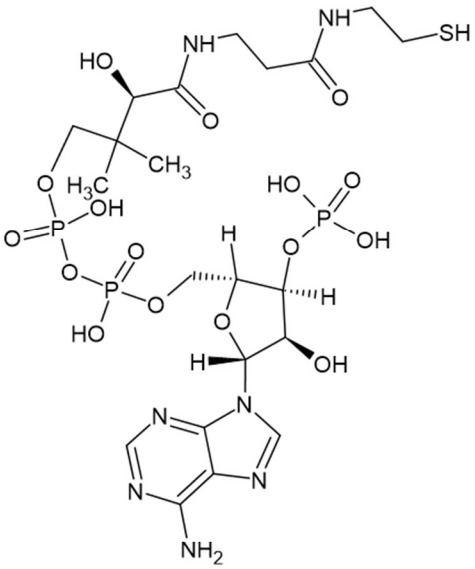

Coenyzme A
[[(2R,3S,4R,5R)-5-(6-aminopurin-9-yl)-4-hydroxy-3-phosphonooxyoxolan-2-yl]methoxy-hydroxyphosphoryl] [(3R)-3-hydroxy-2,2-dimethyl-4-oxo-4-[[3-oxo-3-(2-sulfanylethylamino)propyl]amino]butyl] hydrogen phosphate

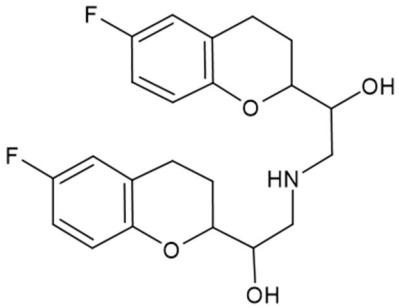

Nebivolol
1-(6-fluoro-3,4-dihydro-2H-chromen-2-yl)-2-[[2-(6-fluoro-3,4-dihydro-2H-chromen-2-yl)-2-hydroxyethyl]amino]ethanol

Figure 56: Chemical structures of CDP-choline, econazole, coenzyme A and nebivolol

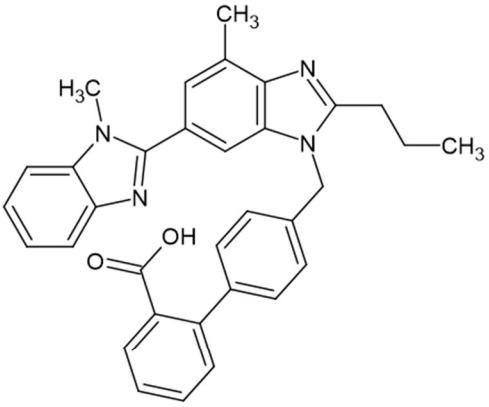

Telmisartan
2-[4-[[4-methyl-6-(1-methylbenzimidazol-2-yl)-2-propylbenzimidazol-1-yl]methyl]phenyl]benzoic acid

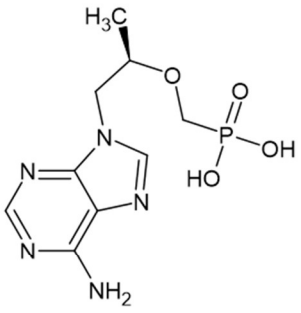

Tenofovir
[(2R)-1-(6-aminopurin-9-yl)propan-2-yl]oxymethylphosphonic acid

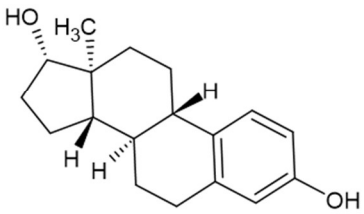

β-Estradiol
(8R,9S,13S,14S,17S)-13-methyl-6,7,8,9,11,12,14,15,16,17-decahydrocyclopenta[a]phenanthrene-3,17-diol

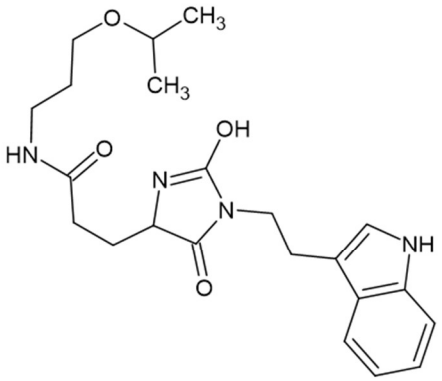

ZINC8765069
3-{(4S)-1-[2-(1H-indol-3-yl)ethyl]-2,5-dioxoimidazolidin-4-yl}-N-[3-(propan-2-yloxy)propyl]propanamide

Figure 57: Chemical structures of telmisartan, tenofovir, β-estradiol, ZINC8765069

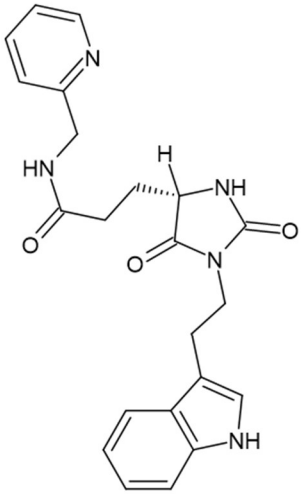

ZINC8792474
3-{(4S)-1-[2-(1H-indol-3-yl)ethyl]-2,5-dioxoimidazolidin-4-yl}-N-(pyridin-2-ylmethyl)propanamide

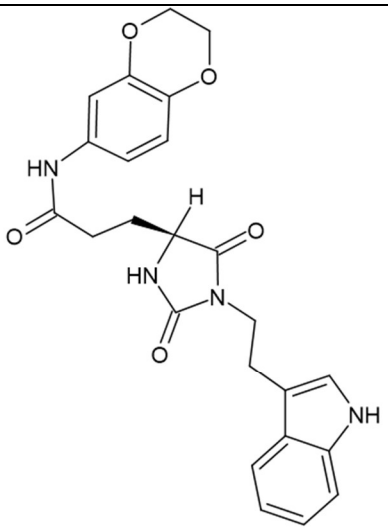

ZINC8879336
N-(2,3-dihydro-1,4-benzodioxin-6-yl)-3-[(4S)-1-[2-(1H-indol-3-yl)ethyl]-2,5-dioxoimidazolidin-4-yl]propanamide

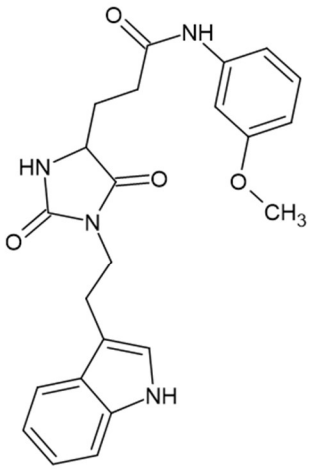

ZINC8879971
3-[(4S)-1-[2-(1H-indol-3-yl)ethyl]-2,5-dioxoimidazolidin-4-yl]-N-(3-methoxyphenyl)propanamide

Figure 58: Chemical structures of ZINC8792474, ZINC8879336, ZINC8879971

8.2 Safety and disposal

Every chemical used during the experimental work for this thesis was handled and disposed of in accordance with GHS safety and precautionary instructions. Contaminated waste and solvents were stored in designated containers and disposed in accordance with the safety instructions. Genetically modified organisms and associated liquid and solid waste were were inactivated in accordance with the the "Deutsches Gentechnikgesetz". All experiments for this work with genetically modified organisms were carried out according to the applicable safety procedures by law. All hazardous and toxic chemicals used in this study are listed in Table 17 with their GHS hazard symbol, hazard statements and precautionary information.

Table 17: Hazardous and toxic chemicals and materials

Name	CAS Number	GHS Hazard	Hazard statements	Precautinary statements
5 mL His Trap FF IMAC column	/	GHS02	H226	P210, P235, P241, P280, P303 + P361 + P353, P501
Acetophenon	98-86-2	GHS07	H302, H319	P264, P264 + P265, P270, P280, P301 + P317, P305 + P351 + P338, P330, P337, P501
ADPR	68414-18-6	GHS07	H315, H319, H335	P261, P264, P271, P280, P302 + P352, P305 + P351 + P338
α-NAD	7298-93-3	GHS07	H315, H319, H335	P261, P264, P271, P280, P302 + P352, P305 + P351 + P338
β-Estradiol	50-28-2	GHS08, GHS09	H350, H351, H360, H360FD, H362, H372, H400, H410	P203, P260, P263, P264, P270, P273, P280, P318, P319, P391, P405, and P501

Table 17 (continued)

Name	CAS Number	GHS Hazard	Hazard statements	Precautinary statements
CDP-choline	987-78-0	GHS07	H315, H319, H335	P261, P264, P264+P265, P271, P280, P302+P352, P304+P340, P305+P351+P338, P319, P321, P332+P317, P337+P317, P362+P364, P403+P233, P405, P501
Chloramphenicol	56-75-7	GHS05, GHS08	H317, H318, H350, H351, H360, H361	P203, P261, P264 + P265, P272, P280, P302 + P352, P305 + P354 + P338, P317, P318, P321, P333 + P317, P362 + P364, P405, P501
cOmplete EDTA-free protease inhibitor	/	GHS05	H314	P260, P280, P301 + P330 + P331, P303 + P 361 + P353, P304 + P340 + P310, P305 +P351 + P338 +P310
Coomassie staining solution	6104-58-1	GHS05, GHS08	H314, H370	P303 + P361 + P353, P305 + P351 + P338, P301 + P330 + P331, P501, P280
DL-Dithiothreitol (DTT)	3583-12-3	GHS05, GHS07	H302, H315, H318	P264, P280, P301 + P312, P302 + P352, P305 + P351 + P338, P332 + P313
Econazole	27220-47-9	GHS07	H302	P301 + P312 + P330
Ethanol	64-17-5	GHS02, GHS07	H225, H319	P210, P223, P240, P241, P242, P305 + P351 + P338

Table 17 (continued)

Name	CAS Number	GHS Hazard	Hazard statements	Precautinary statements
$FeCl_3$	7705-08-0	GHS05, GHS07	H290, H302, H315, H318	P234, P264, P280, P301 + P312, P302 + P352, P305 + P351 + P338
Formic acid	64-18-6	GHS02, GHS05, GHS06	H226, H302, H314, H331	P210, P280, P301 + P312, P303 + P361 + P353, P304 + P340 + P310, P305 + P351 + P338
Gluthatione sepharose 4B	/	GHS02	H226	P210, P235, P241, P280, P303 + P361 + P353, P501
HCl	7647-01-0	GHS05, GHS07	H290, H314, H335	P234, P261, P271, P280, P303 + P361 + P353, P305 + P351 + P338
Imidazole	288-32-4	GHS05, GHS07, GHS08	H302, H314, H360D	P260, P280, P301 + P312, P303 + P361 + P353, P304 + P340 + P310, P305 + P351 + P338
Kanamycin	25389-94-0	GHS08	H360D	P201, P202, P280, P308 + P313, P405, P501
KOH	1310-58-3	GHS05, GHS07	H290, H302, H314	P234, P260, P280, P301 + P312, P303 + P361 + P353, P305 + P351 + P338
Methanol	67-56-1	GHS02, GHS06, GHS08	H225, H301, H311, H331, H370	P210, P233, P280, P301 + P310, P303 + P361 + P353, P304+ P340+P311
NaOH	1310-73-2	GHS05	H290, H314	P234, P260, P280, P303 + P361 + P353, P304 + P340 + P310, P305 + P351 + P338

Table 17 (continued)

Name	CAS Number	GHS Hazard	Hazard statements	Precautinary statements
Nebivolol	152520-56-4	GHS07, GHS08, GHS09	H302, H361d, H400, H410, H413	P203, P264, P273, P280, P301+P317, P318, P330, P391, P405, P501
Penicillin-Streptomycin solution	/	GHS07, GHS08	H302 + H332, H317, H334, H361d	P201, P261, P264, P280, P304 + P340 + P312,P308+P313
Pyruvate solution	113-24-6	GHS07	H317, H319	P261, P264, P272, P280, P302 + P352, P305 + P351 + P338
Sodium dodecyl sulfate (SDS)	151-21-3	GHS05, GHS07	H302, H315, H318, H412	P264, P273, P280, P301, P312, P302 + P352, P305 + P351 + P338
Superdex 75 Increase 10/300 GL	/	GHS02	H226	P210, P235, P241, P280, P303 + P361 + P353, P501
Telmisartan	144701-48-4	GHS08, GHS09	H361, H441	P203, P273, P280, P318, P391, P405, P501
Tenofovir	147127-20-6	GHS05	H318	P264 + P265, P280, P305 + P354 + P338, P317
TFMU	575-03-1	GHS07	H315, H319	P264, P280, P337 + P313, P305 + P351 + P338, P 302 + P352, P332 + P352, P332 + P313, P331
Triton X-100	92046-34-9	GHS07, GHS09	H315, H319, H335, H411	P261, P264, P271, P273, P302 + P352, P305 + P351 + P338
Trypan blue	72-57-1	GHS08	H350	P201, P202, P280, P308 + P313, P405, P501

Literature

Abola, J. & Sundaralingam M. (1973). Refinement of the crystal structure of tubercidin. Acta Crystallogr. B Struct. Crystallogr. Cryst. Chem.29:697-703.

Acker, M & Auld, D. (2014). Considerations for the design and reporting of enzyme assays in high-throughput screening applications. Perspectives in Science. 1. 56–73. 10.1016/j.pisc.2013.12.001.

Alhammad, Y. M. O., & Fehr, A. R. (2020). The Viral Macrodomain Counters Host Antiviral ADP-Ribosylation. Viruses, 12(4), 384. https://doi.org/10.3390/v12040384

Alhammad, Y. M. O., Kashipathy, M. M., Roy, A., Gagné, J. P., McDonald, P., Gao, P., Nonfoux, L., Battaile, K. P., Johnson, D. K., Holmstrom, E. D., Poirier, G. G., Lovell, S., & Fehr, A. R. (2021). The SARS-CoV-2 Conserved Macrodomain Is a Mono-ADP-Ribosylhydrolase. Journal of virology, 95(3), e01969-20. https://doi.org/10.1128/JVI.01969-20

Alhammad, Y. M., Parthasarathy, S., Ghimire, R., Kerr, C. M., O'Connor, J. J., Pfannenstiel, J. J., Chanda, D., Miller, C. A., Baumlin, N., Salathe, M., Unckless, R. L., Zuñiga, S., Enjuanes, L., More, S., Channappanavar, R., & Fehr, A. R. (2023). SARS-CoV-2 Mac1 is required for IFN antagonism and efficient virus replication in cell culture and in mice. Proceedings of the National Academy of Sciences of the United States of America, 120(35), e2302083120. https://doi.org/10.1073/pnas.2302083120

Barkauskaite, E., Jankevicius, G., & Ahel, I. (2015). Structures and Mechanisms of Enzymes Employed in the Synthesis and Degradation of PARP-Dependent Protein ADP-Ribosylation. Molecular cell, 58(6), 935–946. https://doi.org/10.1016/j.molcel.2015.05.007

Barua, S., Kaltenboeck, B., Juan, Y. C., Bird, R. C., & Wang, C. (2023). Comparative Evaluation of GS-441524, Teriflunomide, Ruxolitinib, Molnupiravir, Ritonavir, and Nirmatrelvir for In Vitro Antiviral Activity against Feline Infectious Peritonitis Virus. Veterinary sciences, 10(8), 513. https://doi.org/10.3390/vetsci10080513

Baszczyňski, O., Watt, J.,Rozewitz, M., Guse, A.,Fliegert R., Potter, B. (2019) Synthesis of Terminal Ribose Analogues of Adenosine 5'-Diphosphate Ribose as Probes for the Transient Receptor Potential Cation Channel TRPM2. J. Org. Chem. 84, 6143-6157

Baszczyňski, O., Watt, J.,Rozewitz, M., Fliegert R., Guse, A., Potter, B. (2020) Synthesis of phosphonoacetate analogues of the second messenger adenosine 5'-diphosphate ribose (ADPR).RSC Adv. 10, 1776-1785

Berkowitz, D. B., Bose, M., Pfannenstiel, T. J., & Doukov, T. (2000). alpha-fluorinated phosphonates as substrate mimics for glucose 6-phosphate dehydrogenase: the CHF stereochemistry matters. The Journal of organic chemistry, 65(15), 4498–4508. https://doi.org/10.1021/jo000220v

Blanco-Melo, D., Nilsson-Payant, B. E., Liu, W. C., Uhl, S., Hoagland, D., Møller, R., Jordan, T. X., Oishi, K., Panis, M., Sachs, D., Wang, T. T., Schwartz, R. E., Lim, J. K., Albrecht, R. A., & tenOever, B. R. (2020). Imbalanced Host Response to SARS-CoV-2 Drives Development of COVID-19. Cell, 181(5), 1036–1045.e9. https://doi.org/10.1016/j.cell.2020.04.026

Busnadiego, I., Fernbach, S., Pohl, M. O., Karakus, U., Huber, M., Trkola, A., Stertz, S., & Hale, B. G. (2020). Antiviral Activity of Type I, II, and III Interferons Counterbalances ACE2 Inducibility and Restricts SARS-CoV-2. mBio, 11(5), e01928-20. https://doi.org/10.1128/mBio.01928-20

Callaway E. (2021). Beyond Omicron: what's next for COVID's viral evolution. Nature, 600(7888), 204–207. https://doi.org/10.1038/d41586-021-03619-8

Chea, C., Lee, D. Y., Kato, J., Ishiwata-Endo, H., & Moss, J. (2023). Macrodomain Mac1 of SARS-CoV-2 Nonstructural Protein 3 Hydrolyzes Diverse ADP-ribosylated Substrates. bioRxiv : the preprint server for biology, 2023.02.07.527501. https://doi.org/10.1101/2023.02.07.527501

Cho, E., Rosa, M., Anjum, R., Mehmood, S., Soban, M., Mujtaba, M., Bux, K., Moin, S. T., Tanweer, M., Dantu, S., Pandini, A., Yin, J., Ma, H., Ramanathan, A., Islam, B., Mey, A. S. J. S., Bhowmik, D., & Haider, S. (2021). Dynamic Profiling of β-Coronavirus 3CL Mpro Protease Ligand-Binding Sites. Journal of chemical information and modeling, 61(6), 3058–3073. https://doi.org/10.1021/acs.jcim.1c00449

Correy, G. J., Kneller, D. W., Phillips, G., Pant, S., Russi, S., Cohen, A. E., Meigs, G., Holton, J. M., Gahbauer, S., Thompson, M. C., Ashworth, A., Coates, L., Kovalevsky, A., Meilleur, F., & Fraser, J. S. (2022). The mechanisms of catalysis and ligand binding for the SARS-CoV-2 NSP3 macrodomain from neutron and x-ray diffraction at room temperature. Science advances, 8(21), eabo5083. https://doi.org/10.1126/sciadv.abo5083

Dasovich, M., Zhuo, J., Goodman, J. A., Thomas, A., McPherson, R. L., Jayabalan, A. K., Busa, V. F., Cheng, S. J., Murphy, B. A., Redinger, K. R., Alhammad, Y. M. O., Fehr, A. R., Tsukamoto, T., Slusher, B. S., Bosch, J., Wei, H., & Leung, A. K. L. (2022). High-Throughput Activity Assay for Screening Inhibitors of the SARS-CoV-2 Mac1 Macrodomain. ACS chemical biology, 17(1), 17–23. https://doi.org/10.1021/acschembio.1c00721

Denessiouk, K. A., & Johnson, M. S. (2003). "Acceptor-donor-acceptor" motifs recognize the Watson-Crick, Hoogsteen and Sugar "donor-acceptor-donor" edges of adenine and adenosine-containing ligands. Journal of molecular biology, 333(5), 1025–1043. https://doi.org/10.1016/j.jmb.2003.09.017

Drown, B. S., Shirai, T., Rack, J. G. M., Ahel, I., & Hergenrother, P. J. (2018). Monitoring Poly(ADP-ribosyl)glycohydrolase Activity with a Continuous Fluorescent Substrate. Cell chemical biology, 25(12), 1562–1570.e19. https://doi.org/10.1016/j.chembiol.2018.09.008

Elliott, T. S., Slowey, A., Yeb, Y., Conway, S. J. (2012) The use of phosphate bioisosteres in medicinal chemistry and chemical biology. Med. Chem. Commun., 3, 735-751. https://doi.org/10.1039/C2MD20079A

Evich, M., Spring-Connell, A. & Germann, M. (2017). Impact of modified ribose sugars on nucleic acid conformation and function. Heterocyclic Communications, 23(3), 155-165. https://doi.org/10.1515/hc-2017-0056

Fehr, A. R., Channappanavar, R., Jankevicius, G., Fett, C., Zhao, J., Athmer, J., Meyerholz, D. K., Ahel, I., & Perlman, S. (2016). The Conserved Coronavirus Macrodomain Promotes Virulence and Suppresses the Innate Immune Response during Severe Acute Respiratory Syndrome Coronavirus Infection. mBio, 7(6), e01721-16. https://doi.org/10.1128/mBio.01721-16

Fehr, A. R., Singh, S. A., Kerr, C. M., Mukai, S., Higashi, H., & Aikawa, M. (2020). The impact of PARPs and ADP-ribosylation on inflammation and host-pathogen interactions. Genes & development, 34(5-6), 341–359. https://doi.org/10.1101/gad.334425.119

Feijs, K. L. H., & Žaja, R. (2022). Are PARPs promiscuous?. Bioscience reports, 42(5), BSR20212489. https://doi.org/10.1042/BSR20212489

Fliegert, R., Watt, J. M., Schöbel, A., Rozewitz, M. D., Moreau, C., Kirchberger, T., Thomas, M. P., Sick, W., Araujo, A. C., Harneit, A., Potter, B. V. L., Guse, A. H. (2017) Ligand-induced activation of human TRPM2 requires the terminal ribose of ADPR and involves Arg1433 and Tyr1349. Biochem. J. 474, 2159–2175

Flynn, J. M., Samant, N., Schneider-Nachum, G., Barkan, D. T., Yilmaz, N. K., Schiffer, C. A., Moquin, S. A., Dovala, D., & Bolon, D. N. A. (2022). Comprehensive fitness landscape of SARS-CoV-2 Mpro reveals insights into viral resistance mechanisms. eLife, 11, e77433. https://doi.org/10.7554/eLife.77433

Frey, P. A., & Sammons, R. D. (1985). Bond order and charge localization in nucleoside phosphorothioates. Science (New York, N.Y.), 228(4699), 541–545. https://doi.org/10.1126/science.2984773

Frick, D. N., Virdi, R. S., Vuksanovic, N., Dahal, N., & Silvaggi, N. R. (2020). Molecular Basis for ADP-Ribose Binding to the Mac1 Domain of SARS-CoV-2 nsp3. Biochemistry, 59(28), 2608–2615. https://doi.org/10.1021/acs.biochem.0c00309

Fu, W., Yao, H., Bütepage, M., Zhao, Q., Lüscher, B., & Li, J. (2021). The search for inhibitors of macrodomains for targeting the readers and erasers of

mono-ADP-ribosylation. Drug discovery today, 26(11), 2547–2558. https://doi.org/10.1016/j.drudis.2021.05.007

Gahbauer, S., Correy, G. J., Schuller, M., Ferla, M. P., Doruk, Y. U., Rachman, M., Wu, T., Diolaiti, M., Wang, S., Neitz, R. J., Fearon, D., Radchenko, D. S., Moroz, Y. S., Irwin, J. J., Renslo, A. R., Taylor, J. C., Gestwicki, J. E., von Delft, F., Ashworth, A., Ahel, I., … Fraser, J. S. (2023). Iterative computational design and crystallographic screening identifies potent inhibitors targeting the Nsp3 macrodomain of SARS-CoV-2. Proceedings of the National Academy of Sciences of the United States of America, 120(2), e2212931120. https://doi.org/10.1073/pnas.2212931120

Gattkowski, E., Rutherford, T. J., Möckl, F., Bauche, A., Sander, S., Fliegert, R., & Tidow, H. (2021). Analysis of ligand binding and resulting conformational changes in pyrophosphatase NUDT9. The FEBS journal, 288(23), 6769–6782. https://doi.org/10.1111/febs.16097

Hadjadj, J., Yatim, N., Barnabei, L., Corneau, A., Boussier, J., Smith, N., Péré, H., Charbit, B., Bondet, V., Chenevier-Gobeaux, C., Breillat, P., Carlier, N., Gauzit, R., Morbieu, C., Pène, F., Marin, N., Roche, N., Szwebel, T. A., Merkling, S. H., Treluyer, J. M., … Terrier, B. (2020). Impaired type I interferon activity and inflammatory responses in severe COVID-19 patients. Science (New York, N.Y.), 369(6504), 718–724. https://doi.org/10.1126/science.abc6027

Harder, M., Schäfer, E., Kümin, T., Illarionov, B., Bacher, A., Fischer, M., Diederich, F. and Bernet, B. (2015), 8-Substituted, syn-Configured Adenosine Derivatives as Potential Inhibitors of the Enzyme IspE from the Non-Mevalonate Pathway of Isoprenoid Biosynthesis†. Eur. J. Org. Chem., 2015: 7276-7286. https://doi.org/10.1002/ejoc.201501150

Heer, C. D., Sanderson, D. J., Voth, L. S., Alhammad, Y. M. O., Schmidt, M. S., Trammell, S. A. J., Perlman, S., Cohen, M. S., Fehr, A. R., & Brenner, C. (2020). Coronavirus infection and PARP expression dysregulate the NAD metabolome: An actionable component of innate immunity. The Journal of biological chemistry, 295(52), 17986–17996. https://doi.org/10.1074/jbc.RA120.015138

Heyer, A., Günther, T., Robitaille, A., Lütgehetmann, M., Addo, M. M., Jarczak, D., Kluge, S., Aepfelbacher, M., Schulze Zur Wiesch, J., Fischer, N., & Grundhoff, A. (2022). Remdesivir-induced emergence of SARS-CoV2 variants in patients with prolonged infection. Cell reports. Medicine, 3(9), 100735. https://doi.org/10.1016/j.xcrm.2022.100735

Jankevicius, G., Hassler, M., Golia, B., Rybin, V., Zacharias, M., Timinszky, G., & Ladurner, A. G. (2013). A family of macrodomain proteins reverses cellular mono-ADP-ribosylation. Nature structural & molecular biology, 20(4), 508–514. https://doi.org/10.1038/nsmb.2523

Jensen, S., & Thomsen, A. R. (2012). Sensing of RNA viruses: a review of innate immune receptors involved in recognizing RNA virus invasion. Journal of virology, 86(6), 2900–2910. https://doi.org/10.1128/JVI.05738-11

Jhuti, D., Rawat, A., Guo, C. M., Wilson, L. A., Mills, E. J., & Forrest, J. I. (2022). Interferon Treatments for SARS-CoV-2: Challenges and Opportunities. Infectious diseases and therapy, 11(3), 953–972. https://doi.org/10.1007/s40121-022-00633-9

Karras, G. I., Kustatscher, G., Buhecha, H. R., Allen, M. D., Pugieux, C., Sait, F., Bycroft, M., & Ladurner, A. G. (2005). The macro domain is an ADP-ribose binding module. The EMBO journal, 24(11), 1911–1920. https://doi.org/10.1038/sj.emboj.7600664

Klimke, G., Cuno, I., Lüdemann, H.-D., Mengel, R. & Robins, M. (1979). Ribose Conformations of Adenosine Analogs Modified at the 2', 3' or 5' Positions. Z. Naturforsch. C. 34. 1075-1084. 10.1515/znc-1979-1201.

Kumler, W. D., & Eiler J. J. (1943). The Acid Strength of Mono and Diesters of Phosphoric Acid. The n-Alkyl Esters from Methyl to Butyl, the Esters of Biological Importance, and the Natural Guanidine Phosphoric Acids. J. Am. Chem. Soc, 65, 12, 2355–2361. https://doi.org/10.1021/ja01252a028

Lei, J., Kusov, Y., & Hilgenfeld, R. (2018). Nsp3 of coronaviruses: Structures and functions of a large multi-domain protein. Antiviral research, 149, 58–74. https://doi.org/10.1016/j.antiviral.2017.11.001

Lei, X., Dong, X., Ma, R., Wang, W., Xiao, X., Tian, Z., Wang, C., Wang, Y., Li, L., Ren, L., Guo, F., Zhao, Z., Zhou, Z., Xiang, Z., & Wang, J. (2020). Activation and evasion of type I interferon responses by SARS-CoV-2. Nature communications, 11(1), 3810. https://doi.org/10.1038/s41467-020-17665-9

Lokugamage, K. G., Hage, A., de Vries, M., Valero-Jimenez, A. M., Schindewolf, C., Dittmann, M., Rajsbaum, R., & Menachery, V. D. (2020). Type I Interferon Susceptibility Distinguishes SARS-CoV-2 from SARS-CoV. Journal of virology, 94(23), e01410-20. https://doi.org/10.1128/JVI.01410-20

Makarov, M. V., & Migaud, M. E. (2019). Syntheses and chemical properties of β-nicotinamide riboside and its analogues and derivatives. Beilstein journal of organic chemistry, 15, 401–430. https://doi.org/10.3762/bjoc.15.36

Meier C. (2017). Nucleoside diphosphate and triphosphate prodrugs - An unsolvable task?. Antiviral chemistry & chemotherapy, 25(3), 69–82. https://doi.org/10.1177/2040206617738656

Michalska, K., Kim, Y., Jedrzejczak, R., Maltseva, N. I., Stols, L., Endres, M., & Joachimiak, A. (2020). Crystal structures of SARS-CoV-2 ADP-ribose phosphatase: from the apo form to ligand complexes. IUCrJ, 7(Pt 5), 814–824. https://doi.org/10.1107/S2052252520009653

Mihalič, F., Benz, C., Kassa, E., Lindqvist, R., Simonetti, L., Inturi, R., Aronsson, H., Andersson, E., Chi, C. N., Davey, N. E., Överby, A. K., Jemth, P., & Ivarsson, Y. (2023). Identification of motif-based interactions between SARS-CoV-2 protein domains and human peptide ligands pinpoint antiviral targets. Nature communications, 14(1), 5636. https://doi.org/10.1038/s41467-023-41312-8

Min, K. A., Rosania, G. R., Kim, C. K., & Shin, M. C. (2016). Functional and cytometric examination of different human lung epithelial cell types as drug transport barriers. Archives of pharmacal research, 39(3), 359–369. https://doi.org/10.1007/s12272-015-0704-6

Moreau, C., Kirchberger, T., Swarbrick, J. M., Bartlett, S. J., Fliegert, R., Yorgan, T., Bauche, A., Harneit, A., Guse, A. H., Potter, B. V. L. (2013) Structure-activity relationship of adenosine 5'-diphosphoribose at the transient receptor potential melastatin 2 (TRPM2) channel: rational design of antagonists. J. Med. Chem. 56, 10079–102

Nakamura, H. & Tamura, Z. (1978). Fluorometric assay of alpha-methylene carbonyl compounds with N1-methylnicotinamide chloride. Analytical Chemistry, 50(14), 2047-2051. https://pubs.acs.org/doi/pdf/10.1021/ac50036a027

Ni, X., Schröder, M., Olieric, V., Sharpe, M. E., Hernandez-Olmos, V., Proschak, E., Merk, D., Knapp, S., & Chaikuad, A. (2021). Structural Insights into Plasticity and Discovery of Remdesivir Metabolite GS-441524 Binding in SARS-CoV-2 Macrodomain. ACS medicinal chemistry letters, 12(4), 603–609. https://doi.org/10.1021/acsmedchemlett.0c00684

Ocenas, M. (2022). Impact of derivatives of adenosine 5'-diphosphoribose (ADPR) on the enzymatic activity of MacroD1 and MacroD2. Masterthesis (MSc.). University of Hamburg

O'Connor, J. J., Ferraris, D., & Fehr, A. R. (2023). An Update on the Current State of SARS-CoV-2 Mac1 Inhibitors. Pathogens (Basel, Switzerland), 12(10), 1221. https://doi.org/10.3390/pathogens12101221

Okumura, H., Kitazawa, N., Wada, S., & Hotta, H. (2011). Stability of sucrose fatty acid esters under acidic and basic conditions. Journal of oleo science, 60(6), 313–320. https://doi.org/10.5650/jos.60.313

Padhi, A. K., & Tripathi, T. (2021). Targeted design of drug binding sites in the main protease of SARS-CoV-2 reveals potential signatures of adaptation. Biochemical and biophysical research communications, 555, 147–153. https://doi.org/10.1016/j.bbrc.2021.03.118

Palazzo, L., Thomas, B., Jemth, A. S., Colby, T., Leidecker, O., Feijs, K. L., Zaja, R., Loseva, O., Puigvert, J. C., Matic, I., Helleday, T., & Ahel, I. (2015). Processing of protein ADP-ribosylation by Nudix hydrolases. The Biochemical journal, 468(2), 293–301. https://doi.org/10.1042/BJ20141554

Perlman S. (2020). Another Decade, Another Coronavirus. The New England journal of medicine, 382(8), 760–762. https://doi.org/10.1056/NEJMe2001126

Pires, D. E., Ascher, D. B., & Blundell, T. L. (2014). DUET: a server for predicting effects of mutations on protein stability using an integrated computational approach. Nucleic acids research, 42(Web Server issue), W314–W319. https://doi.org/10.1093/nar/gku411

Rack, J. G. M., Palazzo, L., & Ahel, I. (2020a). (ADP-ribosyl)hydrolases: structure, function, and biology. Genes & development, 34(5-6), 263–284. https://doi.org/10.1101/gad.334631.119

Rack, J. G. M., Zorzini, V., Zhu, Z., Schuller, M., Ahel, D., & Ahel, I. (2020b). Viral macrodomains: a structural and evolutionary assessment of the pharmacological potential. Open biology, 10(11), 200237. https://doi.org/10.1098/rsob.200237

Rasmussen, H. B., Jürgens, G., Thomsen, R., Taboureau, O., Zeth, K., Hansen, P. E., & Hansen, P. R. (2021). Cellular Uptake and Intracellular Phosphorylation of GS-441524: Implications for Its Effectiveness against COVID-19. Viruses, 13(7), 1369. https://doi.org/10.3390/v13071369

Roy, A., Alhammad, Y. M., McDonald, P., Johnson, D. K., Zhuo, J., Wazir, S., Ferraris, D., Lehtiö, L., Leung, A. K. L., & Fehr, A. R. (2022). Discovery of compounds that inhibit SARS-CoV-2 Mac1-ADP-ribose binding by high-throughput screening. Antiviral research, 203, 105344. https://doi.org/10.1016/j.antiviral.2022.105344

Russo, L. C., Tomasin, R., Matos, I. A., Manucci, A. C., Sowa, S. T., Dale, K., Caldecott, K. W., Lehtiö, L., Schechtman, D., Meotti, F. C., Bruni-Cardoso, A., & Hoch, N. C. (2021). The SARS-CoV-2 Nsp3 macrodomain reverses PARP9/DTX3L-dependent ADP-ribosylation induced by interferon signaling. The Journal of biological chemistry, 297(3), 101041. https://doi.org/10.1016/j.jbc.2021.101041

Sander, S., Pick, J., Gattkowski, E., Fliegert, R., & Tidow, H. (2022). The crystal structure of TRPM2 MHR1/2 domain reveals a conserved Zn2+ -binding domain essential for structural integrity and channel activity. Protein science : a publication of the Protein Society, 31(6), e4320. https://doi.org/10.1002/pro.4320

Schuller, M., Correy, G. J., Gahbauer, S., Fearon, D., Wu, T., Díaz, R. E., Young, I. D., Carvalho Martins, L., Smith, D. H., Schulze-Gahmen, U., Owens, T. W., Deshpande, I., Merz, G. E., Thwin, A. C., Biel, J. T., Peters, J. K., Moritz, M., Herrera, N., Kratochvil, H. T., QCRG Structural Biology Consortium, … Ahel, I. (2021). Fragment binding to the Nsp3 macrodomain of SARS-CoV-2 identified through crystallographic screening and computational docking. Science advances, 7(16), eabf8711. https://doi.org/10.1126/sciadv.abf8711

Sedlackova, L., & Korolchuk, V. I. (2020). The crosstalk of NAD, ROS and autophagy in cellular health and ageing. Biogerontology, 21(3), 381–397. https://doi.org/10.1007/s10522-020-09864-0

Selvaraj, C., Dinesh, D. C., Panwar, U., Boura, E., & Singh, S. K. (2021). High-Throughput Screening and Quantum Mechanics for Identifying Potent Inhibitors Against Mac1 Domain of SARS-CoV-2 Nsp3. IEEE/ACM transactions on computational biology and bioinformatics, 18(4), 1262–1270. https://doi.org/10.1109/TCBB.2020.3037136

Service R. F. (2022). Bad news for Paxlovid? Resistance may be coming. Science (New York, N.Y.), 377(6602), 138–139. https://doi.org/10.1126/science.add8037

Sowa, S. T., Galera-Prat, A., Wazir, S., Alanen, H. I., Maksimainen, M. M., & Lehtiö, L. (2021). A molecular toolbox for ADP-ribosyl binding proteins. Cell reports methods, 1(8), 100121. https://doi.org/10.1016/j.crmeth.2021.100121

Sposito, B., Broggi, A., Pandolfi, L., Crotta, S., Clementi, N., Ferrarese, R., Sisti, S., Criscuolo, E., Spreafico, R., Long, J. M., Ambrosi, A., Liu, E., Frangipane, V., Saracino, L., Bozzini, S., Marongiu, L., Facchini, F. A., Bottazzi, A., Fossali, T., Colombo, R., (…) Zanoni, I. (2021). The interferon landscape along the respiratory tract impacts the severity of COVID-19. Cell, 184(19), 4953–4968.e16. https://doi.org/10.1016/j.cell.2021.08.016

Stevens, L. A., Kato, J., Kasamatsu, A., Oda, H., Lee, D. Y., & Moss, J. (2019). The ARH and Macrodomain Families of α-ADP-ribose-acceptor Hydrolases Catalyze α-NAD+ Hydrolysis. ACS chemical biology, 14(12), 2576–2584. https://doi.org/10.1021/acschembio.9b00429

Studier F. W. (2005). Protein production by auto-induction in high density shaking cultures. Protein expression and purification, 41(1), 207–234. https://doi.org/10.1016/j.pep.2005.01.016

Suskiewicz, M. J., Prokhorova, E., Rack, J. G. M., & Ahel, I. (2023). ADP-ribosylation from molecular mechanisms to therapeutic implications. Cell, 186(21), 4475–4495. https://doi.org/10.1016/j.cell.2023.08.030

Suydam, I. T., & Strobel, S. A. (2008). Fluorine substituted adenosines as probes of nucleobase protonation in functional RNAs. Journal of the American Chemical Society, 130(41), 13639–13648. https://doi.org/10.1021/ja803336y

Taha, T. Y., Suryawanshi, R. K., Chen, I. P., Correy, G. J., McCavitt-Malvido, M., O'Leary, P. C., Jogalekar, M. P., Diolaiti, M. E., Kimmerly, G. R., Tsou, C. L., Gascon, R., Montano, M., Martinez-Sobrido, L., Krogan, N. J., Ashworth, A., Fraser, J. S., & Ott, M. (2023). A single inactivating amino acid change in the SARS-CoV-2 NSP3 Mac1 domain attenuates viral replication in vivo. PLoS pathogens, 19(8), e1011614. https://doi.org/10.1371/journal.ppat.1011614

Tao, S., Zandi, K., Bassit, L., Ong, Y. T., Verma, K., Liu, P., Downs-Bowen, J. A., McBrayer, T., LeCher, J. C., Kohler, J. J., Tedbury, P. R., Kim, B., Amblard, F., Sarafianos, S. G., & Schinazi, R. F. (2021). Comparison of anti-SARS-CoV-2 activity and intracellular metabolism of remdesivir and its parent nucleoside. Current research in pharmacology and drug discovery, 2, 100045. https://doi.org/10.1016/j.crphar.2021.100045

Tashiro, K., Wijngaarden, S., Mohapatra, J., Rack, J. G. M., Ahel, I., Filippov, D. V., & Liszczak, G. (2023). Chemoenzymatic and Synthetic Approaches To Investigate Aspartate- and Glutamate-ADP-Ribosylation. Journal of the American Chemical Society, 145(25), 14000–14009. https://doi.org/10.1021/jacs.3c03771

Tóth, B., Iordanov, I., & Csanády, L. (2014). Putative chanzyme activity of TRPM2 cation channel is unrelated to pore gating. Proceedings of the National Academy of Sciences of the United States of America, 111(47), 16949–16954. https://doi.org/10.1073/pnas.1412449111

Virdi, R. S., Bavisotto, R. V., Hopper, N. C., Vuksanovic, N., Melkonian, T. R., Silvaggi, N. R., & Frick, D. N. (2020). Discovery of Drug-Like Ligands for the Mac1 Domain of SARS-CoV-2 Nsp3. SLAS discovery : advancing life sciences R & D, 25(10), 1162–1170. https://doi.org/10.1177/2472555220960428

Vogel G. (2022). New subvariants are masters of immune evasion. Science (New York, N.Y.), 376(6594), 679–680. https://doi.org/10.1126/science.adc9448

Voorneveld, J., Rack, J. G. M., Ahel, I., Overkleeft, H. S., van der Marel, G. A., & Filippov, D. V. (2018). Synthetic α- and β-Ser-ADP-ribosylated Peptides Reveal α-Ser-ADPr as the Native Epimer. Organic letters, 20(13), 4140–4143. https://doi.org/10.1021/acs.orglett.8b01742

Voorneveld, J., Kloet, M. S., Wijngaarden, S., Kim, R. Q., Moutsiopoulou, A., Verdegaal, M., Misra, M., Đikić, I., van der Marel, G. A., Overkleeft, H. S., Filippov, D. V., & van der Heden van Noort, G. J. (2022). Arginine ADP-Ribosylation: Chemical Synthesis of Post-Translationally Modified Ubiquitin Proteins. Journal of the American Chemical Society, 144(45), 20582–20589. https://doi.org/10.1021/jacs.2c06249

Voth, L. S., O'Connor, J. J., Kerr, C. M., Doerger, E., Schwarting, N., Sperstad, P., Johnson, D. K., & Fehr, A. R. (2021). Unique Mutations in the Murine Hepatitis Virus Macrodomain Differentially Attenuate Virus Replication, Indicating Multiple Roles for the Macrodomain in Coronavirus Replication. Journal of virology, 95(15), e0076621. https://doi.org/10.1128/JVI.00766-21

Wang, Z., Yang, L., & Song, X. Q. (2022). Oral GS-441524 derivatives: Next-generation inhibitors of SARS-CoV-2 RNA-dependent RNA polymerase. Frontiers in immunology, 13, 1015355. https://doi.org/10.3389/fimmu.2022.1015355

Wazir, S., Maksimainen, M. M., Alanen, H. I., Galera-Prat, A., & Lehtiö, L. (2021). Activity-Based Screening Assay for Mono-ADP-Ribosylhydrolases. SLAS discovery : advancing life sciences R & D, 26(1), 67–76. https://doi.org/10.1177/2472555220928911

Weinschenk, L. (2015). DiPPro nucleotides with non-symmetric masking of the pyrophosphate unit. Dissertation. University of Hamburg

Westhof, E., Röder, O., Croneiss, I., & Lüdemann, H. D. (1975). Ribose conformations in the common purine(beta)ribosides, in some antibiotic nucleosides, and in some isopropylidene derivatives: a comparison. Zeitschrift fur Naturforschung. Section C, Biosciences, 30(2), 131–140. https://doi.org/10.1515/znc-1975-3-401

Yu, H. N., Song, E. K., Yoo, S. M., Lee, Y. R., Han, M. K., Yim, C. Y., Kwak, J. Y., & Kim, J. S. (2007). Activation of NUDT5, an ADP-ribose pyrophosphatase, by nitric oxide-mediated ADP-ribosylation. Biochemical and biophysical research communications, 354(3), 764–768. https://doi.org/10.1016/j.bbrc.2007.01.055

Zhang, J. H., Chung, T. D., & Oldenburg, K. R. (1999). A Simple Statistical Parameter for Use in Evaluation and Validation of High Throughput Screening Assays. Journal of biomolecular screening, 4(2), 67–73. https://doi.org/10.1177/108705719900400206

Zhang, Q., Bastard, P., Liu, Z., Le Pen, J., Moncada-Velez, M., Chen, J., Ogishi, M., Sabli, I. K. D., Hodeib, S., Korol, C., Rosain, J., Bilguvar, K., Ye, J., Bolze, A., Bigio, B., Yang, R., Arias, A. A., Zhou, Q., Zhang, Y., Onodi, F., … Casanova, J. L. (2020). Inborn errors of type I IFN immunity in patients with life-threatening COVID-19. Science (New York, N.Y.), 370(6515), eabd4570. https://doi.org/10.1126/science.abd4570

Zhao, Q., Capelli, R., Carloni, P., Lüscher, B., Li, J., & Rossetti, G. (2021). Enhanced Sampling Approach to the Induced-Fit Docking Problem in Protein-Ligand Binding: The Case of Mono-ADP-Ribosylation Hydrolase Inhibitors. Journal of chemical theory and computation, 17(12), 7899–7911. https://doi.org/10.1021/acs.jctc.1c00649

Zimmermann, L., Zhao, X., Makroczyova, J., Wachsmuth-Melm, M., Prasad, V., Hensel, Z., Bartenschlager, R., & Chlanda, P. (2023). SARS-CoV-2 nsp3 and nsp4 are minimal constituents of a pore spanning replication organelle. Nature communications, 14(1), 7894. https://doi.org/10.1038/s41467-023-43666-5

Danksagung

Ich möchte mich von ganzem Herzen bei meinem Doktorvater Dr. Ralf Fliegert bedanken. Seine unermüdliche Hilfsbereitschaft und exzellente Betreuung haben einen großen Anteil am Erfolg dieser Arbeit.
Großer Dank gebührt auch Prof. Ralph Holl für die Begutachtung dieser Arbeit. Prof. Chris Meier möchte ich für die Co-Betreuung danken sowie seiner Arbeitsgruppe, insbesondere Sahra Tajdar und Benedikt Ganter, die immer wieder den benötigten Nachschub an Testsubstanzen sicherstellen konnten.
Ferner danke ich auch Prof. Andreas H. Guse für die Zusage zur Anfertigung meiner Arbeit an seinem Institut und den vielen anregenden Diskussionen im Rahmen der allwöchentlichen Laborbesprechung und des SFB 1328 sowie für die Unterstützung bei der Teilnahme an Kongressen. In diesem Zusammenhang bedanke ich mich auch bei meiner Arbeitsgruppe - allen voran bei Marina Ocenas, deren Masterarbeit ich anleiten durfte sowie Andreas Bauche, der mich nicht nur tatkräftig bei der Durchführung und Planung der Versuche unterstützt hat, sondern auch für eine stets heitere Arbeitsatmosphäre sorgte. Dank gebührt auch Stefanie Etzold und Frederike Kulow für die Unterstützung im Laboralltag.
Bedanken möchte ich mich auch bei Prof. Barry VL Potter für die vielen ADPR Derivate und László Csanády für die Bereitstellung von AMPcPR. Mein Dank gilt auch Dr. Susanne Pfefferle, Prof. Andreas G. Ladurner und Prof. Bernhard Lüscher für die Unterstützung mit Materialien und Vektoren sowie die vielen (nicht nur fachlich) spannenden Gespräche.
Ferner möchte ich auch den Strukturbiologen am DESY danken, insbesondere Dr. Simon Sander, Prof. Henning Tidow, Dr. David Ruiz Carrillo, Dr. Stephan Niebling und Dr. Maria Garcia Alai für das Bereitstellen von Materialien und Instrumenten sowie für die tatkräftige Unterstützung bei der Durchführung und Interpretation von Experimenten.
Nicht zuletzt möchte ich mich auch bei meiner Familie und meinen Freunden bedanken, die mir immer stets geholfen haben, die vielen anstrengenden Phasen und Durststrecken meiner Promotion zu überstehen.
Danke euch Allen!

Eidesstattliche Versicherung

Hiermit versichere ich an Eides statt, die vorliegende Dissertationsschrift selbst verfasst und keine anderen als die angegebenen Quellen und Hilfsmittel benutzt zu haben. Sofern im Zuge der Erstellung der vorliegenden Dissertationsschrift generative Künstliche Intelligenz (gKI) basierte elektronische Hilfsmittel verwendet wurden, versichere ich, dass meine eigene Leistung im Vordergrund stand und dass eine vollständige Dokumentation aller verwendeten Hilfsmittel gemäß der Guten wissenschaftlichen Praxis vorliegt. Ich trage die Verantwortung für eventuell durch die gKI generierte fehlerhafte oder verzerrte Inhalte, fehlerhafte Referenzen, Verstöße gegen das Datenschutz- und Urheberrecht oder Plagiate.

Hamburg, 28.06.2024